

Composite Cathodes for Lithium Rechargeable Batteries

by

Elsa A. Olivetti

B.S. Engineering Science
University of Virginia, 2000

Submitted to the Department of Materials Science and Engineering in
Partial Fulfillment of the Requirements for the Degree of

Doctor of Philosophy in Materials Science and Engineering

at the

Massachusetts Institute of Technology

June 2007

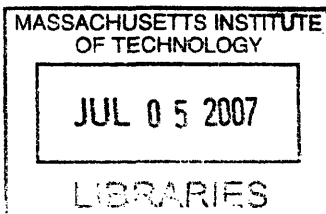
©2007 Massachusetts Institute of Technology
All Rights Reserved

Signature of Author: _____
Department of Materials Science and Engineering
May 7th, 2007

Certified by: _____
Donald R. Sadoway
John P. Elliott Professor of Materials Chemistry
Thesis Supervisor

Certified by: _____
Anne M. Mayes
Toyota Professor of Materials Science and Engineering
Thesis Supervisor

Accepted by: _____
Samuel M. Allen
POSCO Professor of Physical Metallurgy
Chair, Departmental Committee on Graduate Students



ARCHIVES

Composite Cathodes for Lithium Rechargeable Batteries

by

Elsa A. Olivetti

Submitted to the Department of Materials Science and Engineering
on May 7th, 2007 in partial fulfillment of the requirements for the
Degree of Doctor of Philosophy in Materials Science and Engineering

Abstract:

The utility of incorporating continuous, nanoscale vanadium oxide phases within preferred domains of self-organizing copolymers was investigated towards the fabrication of composite, nanoarchitected electrode materials for solid-state rechargeable batteries. *In situ* growth of cathodic phases within ion-conducting copolymer domains was explored as a means to control morphology and to increase the surface-area-to-volume ratio, thereby increasing the specific electrode area for faradaic reactions and decreasing ion diffusion distances within the electrode-active material.

Copolymers of microphase-separating rubbery block and graft copolymers, previously developed as solid electrolytes, provide a matrix for directing the synthesis of an inorganic battery-active phase. The copolymers include poly[(oxyethylene)₉ methacrylate]-*block*-poly(butyl methacrylate) (POEM-*b*-PBMA) with a domain periodicity of ~35 nm made by atom transfer radical polymerization, and poly[(oxyethylene)₉ methacrylate]-*graft*-poly(dimethyl siloxane) (POEM-*g*-PDMS) with a domain periodicity of ~17 nm made by free radical polymerization. The resulting microphase-separated polymer is a structure of alternating hydrophilic (Li-ion conducting) and hydrophobic regions.

Sol-gel chemistry involving a vanadium alkoxide precursor enabled the *in situ* growth of cathode-active vanadium oxide within the continuous ion-conducting POEM domains of the microphase-separated copolymers. Resulting films, termed POEM-*b*-PBMA/VO_x and POEM-*g*-PDMS/VO_x, were freestanding and mechanically flexible. Small angle x-ray scattering and transmission electron microscopy revealed the nanoscale morphology of the composite and confirmed the spatially-selective incorporation of up to 34 wt% VO_x in POEM-*b*-PBMA and 31 wt% in POEM-*g*-PDMS.

Electronically conductive components, necessary for wiring of the lithium-active vanadium oxide domains to the external circuit, were added through a variety of methods. Dispersions of acid-treated and cryo-ground carbon black within POEM-*b*-PBMA/VO_x enabled the cycling of this material as a cathode. Reversible capacities of ~40 mAh/g were measured for batteries fitted with a polymer electrolyte doped with LiCF₃SO₃ and a lithium foil anode. Electrolyte thickness studies indicated battery performance was limited by the ionic conductivity of the solid electrolyte. Using liquid electrolyte resulted in improved capacity (at higher currents) over conventional composite cathodes made from sol-gel derived vanadium oxide without the polymer matrix. The vanadium oxide nanoarchitecture was preserved upon removal of the polymer by heat treatment. The resulting *templated* vanadium oxide, when repotted with carbon black and binder, exhibited improved capacity at high current over *non-templated* vanadium oxide cathodes.

Thesis Supervisors: Donald R. Sadoway, John F. Elliott Professor of Materials Chemistry
Anne M. Mayes, Toyota Professor of Materials Science and Engineering

Table of Contents:

List of Figures	
List of Tables	
List of Abbreviations	
Acknowledgments	
Chapter 1 : Introduction	13
Battery Overview	13
Battery Metrics.....	16
Energy Density.....	16
Power Density.....	17
Cycle Life.....	17
Tradeoffs in Battery Architecture: Energy Density vs. Power Density.....	17
Polymers for Structure-Direction Overview.....	22
Description of Thesis	23
References.....	24
Chapter 2 : Literature Review.....	26
Templating and Structure-Directing with Polymers.....	26
Templating for Batteries	29
Vanadium Oxide and Vanadium Oxide Architectures	30
Electrochemistry of Vanadium Oxide	34
Electronic Conductivity	38
Conjugated Polymers.....	40
Summary and Introduction to the Next Section.....	44
References.....	45
Chapter 3 : Processing and Characterization Techniques.....	53
Polymer synthesis	53
Materials	53
Block copolymer synthesis	53
Graft copolymer synthesis	55
Active Battery material.....	56
Materials	56
Synthesis of Composite Films	56
Electronic Conductivity	57
Materials	57
Carbon Black	58
Conducting Polymers.....	59
Silver Salt.....	60
Carbon Nanotubes.....	61
Electrochemical Characterization	61
Materials	61
Methods.....	61
Techniques	62
Electrochemical Tests Performed	63
Characterization techniques: Ex Situ	66
Polymer Characterization.....	66
X-ray Diffraction	66

Spectroscopy	66
Thermal Characterization.....	67
Rheology	67
Electron Microscopy	68
Surface Area.....	68
References.....	70
Chapter 4 : Structure-Directed Vanadium Oxide	72
Polymer Matrix	72
Inorganic Characterization: POEM-b-PBMA/VO _x	77
Structure and Chemical Characterization	77
Characterization of phases	82
Electrochemical Characterization	84
Inorganic Characterization: POEM-g-PDMS/VO _x	86
Summary	91
References.....	93
Chapter 5 : Electronic Conductivity	95
Without additive.....	96
Silver Salt.....	97
PEDOT	100
Capacity of PEDOT	100
Carbon Black	113
Carbon black: Performance Limitations of the Battery	119
Carbon black: Advantages of system.....	120
Summary	122
References.....	124
Chapter 6 : Benefits of Templated Architecture.....	126
A Word about Taxonomy	127
Removing the Template.....	127
Template Removal: Changing the Atmosphere.....	131
Calculating Potential Benefits of Architecture	137
Mass Transport.....	139
Cycling Data for Templated VO _x	140
Discussion of Performance	142
Summary	145
References.....	147
Chapter 7 : Contributions of Dissertation	149
General Conclusions	149
Suggested Directions	151
Other applications	153
References.....	154

List of Figures:

Figure 1-1: A schematic of a rechargeable lithium battery upon discharge.	15
Figure 1-2: Schematic of the limiting kinetic processes within the electrodes.....	20
Figure 1-3: Schematic showing morphologies of diblock copolymers.	22
Figure 2-1: Block copolymer nanoreactor scheme for metal nanocluster synthesis	28
Figure 2-2: Morphologies obtained from PI- <i>b</i> -PEO with varying amounts of alkoxides	29
Figure 2-3: Formation of V ₂ O ₅ from sol gel process.....	33
Figure 2-4: Discharge curve for crystalline and xerogel V ₂ O ₅	35
Figure 2-5: Process for coating V ₂ O ₅ on PEG-carbon nanoparticles.	39
Figure 2-6: Chemical structure of poly(3,4-ethylene dioxythiophene)	42
Figure 2-7: Schematic diagram of assembly of PEDOT into V ₂ O ₅ layers.....	43
Figure 2-8: Charge-discharge cycles of Li _{1.03} Mn _{1.97} O ₄ /PEDOT composite electrodes ...	44
Figure 3-1: POEM- <i>b</i> -PBMA chemical structure	55
Figure 3-2: POEM- <i>g</i> -PDMS chemical structure.....	55
Figure 3-3: Scheme for growth of vanadium oxide <i>in situ</i> in the polymer domains	56
Figure 3-4: Scheme for adding carbon black to composite films	58
Figure 3-5: CVD reactor, Reproduced from Lock <i>et al.</i> [12]	60
Figure 3-6: Coin cell used in battery testing.....	61
Figure 3-7: Schematic of coin cell used in battery testing.....	62
Figure 3-8: Schematic of 3-electrode cell showing WE, RE and CE	63
Figure 3-9: Schematics of test cells	65
Figure 4-1: SAXS and TEM characterization of pristine POEM- <i>b</i> -PBMA.	73
Figure 4-2: DSC trace for POEM- <i>b</i> -PBMA.	74
Figure 4-3: SAXS and TEM characterization of pristine POEM- <i>g</i> -PDMS.....	74
Figure 4-4: DSC trace for POEM- <i>g</i> -PDMS.....	75
Figure 4-5: Ionic conductivities measured by EIS for POEM and POEM- <i>b</i> -PBMA	76
Figure 4-6: Ionic conductivities measured by EIS of POEM and POEM- <i>g</i> -PDMS.....	76
Figure 4-7: POEM- <i>b</i> -PBMA film incorporating 18 wt% VO _x	77
Figure 4-8: Weight% of VO _x from TGA as a function of precursor concentration	78
Figure 4-9: SAXS patterns for POEM- <i>b</i> -PBMA nanocomposite with vanadium oxide..	78
Figure 4-10: TEM micrographs of POEM- <i>b</i> -PBMA containing 24 and 50 wt% V ₂ O ₅ . .	79
Figure 4-11: STEM maps of POEM- <i>b</i> -PBMA containing 24 wt% vanadium oxide.	80
Figure 4-12: DSC trace of pristine polymer and after incorporation of vanadium oxide.	81
Figure 4-13: FTIR spectra for neat POEM- <i>b</i> -PBMA and POEM- <i>b</i> -PBMA/VO _x	82
Figure 4-14: XPS spectra of V 2p peak for neat vanadium oxide and composite film	83
Figure 4-15: WAXS for POEM- <i>b</i> -PBMA, amorphous VO _x and nanocomposite	84
Figure 4-16: CV for VO _x and POEM- <i>b</i> -PBMA/VO _x in LiClO ₄ /PC electrolyte.....	85
Figure 4-17: SAXS spectra for pristine POEM- <i>g</i> -PDMS and its nanocomposite films...	86
Figure 4-18: WAXS spectra for pristine POEM- <i>g</i> -PDMS and homopolymer.	87
Figure 4-19: WAXS spectra for pristine POEM- <i>g</i> -PDMS and nanocomposite films.	88
Figure 4-20: DSC curves for pristine POEM- <i>g</i> -PDMS and its nanocomposite films.	89
Figure 4-21: FT-IR spectra for pristine POEM- <i>g</i> -PDMS and its nanocomposite films..	90
Figure 4-22: Storage and loss moduli for pristine POEM- <i>g</i> -PDMS and nanocomposite .	90
Figure 5-1: Galvanostatic cycling of POEM- <i>b</i> -PBMA/VO _x film.....	96
Figure 5-2: WAXS for POEM- <i>b</i> -PBMA/VO _x /Ag heated, w/o heating and AgNO ₃	98

Figure 5-3: TEM of POEM- <i>b</i> -PBMA/VO _x film containing Ag particles.....	98
Figure 5-4: TEM of POEM- <i>g</i> -PDMS/VO _x film containing Ag.....	99
Figure 5-5: POEM- <i>b</i> -PBMA/VO _x /Ag cycling data at C/20.	100
Figure 5-6: PEDOT deposition on Au electrode.....	101
Figure 5-7: Cyclic voltammogram of PEDOT.....	101
Figure 5-8: Charge/Discharge from the POEM- <i>b</i> -PBMA/VO _x /PEDOT(CVD) film.	103
Figure 5-9: Capacity from POEM- <i>b</i> -PBMA/VO _x /PEDOT(CVD) as cathode	103
Figure 5-10: Cross-sectional STEM of CVD PEDOT on POEM- <i>b</i> -PBMA/VO _x	104
Figure 5-11: Higher magnification STEM micrograph with chemical map of sulfur. ...	105
Figure 5-12: CV PEDOT deposition on VO _x sputtered ITO and image of film.....	106
Figure 5-13: PEDOT deposition onto POEM- <i>b</i> -PBMA/VO _x coated Al wire mesh.....	107
Figure 5-14: PEDOT deposition onto POEM- <i>b</i> -PBMA/VO _x coated ITO glass slide....	108
Figure 5-15: POEM- <i>b</i> -PBMA/VO _x film containing PEDOT added as monomer.....	108
Figure 5-16: CV of electropolymerization of EDOT w/POEM- <i>b</i> -PBMA/VO _x	109
Figure 5-17: STEM mapping O, S and V w/in POEM- <i>b</i> -PBMA/VO _x /PEDOT.....	111
Figure 5-18: Cycling for 120 μm POEM- <i>b</i> -PBMA/VO _x /PEDOT film at 2.5 μA/mg....	112
Figure 5-19: Impedance plot of POEM- <i>b</i> -PBMA/VO _x /PEDOT.	113
Figure 5-20: POEM- <i>b</i> -PBMA with 34 wt% VO _x and 5 wt% CB.....	114
Figure 5-21: TEM of POEM- <i>b</i> -PBMA w/34 wt% VO _x and 5 wt% acid-treated CB.	115
Figure 5-22: Nyquist plot of POEM- <i>b</i> -PBMA/VO _x with and without carbon black.	116
Figure 5-23: Cycling for POEM- <i>b</i> -PBMA/VO _x /CB film with solid electrolyte.	117
Figure 5-24: Cycling for POEM- <i>b</i> -PBMA/VO _x /CB (acid-treated & non-acid-treated)	118
Figure 5-25: CV for POEM- <i>b</i> -PBMA films w/VO _x and/or CB (acid-treated).....	119
Figure 5-26: Discharge of POEM- <i>b</i> -PBMA/VO _x /CB w/ varying electrolyte thickness.	120
Figure 5-27: Cycling data of POEM- <i>b</i> -PBMA/VO _x /CB w/ current w/liquid elyte.	121
Figure 6-1: SEM of POEM- <i>b</i> -PBMA/VO _x after polymer removal under Ar at 400°C.	128
Figure 6-2: Non-templated VO _x synthesized and cast without polymer.	129
Figure 6-3: TEM of templated VO _x heated to 600°C under argon and crushed.....	129
Figure 6-4: Higher magnification TEM micrograph of templated VO _x particles.....	130
Figure 6-5: WAXS for sol-gel derived vanadium oxide heated at 400°C	131
Figure 6-6: Ellingham diagram for vanadium oxide and carbon dioxide.....	132
Figure 6-7: XPS V2p spectrum of sol-gel derived, non-templated vanadium oxide.....	133
Figure 6-8: TEM of sol-gel derived, non-templated VO _x ground for use in cathode....	133
Figure 6-9: XPS V2p of sol-gel derived, templated VO _x , heated 400°C under argon. ..	134
Figure 6-10: XPS V2p of sol-gel derived, templated VO _x , heated 400°C under air.	134
Figure 6-11: TEM of sol-gel derived, templated VO _x heated to 400°C in air.	135
Figure 6-12: XPS of VO _x heated first in argon at 400°C, then heating in air to 400°C.	136
Figure 6-13: TEM of templated VO _x heated at 400°C in argon, then heating in air.	136
Figure 6-14: V ₂ O ₅ composite cathode cycled at different rates with liquid electrolyte..	140
Figure 6-15: Discharge curves for templated and non-templated VO _x at C/5.....	141
Figure 6-16: 1 st discharge curves for templated vs. non-templated composite cathodes.	142
Figure 6-17: SEM of composite cathode made with non-templated VO _x	143
Figure 6-18: SEM of composite cathode made from non-templated VO _x at high mag..	144
Figure 6-19: SEM of composite cathode made with templated VO _x	144
Figure 6-20: SEM of cathode made from templated VO _x at higher magnification.	145

List of Tables:

Table 5-1: Table of capacity and depth calculation for POEM-*b*-PBMA/VO_x/PEDOT. 112
Table 5-2: Conductivity values for various electronic conductivity additives. 123
Table 6-1: Elemental analysis on films with polymer removed under different atmospheres..... 136
Table 6-2: Surface area: volume comparing templated and non-templated VO_x 138
Table 6-3: Capacity from templated and non-templated VO_x at C/5..... 141
Table 6-4: Summary of VO_x films, templated and non-templated. 146

List of Abbreviations:

AIBN = 2,2'-azobisisobutyronitrile initiator
BET = brunauer, Emmet and Teller
CB = Carbon black
CCC = conventional composite cathode
CV = cyclic voltammetry
DCM = dichloromethane
DI = deionized
FTIR = fourier transform infrared spectroscopy
GPC = gel permeation chromatography
HMTETA = 1,1,4,7,10,10-hexamethyltriethylenetetramine
IPA = isopropyl alcohol
ITO = indium tin oxide
NMP = 1-methyl-2-pyrrolidinone
NMR = nuclear magnetic resonance
PANI = polyaniline
PC = propylene carbonate
PEDOT = Poly (3,4-ethylene dioxythiophene)
PEO = polyethylene oxide
POEM-b-PBMA = poly[(oxyethylene)₉ methacrylate]-*block*-poly(butyl methacrylate)
POEM-g-PDMS = poly[(oxyethylene)₉ methacrylate]-*graft*-poly(dimethyl siloxane)
PPY = polypyrrole
PTFE = polytetrafluoroethylene
PVDF = polyvinylidene fluoride
SAXS = small angle x-ray scattering
SEM = scanning electron microscopy
STEM = scanning transmission electron microscopy
TEM = transmission electron microscopy
TGA = thermogravimetric analysis
THF = tetrahydrofuran
TMO = transition metal oxide
VO(OⁱPr)₃ = vanadyl triisopropoxide
VO_x = vanadium oxide
WAXS = wide angle x-ray scattering
XPS = x-ray photoelectron spectroscopy

Acknowledgments

First, I would like to thank my advisors, Professors Anne Mayes and Donald Sadoway for their patience and investment in my development as a scientist. Prof. Mayes' intellectual prowess, scientific curiosity, and attention to detail have taught me so much. She has touched the lives of many at MIT and the greater polymer community. Professor Sadoway has always entrusted me to learn from my mistakes, teaching me how to think independently. I have also appreciated his incredible teaching skills, precise use of language, and command of an audience. I am grateful to both of them for their encouragement, advice throughout the years, and tremendous support.

I would also like to thank my committee members, Prof. Robert Cohen and Prof. Yang Shao-Horn. Prof. Cohen met with me early on to shape this work and his students, Yot Boontongkong and Tom Wang, helped with my attempts at electroless deposition. Prof. Shao-Horn's post-doctoral researchers, Sundeep Kumar and more recently Naoaki Yabuuchi, have provided helpful input.

Several other researchers have helped with this work and I would like to thank them for their assistance. During his tenure at MIT, Dr. Jong Hak Kim was instrumental in the progress of my research and helped with polymer synthesis, FTIR and mechanical property testing. Ayse Asetakin performed all of the XPS in this thesis and her cheerful disposition always made each day a little brighter. Dr. Ikuo Tanaguichi helped with the polymer synthesis, and I appreciated our conversations throughout my graduate experience. He has taught us all so much and I am very grateful for his time with the Mayes group. Ken Avery helped with some of the SEM and provided much needed conversations on batteries as well as all things pertaining to life. Sung Gap Im in Prof. Karen Gleason's group did the PEDOT CVD and helped me a great deal with the world of electronically conducting polymers. Dr. Aislinn Sirk joined the Sadoway group at a critical time for me and I have thoroughly enjoyed her lessons in three-electrode electrochemistry, her dedication to research, the spirit and community that she brought to the group, and for her companionship, not to mention editing this document many times over.

One of the best parts of my experience in graduate school has been the opportunity to develop skills in electron microscopy, which would not have been possible without the impeccable instruction of Mike Frongillo and Dr. Tony Garrett-Reed. Tony also helped with the STEM work and provided much guidance about the use of EDX in sample analysis. Thank you also to David Bell who taught me all about "modern microscopes" and the recent help from Yong Zhang with the FEG TEM. I learned microscopy sample preparatory skills from (and with) Patrick Boisvert, Jongseung Yoon and Juan Gonzalez who helped align moons when it was time to microtome.

I would also like to extend my gratitude to Patrick Trapa and Simon Mui who have helped with the science all along the way, even from afar, and for their great horn/piano music at my wedding. Thank you also to Will Kuhlman for his help with spin-coating, NMR and great science conversation over the green glow of the TEM phosphor screen. Nava Ariel has been a great friend throughout and I am grateful for her help in

teaching me the secrets to good microscopy. Thank you to Dilan Seneviratne for his help with the heat treatment portion of my thesis and for the use of Old Faithful. I would also like to thank my undergraduate mentors: Professors Robert Kelly and David Kaplan. In addition, thank you to Jodie Lutkenhaus, Rachel Pytel, Shirley Meng, Vahik Krikorian, Elisa Alonso and Lenny Rigione. I am also very grateful for the support of past and present labmates, Solar Olugebefola, Ozge Akbulut, Nathan Lovell, Ariya Akthakul, Heather Stern, David Bradwell, Andrew Gmitter, Chanaka de Alwis, Dihua Wang, Bing Li and the great help of lab UROPs, Harold Hsiung, Boris Rasin and Alex Konings. I am also very grateful for all the support and help from Jenna Picceri and Hilary Sheldon.

Thank you also to the sponsors of this work: the Office of Naval Research under Contract numbers N00014-02-1-0226 and N00014-05-1-0056 and in part by the MIT MRSEC Program of the National Science Foundation under Award number DMR-0213282.

The support and patience of my friends and family has been tremendous, truly overwhelming and something I will never be able to repay. My parents have been endlessly supportive and encouraging of my work and I owe a special thank you to my dad for providing inspiration for the first paragraph of this thesis. My fabulous sister has been crucial to keeping it all in perspective by providing the soundtrack to my graduate experience and many visits when she was in the neighborhood. And to Justin, thank you so much for being my teammate and companion through all of this, and thank you to your family for their never ending support.

I would like to dedicate this thesis to Justin and his mom, my heroes.

Chapter 1 : Introduction

A recent *New York Times* article described General Motors' introduction of its new hybrid vehicle, the Volt, at the North American International Auto Show. This vehicle is projected to travel up to 40 miles on batteries alone (longer than the daily distance traveled by almost 80% of U.S. commuters) [1] and would charge its long cylindrical battery pack through an onboard generator or a household plug-in. As described by GM, the Volt has one major challenge, "the battery technology to make it roadworthy does not yet exist," meaning a battery that meets these requirements has not yet been developed.[2]

The challenge for battery scientists with regard to electric vehicles is to develop small, light batteries that can achieve a real-world target for driving distance, such as the 40 miles mentioned above, before recharging. The U.S. Advanced Battery Consortium has set criteria for EV applications, which include a lifetime of 10 years, a cycle life of 1000 cycles along with a recharge time of between 3 and 6 hours at $< \$100/\text{kWh}$.¹ As the United States seeks solutions to alleviate its dependence on fossil fuels, which contribute to greenhouse gas emissions and make the country dependent on foreign energy sources, there is great demand for improved energy storage devices.

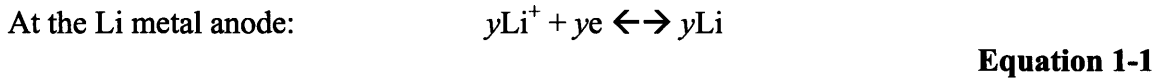
This thesis studies possible modifications in current battery architectures, more specifically in cathode materials, to improve overall performance specifically and investigates the relevant materials science because, as MIT Professor Donald Sadoway has observed, "the road to autonomy is paved with advanced materials." [3]

Battery Overview

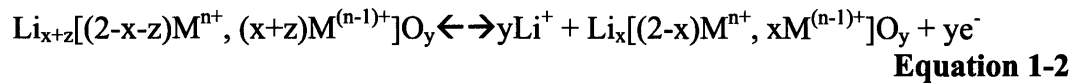
A rechargeable lithium battery operates due to a gradient in the chemical potential of lithium between the anode and cathode. A schematic of a typical rechargeable battery is shown in Figure 1-1. Upon discharge, lithium ions move from the anode to the cathode. If pure lithium metal is used as the anode, a charge transfer step will take place, $\text{Li} \rightarrow \text{Li}^+ + \text{e}^-$, and the soluble lithium ions will diffuse through the ionically conducting, electronically insulating electrolyte. When the ions reach the cathode particles and insert,

¹ http://www.uscar.org/guest/article_view.php?articles_id=85

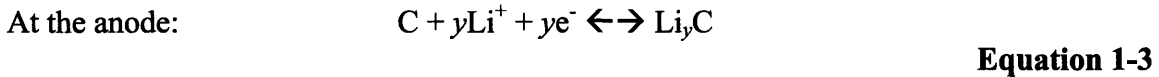
their presence causes a valence shift in the transition metal oxide cathode material. This, in turn, calls for a compensating electron from the external circuit (supplied from the reaction at the anode). The electrode reactions for charge and discharge of the intercalation compound cathode and pure lithium metal anode are shown in Equation 1-1 and Equation 1-2.



At the cathode:



where LiMO_y is a lithiated transition metal oxide. Or for Li-ion cells, where insertion occurs at both electrodes, using lithiated carbon on the anode side gives Equation 1-3.



where the system moves towards the right on charge and towards the left on discharge. On **discharge oxidation** occurs at the anode, while on **charging reduction** occurs at the “anode.”

As depicted in Figure 1-1, the conventional cathode contains several elements, including the battery active material (transition metal oxide), a conductivity additive (carbon black particles), and a polymer binder that combines the elements of this composite cathode.

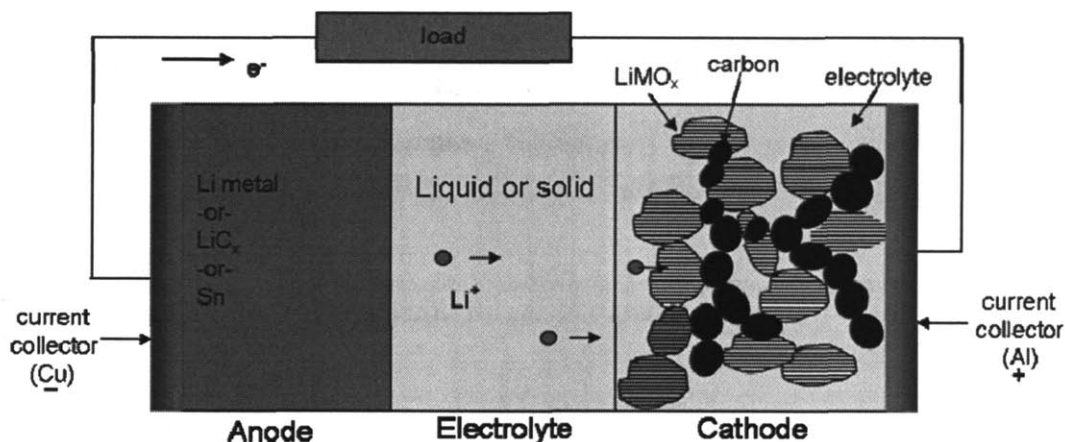


Figure 1-1: A schematic of a rechargeable lithium battery upon discharge.

The electrolyte of a rechargeable lithium battery must be ionically conducting but electronically insulating to allow Li^+ to pass but to prevent self discharge of the cell. The electrolyte may consist of a liquid organic solvent containing a high concentration of dissolved lithium salts. However, there are safety concerns and degradation issues associated with liquid electrolytes. To address these issues, liquid-like characteristics may be introduced to a solid electrolyte in the form of plasticizers, or an entirely solid electrolyte may be used.

Typical solid electrolytes are made of polyethylene oxide (PEO), which is able to dissolve lithium salt and become an ion conductor. The high molecular weight that makes this polymer solid also increases the polymer's crystallinity and, as a result, lowers the ionic mobility and therefore the conductivity. Additives to suppress crystallinity, such as clays or other inorganic components, have been incorporated into the polymer with some success.[4, 5] In our laboratory a family of polymer electrolytes consisting of a hydrophilic, ion-conducting block component (PEO-based) covalently bound to a hydrophobic, mechanically stabilizing block, have been developed. The PEO-based block is amorphous due to its comb-like architecture incorporating short PEO side chains, while the hydrophobic component confers solid-like characteristics upon microphase separation, increasing mechanical stability.[6, 7]

The choice of material and architecture for each element of a battery (anode, cathode and electrolyte as well as current collectors and packaging) will affect the overall system performance. The chemical potential gradient between the anode and the cathode

determines the voltage of the cell, while the amount of charge (Li^+) stored by the cell determines the capacity. To compare batteries of different chemistries, capacity is often normalized by either the weight or volume of the cell. Another important consideration for materials choice is the rate capability, which is the rate transfer of energy, i.e., current, determined by the kinetics of various rate phenomena. Other important parameters include safety and cycle life. Recent explosions of lithium ion cells in laptops due to several potential factors, including thermal runaway (addressed by altering the cathode chemistry) and the volatility and flammability of the electrolyte have brought about renewed interest in safety.[8] Sony, the company responsible for the manufacture of these batteries, has reported that the cost of recalling 9.9 million laptop computer batteries was \$429 million.[9] There are tradeoffs between electrolytes, however, as a solid electrolyte is advantageous from a safety perspective, but the ionic conductivity and therefore rate capability can be reduced.

The next section will describe relevant battery metrics and discuss the relationship between the metrics addressed in this work.

Battery Metrics

Depending on which chemistries and architectures are chosen for a battery, different applications and technologies can be targeted. This work focuses on rechargeable batteries that can be cycled readily through monotonic charge and discharge cycles. The key performance indicators for rechargeable batteries are high discharge current, large capacity, quick rechargeability, long shelf life (stable voltage) and long cycle life. Three related metrics that capture several of these characteristics are energy density, power density and cycle life. The following sections explain these metrics in detail.

Energy Density

Energy density refers to the amount of electrical energy available from the battery in a single discharge cycle, expressed in energy/mass (Wh/kg) or energy/volume (Wh/L) of battery material (which can be defined for either the electrode material or the entire battery). The theoretical energy density (Wh/kg) of a battery is determined by the product

of the battery voltage (V) times the charge capacity (Ah/kg) of the system². The actual energy density of a battery is always less than the theoretical value due to the inactive materials such as the electrolyte, conductivity additives, current collectors and packaging. Also, there are the inevitable energy loss mechanisms that become more significant at higher discharge rates (higher power), most notably the ohmic drop, which is the product of the current through the device and its internal resistance.

Power Density

The rate at which energy is delivered to or from the battery defines its power (expressed in W or kW). The maximum power a battery can deliver or accept is determined by the highest rate at which the battery can be discharged/charged and is governed by kinetic processes within the battery. The specific power (W/kg) is given by the battery voltage (V) times the battery discharge rate (A/kg). The discharge rate can also be expressed in terms of a C-rate. 1C is the current rate that would fully discharge the capacity of the cell in 1 hour, a 2C rate indicates full discharge/charge in 30 minutes, and a C-rate of ½ indicates full discharge/charge in 2 hours.

Cycle Life

Cycle life is defined as the number of charge/discharge cycles a battery can tolerate before it becomes unusable in a specific application. The cycle life is highly dependent on the depth of discharge of each cycle, with the cycle life decreasing drastically with higher depths of discharge when discharge cycles extend into irreversible regimes due to irreversible phase transformations.

Tradeoffs in Battery Architecture: Energy Density vs. Power Density

Battery chemistry and morphology will determine the limits of energy density and power density in a cell. The energy density is determined by the thermodynamics of the system (the potential difference between the anode and the cathode). The power density is determined by the kinetic processes such as electron transfer (reaction rate), mass transport within the cathode (diffusion length scales), and ion transport within the

² the product of the number of lithium ions, n , inserted per molecular mass, M , of the cathode times the Faraday constant, F ($n/M \times F$)

electrolyte. These processes result in more significant energy losses when the battery is operated at the higher end of its power capabilities (high C rate). Thus, for high power operation, a battery must have high Li^+ diffusion rates within the active material in the anode and the cathode, high electronic conductivity within the anode and cathode, high diffusion rates of ions through the electrolyte, and fast reaction rates at the cathode and anode surfaces. If any of these are sluggish, the properties of the battery as a whole are affected.

There are several mechanisms by which the power or energy density of the cell can be adversely affected. These voltage losses, detailed below in Equation 1-4, are described in the subsequent paragraphs.[10]

$$\Delta E = E_{\text{cath}} - E_{\text{anodic}} - IR - \eta_{\text{cath}} - \eta_{\text{anode}} - \eta_{\text{mass trans}} \quad \text{Equation 1-4}$$

Losses may be associated with electronic resistance in the electrodes. These IR losses are mitigated by developing electrode materials with higher intrinsic conductivities or by using composite electrodes consisting of active electrode materials mixed with higher conductivity inactive materials.

Kinetic losses associated with driving the faradaic processes at the electrode/electrolyte interfaces are termed charge transfer or overpotential losses, η_{cath} and η_{anode} . [11] These losses are minimized by using electrode/electrolyte pairs that have intrinsically high catalytic activities for the reactions involved and by maximizing the electrode/electrolyte interfacial area. The maximization of electrode/electrolyte interface can be achieved by making porous electrodes consisting of very small active particles (nanoparticles) or by increasing the total surface area.

The active materials' structure and particle size largely determine the diffusion rates of lithium ions within the anode and cathode. Losses associated with these diffusion processes are typically termed mass transport limitations, $\eta_{\text{mass trans}}$. [11] The development and use of materials with high intrinsic diffusivities helps mitigate this loss mechanism. The use of smaller particles (i.e. nanomaterials) shortens the distance ions need to diffuse.

The intercalation ability of Li into the cathode is limited by its diffusion in the solid, which hinders performance at higher rates of discharge. Therefore, increasing the

thickness of the electrode to increase its energy density will increase the diffusion penetration time as L^2/D (where D is the diffusion coefficient and L is the electrode thickness). Porous electrode structures will overcome diffusion limitations even in thicker films if there is electrolyte penetration. To illustrate the dependence of diffusion time on particle size, consider particles of diameter 50 and 5 μm along with a film that is 500 nm thick. Assuming a diffusion coefficient of $10^{-13} \text{ cm}^2/\text{s}$, the diffusion time through the inorganic would be 70,000, 700 and 7 hours, respectively.[12]

The schematic in Figure 1-2 illustrates the various forms of transport within the cathode/electrolyte interface that are enhanced by increasing the surface-area-to-volume ratio. Both slow transfer kinetics and slow lithium diffusion can be aided by increasing this ratio. Figure 1-2a illustrates the case of a graphite carbon anode upon charging. The processes of interest include the mass transport of Li^+ through the electrolyte (1), the charge transfer across the electrode/electrolyte interface (2), and metallic lithium transport (4) through the anode. Electronic conduction (6) through the anode is also necessary for charge to pass through the external circuit. So that the ingress of lithium was illustrated in both electrodes, Figure 1-2b shows the cathode upon discharging. Additional kinetic processes occurring in this intercalation cathode that may be improved by increasing the surface-area-to-volume ratio include: mass transport of Li^+ through the galleries of the cathode (4), compensating valence shift in the transition metal oxide (5) and electronic wiring of the cathode, enabling current to travel through the external circuit (3). The cathode must be a mixed conductor of ions and electrons to facilitate electron motion in the presence of Li^+ motion. In vanadium oxide, the cathode material studied in the thesis, conduction occurs by polaron hopping associated with V^{4+} and V^{5+} valence shifts. A “front” of charge transfer moves through the TMO cathode as Li^+ intercalates and destabilizes the V^{5+} .

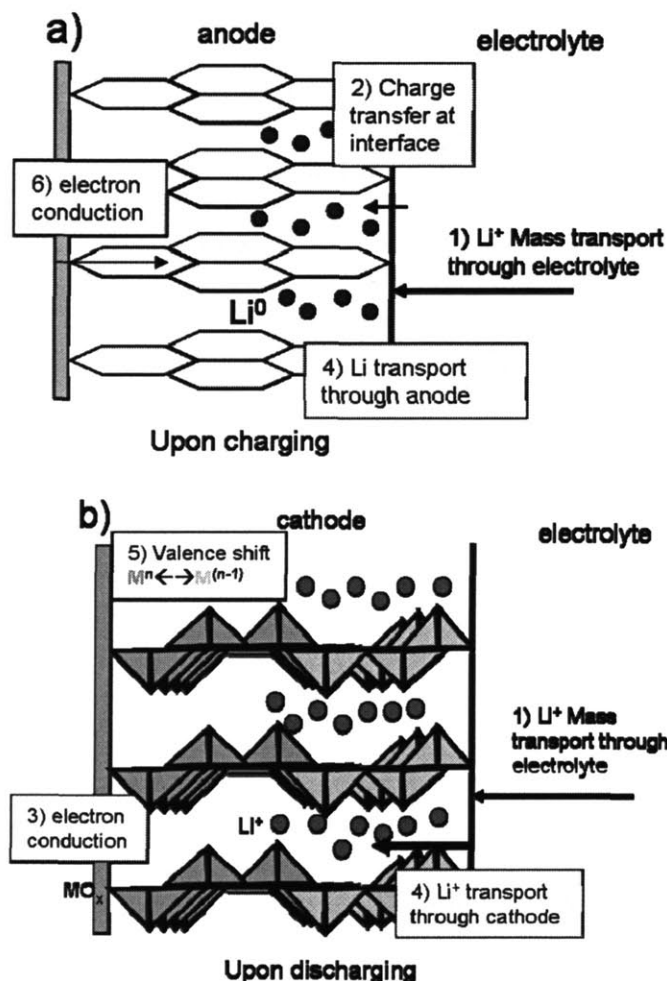


Figure 1-2: Schematic of the limiting kinetic processes within and at the electrode/electrolyte interface of a) LiC₆ carbon anode (upon charging) b) intercalation cathode (upon discharging).

Overall, in designing an optimal electrode material one seeks to use a large fraction of the electrode in the reversible redox reaction, to maintain electrical conductivity within the cathode, and present a high particle/electrolyte surface area over many discharge/charge cycles. The solid-state Li-ion diffusion coefficient (intrinsic to the material) and diffusion lengths may limit the kinetics (mass transfer effects) of these devices. Therefore, the rate capability or power performance of a battery is greatly influenced by the size of the particles making up the electrodes and by the electrode surface area. Improved power density exists in high surface area structures because the distance over which Li⁺ must diffuse in the solid-state is shorter. Critical interface area becomes more important as ionic conductivity decreases. A host material that provides a

larger free volume for Li^+ motion in the interstitial space would allow realization of higher Li^+ conductivity and hence higher power densities. In addition, at high discharge rates, high Li^+ insertion flux density and slow Li^+ transport result in concentration polarization of lithium within the electrode material. This phenomenon causes a drop in cell voltage, which results in termination of the discharge before accessing the full capacity of the electrode material. Improved rate capabilities delay the onset of concentration polarization.

However, a tradeoff exists between those battery systems with high energy density and those with high power density.[13, 14] The former requires electrodes with high capacity, high voltage, and a low mass of inactive materials (such as conductivity and polymeric binder additives). Systems with thin current collectors and thick, low porosity electrodes fit this profile. On the other hand, systems aiming for high power density use electrodes with low resistance but high voltage focus on thin, highly porous electrodes to reduce diffusion distances and high surface area. Often an increase in power density comes at the expense of energy density.

Other issues affecting the cycle life of a battery include particles becoming isolated from electronic additives, or other cathode particles, upon cycling because of volume excursions in the active battery phase.[14] Battery lifetime is determined by mechanical and chemical degradation that occurs during battery cycling. During charge and discharge, battery electrodes experience phase transformations between crystal structures of different volumes; for example, the layered phase reversing to the spinel with cycling in LiMn_2O_4 . [15] Thus, during cycling, significant volume changes occur, introducing mechanical stresses into the device that ultimately break down battery structural integrity. Furthermore, irreversible parasitic chemical reactions between the electrolyte and the electrodes or dendrite formation can change the electrode/electrolyte interface, thus limiting battery cycle life.[15]

This thesis will focus on the cathode, which is generally the limiting factor in improving rate capability.[16] To develop an alternative cathode material, block and graft copolymers, developed by our lab group as electrolytes for rechargeable batteries,

are used to structure-direct the growth of an active phase within the nanoscale domains of the polymer. The next section will briefly describe the properties of these polymers.

Polymers for Structure-Direction Overview

Block copolymers consist of two or more chemically distinct polymer block components that are covalently linked. When many copolymer chains are mixed, mutual repulsion between chemically dissimilar blocks causes them to segregate to form like domains. Chemical bonds between the two blocks limit their separation to the nanoscale, and the resulting morphologies seek to lower their interfacial energy. Therefore, different self-assembling morphologies can be achieved by changing the relative amounts of the two polymer components. The equilibrium polymer morphologies can range from body-center cubic packed spheres of one block in a matrix of the other to bicontinuous networks of each, as shown in Figure 1-3.






Nature of Patterns	Spheres	Cylinders	Double Diamond	Double Gyroid	Lamellae
Space group	$Im\bar{3}m$	$p6mm$	$ Ia\bar{3}d$	$Pn\bar{3}m$	pm
Blue domains: A block					
Vol frac. of A block	0-21%	21-33%	33-37%		37-50%

Figure 1-3: Schematic showing different morphologies of non-crystalline linear diblock copolymers. Reproduced from Park *et al.* [17]

This microphase-separating characteristic of copolymers has been used to structure direct the growth of inorganic phases within one block domain, relying on strategies such as differences in solubility or chemical tethering.[17-19] The current work employs microphase-separating block and graft copolymer electrolytes, previously developed in this group as electrolyte materials, and repurposes them as a matrix for the *in situ* growth of nanoscale vanadium oxide morphologies which serve as a battery active phase within the ion-conducting domains of the polymer. Increasing the surface-area-to-volume ratio within the cathode is expected to improve battery performance when it is limited by mass transfer. The enhanced performance is due both to reduced Li^+ diffusion

distances and to increased surface area over which faradaic reactions can occur. In addition, using a solid electrolyte with a cathode of similar composition may improve the kinetics at the electrode/electrolyte interface. The solid electrolyte also addresses safety issues present with a flammable organic liquid electrolyte and facilitates the formation of a fully solid-state device that can be made mechanically flexible.

This thesis investigates the use of microphase-separating copolymer electrolytes to generate cathode architectures.

Some of the questions this dissertation will address are:

1. Can microphase-separated polymers be used to direct the growth of cathode active materials, such as transition metal oxides?
2. Are the resulting microstructures continuous and on an appropriate size scale?
3. Can these structure-directed materials be used as cathodes? What electronic conductivity additives are necessary to make them usable?
4. Do these nanocomposites offer an improvement to a particular set of battery metrics, e.g. rate capability?

Description of Thesis

The next chapter provides a review of relevant literature, describing current approaches to cathode architecture, block copolymer templating and vanadium oxide's use as a cathode material. Chapter 3 describes the experimental techniques and synthesis strategies that make up the body of this work. Chapters 4-6 elaborate on the cathode films that were synthesized, their chemical and electrochemical characterization and their use in battery test cells. Chapter 4 focuses on the incorporation of vanadium oxide through sol-gel chemistries into the block copolymer, POEM-*b*-PBMA, and the graft copolymer POEM-*g*-PDMS to form a nanocomposite film. Electronic conductivity is necessary for the nanocomposite to function as a cathode, so Chapter 5 describes approaches to incorporating electronically components such as poly (3,4-ethylene dioxythiophene) and carbon black. In Chapter 6, the nano-architecture is explored in a composite cathode without the polymer to evaluate battery metrics. Finally, Chapter 7 summarizes the accomplishments of this thesis and provides recommendations for future research.

References

1. "NHTS 2001 Highlights Report, BTS03-05" by *US Department of Transportation*, 2.
2. Brooke, L., "All the Technology Needed for 100 mpg (Batteries Not Included)" in *New York Times*, January 7, 2006, 2, 12.
3. Sadoway, D. R. (2005).
4. Walls, H. J., Singhal, R. R., Spontak, R. J., Fedkiw, P. S. & Khan, S. A. "Nanocomposite Electrolytes with Fumed Silica and Hectorite Clay Networks: Passive versus Active Fillers." *Advanced Functional Materials*, **2003**, 13, 710-717.
5. Kurian, M., Galvin, M., Trapa, P. E., Sadoway, D. R. & Mayes, A. M. "Single-ion conducting polymer-silicate nanocomposite electrolytes for lithium battery applications." *Electrochimica Acta*, **2005**, 50, 2125-2134.
6. Trapa, P. E., Huang, B., Won, Y.-Y., Sadoway, D. R. & Mayes, A. M. "Block Copolymer Electrolytes Synthesized by Atom Transfer Radical Polymerization for Solid-State, Thin-Film Batteries." *Electrochemical and Solid-State Letters*, **2002**, 5, A85-A88.
7. Trapa, P. E. et al. "Rubbery Graft Copolymer Electrolytes for Solid-State, Thin-film Lithium Batteries." *Journal of the Electrochemical Society*, **2005**, 152, A1-A5.
8. AP posting, "Sony Says Recall Strains Battery Production" in *New York Times*, 5, C.
9. Darlin, D., "Reluctance and Silence on Recalls" in *New York Times*, October 28, 2006, 1, C.
10. Stender, W. W., Zivotinsky, P. B. & Stroganoff, M. M. "The voltage balance of a cell for the electrolysis of sodium chloride solutions. Distribution of voltage drop through the (Vorce) cells with vertical filtering diaphragms." *Transactions of the Electrochemical Society*, **1934**, 65, 24.
11. Bard, A. J. & Faulkner, L. R. *Electrochemical Methods* John Wiley & Sons: New York, 2001.

12. Tipton, A. L., S., P., Owens, B. B. & Smyrl, W. H. "Performance of Lithium/V₂O₅ Xerogel Coin Cells." *Journal of the Electrochemical Society*, **1996**, 143, A221-A223.
13. Doyle, M. & Newman, J. "Analysis of Capacity-rate Data for Lithium Batteries using Simplified Models of the Discharge Process." *Journal of Applied Electrochemistry*, **1997**, 27, 846-856.
14. Linden, D. *Handbook of Batteries* McGraw-Hill: New York, 2001.
15. Tarascon, J. M. & Armand, M. "Issues and Challenges Facing Rechargeable Lithium Batteries." *Nature*, **2001**, 414, 359-367.
16. Sadoway, D. R. & Mayes, A. M. "Portable Power: Advanced rechargeable lithium batteries." *MRS Bulletin*, **2002**, 27, 590-592.
17. Park, C., Yoon, J. & Thomas, E. L. "Enabling Nanotechnology with Self Assembled Block Copolymer Patterns." *Polymer*, **2003**, 44, 6725-6760.
18. Cohen, R. E. "Block Copolymers as Templates for Functional Materials." *Current Opinion in Solid State and Materials Science*, **1999**, 4, 587-590.
19. Templin, M. et al. "Organically Modified Aluminosilicate Mesostructures from Block Copolymer Phases." *Science*, **1997**, 278, 1795-1798.

Chapter 2 : Literature Review

This chapter summarizes relevant literature covering the methods and materials used in this dissertation. It begins with a discussion of block copolymers as templates to direct the growth of inorganic compounds. Next, it describes the transition metal oxide, vanadium oxide, and its use in lithium battery cathodes, as well as modifications to oxide cathode architecture. Finally, it presents relevant approaches to increase electronic conductivity within the cathode.

Templating and Structure-Directing with Polymers

When block copolymers are combined with inorganic compounds the composites that result include the properties of the organic host and the inorganic phase, thereby generating a variety of novel materials for magnetic, electronic or photonic applications. The interest in developing hybrid organic-inorganic, self-assembling materials stems from the small scale of microdomains and the tunability of size, shape and periodicity of these composites, which should lead to improved transport, mechanical, electrical and optical properties. Resulting materials are predicted to have larger surface-area-to-volume ratios and possibly desired quantum size effects. Current applications include contact lenses, scratch-resistant coatings, chemical filters and dental fillings.[1] Future applications, such as interconnects, sensors or lithography, could take advantage of other tunable properties including high anisotropy and high local dielectric contrast. Further tunability arises from the ability to control microstructure through application of applied fields.[2] Applications in nanotechnology have included micelles for drug delivery, formation of metal or ceramic nanodots and wires, as well as photonic crystals and masks for high density information storage.[1] The challenge and limit of these structures for many applications comes in the ability to control for defects and domain orientation on a large scale.

There are numerous examples of block copolymer templating found in the literature. This section will describe some that are most applicable to this research. Much of the seminal work describing structure-direction of inorganic compounds with organic species was done by Stucky and coworkers at the University of California, Santa Barbara.

In their most cited paper, Yang *et al.* described the use of surfactants and poly(alkylene oxide) block copolymers to form mesostructured systems for a variety of metal oxides and mixed oxides including TiO₂, Al₂O₃, WO₃, SnO₂, and others.[3] They have also used these structure-directing agents to form highly ordered mesoporous silica structures in acidic media, some with surface areas as high as 1000 m²/g.[4] A recent investigation by this group described the versatility and ease of combining polymers and metal alkoxides to form complicated and novel multicomponent mesostructured oxides (MMOs) including oxides of aluminum, silicon, titanium, tantalum and zirconium.[5] That paper presented a broadly applicable sol-gel approach for synthesizing MMOs, pointing out the potentially dissimilar condensation kinetics and chemistry of metal oxide precursors.

Work by Lopes and Jaeger exploited self-assembling diblock copolymers of poly(styrene-*block*-methyl methacrylate), PS-*b*-PMMA, as a scaffold for the diffusion of thermally-evaporated metal by relying on preferential wetting of metal components by one domain of the polymer (selective adsorption).[6] Because of the preference of metal-metal bonds to metal-polymer bonds, the aggregation of metal regions dominates the final structure. They found that nonequilibrium structures, achieved by short time annealing of small amounts of thermally evaporated metal, helped avoid this metal aggregation and resulted in highly ordered configurations.

Supercritical CO₂ (scCO₂) has been used to load polymer films with metal salts through preferential swelling of one domain over the other as shown by Watkins *et al.*[7-9] Once the inorganics were selectively deposited within the swollen framework, reduction of the metal salts was carried out by chemical or thermal means.[10] This approach is attractive because of the low toxicity, easy separation, variable density, low viscosity, low surface tension, and polymer plasticization.[11, 12] The swollen polymer demonstrated increased mass transport in the uptake of metals. The degree of swelling in the polymer and the diffusion rates could be controlled by density-mediated adjustments of solvent strength and changes in pressure and temperature. Several metal-polymer nanocomposites were produced, including those containing silver or platinum. In addition, Watkins demonstrated the growth of sulfides such as PbS in poly(styrene-*block*-acrylic acid) (PS-*b*-PAA) using scCO₂ processing with H₂S reduction and prepared sulfide

nanoclusters of Cu, Cd, Co, Ni, Zn and Ag by reducing metal salts in the P2VP domains of poly(styrene-*block*-2-vinyl pyridine) (PS-*b*-P2VP).

Work by Cohen and coworkers used block copolymers as *nanoreactors*. One approach involved block copolymers containing metal-sequestering moieties in one block such as carboxylic acids. These assembled to form nanoreactors due to microphase separation, as shown in Figure 2-1. Another approach involved incorporating organometallic monomers as one of the domains. In either case, a post-processing step provided the final inorganic phase through reduction or other decomposition methods.[13, 14]

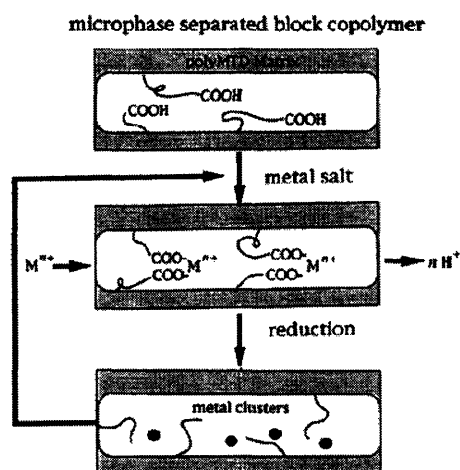


Figure 2-1: Block copolymer nanoreactor scheme for metal nanocluster synthesis. Reproduced from Cieben *et al.*[13]

Electroless deposition has been developed for continuous material loading of metals such as cobalt, nickel or copper within the hydrophilic block of a copolymer containing preloaded catalyst particles such as palladium.[15, 16] The extent of deposition was controlled through changes in the deposition rate and time. Cohen's group has more recently achieved patterned particles of iron, iron-cobalt, and cobalt nickel within the vinyl pyridine domain of PS-*b*-P2VP through preloading followed by thermal decomposition of organometallic complexes.[17]

Wiesner and coworkers at Cornell employed sol-gel chemistry to grow aluminosilicates from two metal alkoxide precursors, (3-glycidyloxypropyl-) trimethoxysilane and aluminum sec-butoxide, within the PEO domains of polyisoprene-

block-polyethylene oxide, PI-*b*-PEO.[18] The PEO domains confined the condensation products of the pre-hydrolyzed metal alkoxide. By increasing the amount of precursor incorporated within a dissolved polymer of fixed concentration, several polymer morphologies were accessed, as shown in Figure 2-2. This group highlighted the amphiphilic nature of the block copolymer and the low glass transition temperature of the hydrophobic block as properties enabling the final structures.[19] Solid-state NMR indicated that the local structure of the inorganic condensation products was not disturbed by the polymer and that the PEO phase was integrated with the ceramic phase.[20]

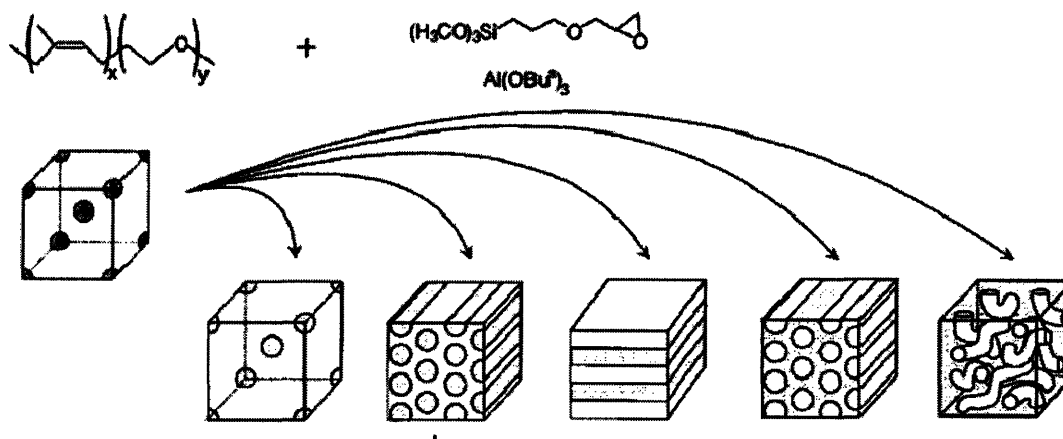


Figure 2-2: Morphologies obtained from PI-*b*-PEO with differing amounts of metal alkoxides. Reproduced from Ulrich *et al.*[19]

This approach has also been used to incorporate magnetite $\gamma\text{-Fe}_2\text{O}_3$ particles in the walls of the aluminosilicate structure to establish supermagnetic nanostructures of spherical, lamellar, and hexagonal block copolymer morphologies.[21, 22] In addition, the Cornell group developed a polymer electrolyte using the organic-inorganic solid hybrid system blended with PEO and lithium salts. The molecular scale mixing of components suppressed PEO crystallization while retaining conductivities of 10^{-4} S/cm at 60°C .[23]

Templating for Batteries

Several examples found in the literature specifically describe templating for the synthesis of battery electrode materials. A few illustrative examples are mentioned here. One set of templating strategies developed by Martin and coworkers began with arrays of

nanostructures using either “track-etch” polymeric membranes or porous alumina membranes as templates. The templates were removed either by solvent extraction or by thermal decomposition. Martin and co-workers showed that the membrane-based approach formed micro- and nanoscale “brush” electrodes for lithium batteries.[24, 25] This work will be discussed in more detail in the section related to electrochemistry of vanadium oxides, although this strategy was also used for the synthesis of LiMn_2O_4 for cathodes and tin oxide materials for anodes.[26-28]

In recent work, Nam *et al.* used viruses to self-assemble nanowires and 2D organized nanowire ensembles of cobalt oxide, Co_3O_4 and gold-cobalt oxide by exploiting the carboxylic acid-containing side chains of the viruses. These nanowires showed improved capacities over micronscale powders of the same chemistry.[29]

Previous use of block copolymers to prepare battery architectures provided a valuable basis for this work as well. Polymers similar to those designed by Cohen’s group, 5-norbornene-2,3-dicarboxylic acid and 1,4,7,10 Tetraoxacyclotetradec-12-ene incorporated LiMn_2O_4 at room temperature by mixing Li and Mn acetate salts in a solution of polymer dissolved in tetrahydrofuran (THF). These systems were cycled with liquid electrolyte and reversible capacities of ~ 25 mAh/g for over 600 cycles were achieved (current rate not specified).[30]

Work by our laboratory has explored development of a self-organizing nanocomposite anode using a block copolymer of poly(oxyethylene)₉ methacrylate-*block*-poly(methyl) methacrylate, POEM-*b*-PMMA.[31] That system incorporated surfactant-treated single-walled nanotubes and a lithiated gold salt. *In situ* metallothermic reduction of the salt formed particles of metallic gold that alloyed with lithium. The resulting electrode cycled repeatedly at rates between C/1.8 and 8.8C (see definition of C-rate in Chapter 1).

Vanadium Oxide and Vanadium Oxide Architectures

Vanadium oxide has been studied extensively as an insertion cathode material for lithium ion batteries due to its stability, relative safety, low cost, ease of synthesis, and high energy density. Vanadium oxide can be produced through several different synthetic routes, including solid-state reactions involving decomposition of ammonium vanadate NH_4VO_3 . [32] This work focuses on amorphous (low-crystalline) vanadium oxides

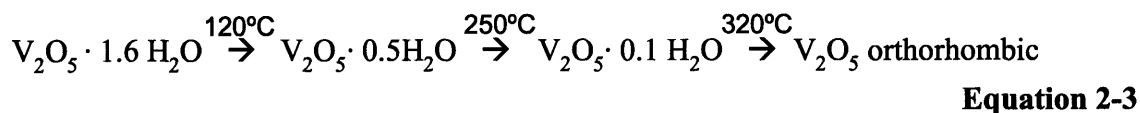
synthesized using sol-gel chemistry. Sol-gel chemistry is desirable due to the ease of synthesis, room temperature processing, access to high surface area materials, and, in this case, the hydrophilic solution phase which is essential for the templating of the composite. Vanadium oxide could be used as a non-lithiated TMO versus metallic lithium because of the polymer electrolyte's stability in the presence of lithium. Any of the high temperature processes used to produce lithiated transition metal oxides (TMOs) could result in decomposition of the polymer phase. This section will describe several sol-gel techniques for the synthesis of vanadium oxide and the resulting oxide morphologies, while the next section will focus on the electrochemistry of these systems.

Sol-gel chemistry, developed for many silicon based materials but also other TMOs, is characterized by hydrolysis and condensation reactions forming the final structure from a gel rather than crystallization or precipitation. The earliest description of sol-gel science, found in 1846, related to SiO₂, but its versatility has increased over the past 150 years.[33] The colloidal suspension that makes up the sol can be made of pre-hydrolyzed particles that bond via covalent, van der Waals or hydrogen bonding forces in the gelled network. The final product forms by aging and drying steps which again offer variety in the resulting structure. Mild reaction conditions characterize sol-gel chemistry, including: low temperature, easy modification and simple processing.

Vanadium oxide sol-gel can be produced by either an aqueous route involving metal salts resulting in vanadic acid, or vanadyl alkoxides, involving metal-organic precursors, where water serves only as a reactant. The hydrolysis step of the reaction, catalyzed by water, creates reactive M-OH groups, which condense to metal-oxygen-metal bonds forming a connecting TMO network according to the reactions found in Equation 2-1 and Equation 2-2.



Much work in vanadium oxide sol-gel chemistries has been done by Jacques Livage since the 1990s.[32] Altering the ratio between water and vanadium pentoxide affects the product of this reaction. Using high water-to-inorganic ratios lead to ribbon-like particles of $V_2O_5 \cdot nH_2O$ structures similar to those obtained from the aqueous vanadic acid synthesis, while smaller amounts of water lead to unhydrolyzed alkoxy groups that remain as ligands bonded to the oxide network. Water in the final structure of $V_2O_5 \cdot nH_2O$ can take on several different forms: higher amounts of H_2O per V_2O_5 are weakly bound and n can be reversibly varied between about $n= 0.5$ and $n = 1.6$. Below $n = 0.5$ dehydration is less reversible: water can be removed through heating up to $250^\circ C$. Finally, water is chemically bound at levels of $0.1 H_2O$ per V_2O_5 , and liberated only above the crystallization temperature, which gives orthorhombic vanadium oxide. Reactions with water are given in Equation 2-3.[32]



The final sol-gel structure consists of ribbon-like polymeric species with dimensions of approximately $100 \times 10 \times 1$ nm. The acidification route from sodium metavanadate involves an ion exchange step, which increases in viscosity over time. The formation of the ribbon V_2O_5 network stems from the condensation of V-OH groups of the hexacoordinated species $[VO(OH)_3(OH_2)_2]^0$. [32] Two reactions govern the final structure (Figure 2-3), fast olation reactions along the HO-V-OH₂ (y-axis) direction and slower oxolation reactions along the HO-V-OH direction (x-axis), with a double bonded O along the z-axis (where condensation will not occur). Increasing the amount of water favors M — OH groups over M — O — M groups.[34] The polarity and viscosity of the solvent will also affect the reaction rate and the structure of final material.[35]

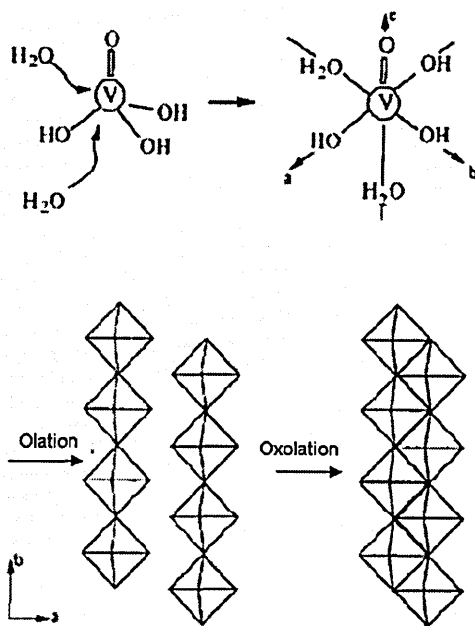


Figure 2-3: Formation of V_2O_5 from sol gel process a) coordination expansion b) condensation. Reproduced from Livage. [36]

The surface area of the final sol-gel vanadium oxide can be controlled by altering the way the solvent phase is removed, through techniques including supercritical drying[37], freeze-drying[38], or solvent exchange.[39, 40] This variation in surface area arises due to the surface tension forces that develop at the interface between the evaporating liquid phase and the gas phase. When deposited onto a flat substrate and *dried in air*, vanadium pentoxide gels give rise to **xerogel** layers that exhibit a preferred orientation, a surface area of $10 \text{ m}^2/\text{g}$, and particle size between $4 - 40 \text{ }\mu\text{m}$. Large capillary forces exerted on the gel structure at the liquid-gas interface collapse the porous structure during the pore fluid's evaporation in air. Intercalation of ions occurs readily at room temperature within a few minutes when the gel is dipped into an aqueous solution of ionic salts. This addition does not destroy the internal structure of the oxide network or the one-dimensional stacking of the V_2O_5 ribbons.

Aerogels, created by *supercritical drying* processes, possess highly interconnected, bicontinuous structures of solid phase and pores. Supercritical drying replaces the solvent with a gas under conditions that prevent pores from collapsing via capillary forces. The liquid is removed above the critical point where there is no surface tension. The first aerogels, formed by Hirashima *et al.* from $VO(OEt)_3$ supercritical

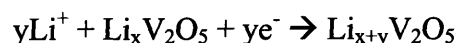
drying of ethanol at 255°C at 210 atm, were crystallized.[42] The use of supercritical CO₂ to form aerogels was developed by Chaput *et al.* with VO(OPrⁱ)₃ in acetone.[37] The thickness of the solid phase surrounding the pores is in the range of 10-30 nm, with a high surface area of 450 m²/g. The porous structure allows certain electrolytes to penetrate within the aerogel particles and the material's thin solid phase reduces the length of ionic diffusion paths for the intercalated ions.[43-45] The characteristic mesoporosity of these materials provides both molecular accessibility and rapid mass transport via diffusion.[46]

Another approach towards an aerogel-like material, termed an **ambigel**, consists of a sequence of *solvent exchange steps* in which the new solution is miscible with the previous one and its surface tension is lower than the previous one. For example, exchanging water with acetone and then hexane, leads to an organogel that, when dried by evaporation below the critical point, generates a material with a surface area of 200 m²/g.[39, 40]

Other nanoscale microstructures for vanadium oxide to increase capacity and rate capability have included nanotubes, nanorolls and nanowires. Wang *et al.* have reviewed the properties of nanostructured vanadium oxides including nanotubes, nanorolls, nanoarrays and nanobelts.[47] Singhal *et al.* have seen increased capacity in partially crystalline nanoparticles of vanadium oxide produced using the combustion flame-chemical vapor condensation process.[48] Further background on these nano-architected vanadium oxides will be presented in the next section.

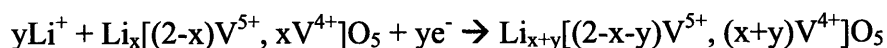
Electrochemistry of Vanadium Oxide

The overall reaction for the insertion of lithium into vanadium oxide particles is:



Equation 2-4

or with the valence state of vanadium taken into consideration this equation becomes (where x and y are the fractions of Li, V⁴⁺ and V⁵⁺ valence upon lithation):



Equation 2-5

The valence shift in vanadium oxide indicated above is necessary for electronic conduction, which occurs via electron hopping between V^{4+} and V^{5+} ions. Electrical conductivity increases with the amount of V^{4+} states, for example at 1% V^{4+} , $\sigma_{300} = 4 \times 10^{-5}$ S/cm while at 10% V^{4+} , $\sigma_{300} = 2 \times 10^{-3}$ S/cm.[34]

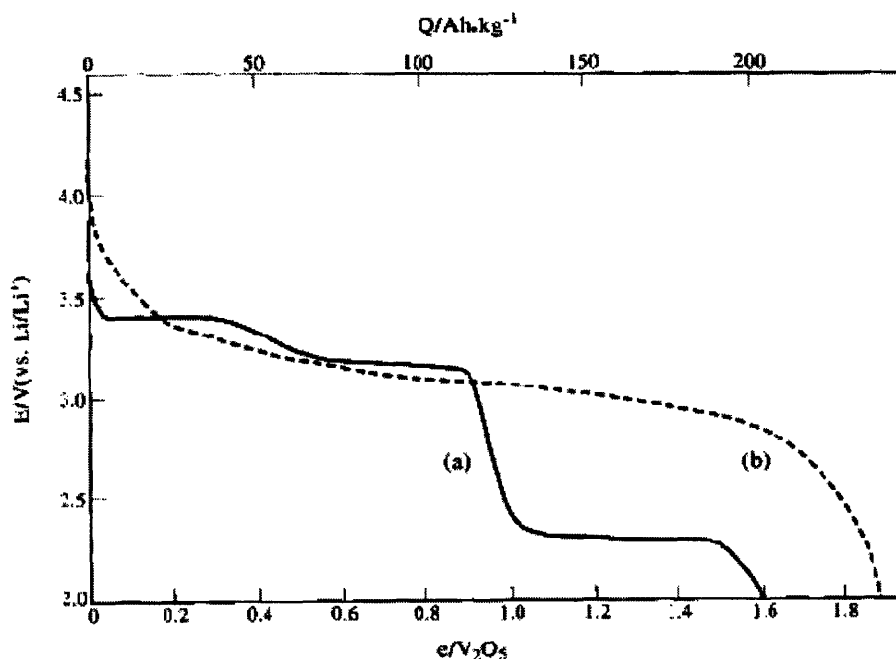


Figure 2-4: Discharge curve of a) crystalline V_2O_5 b) xerogel of V_2O_5 . Reproduced from Livage *et al.*[34]

A typical discharge curve for vanadium oxide is shown in Figure 2-4. Amorphous vanadium oxide has higher reversible Li^+ storage capability than the crystalline form, for example up to 4 moles of lithium can be reversibly inserted, as compared to 1.8 for crystalline forms. Sol-gel vanadium oxides were reported to have electroactive capacities up to 100% greater than polycrystalline non-porous V_2O_5 powders and superior rate capabilities compared to usual V_2O_5 powders.[41] Batteries containing vanadium oxide as a cathode material suffer loss of capacity when discharged to below 2V.[49] The sloped (as compared to discrete plateaus) discharge profile shown above is unique to amorphous (low-crystalline) systems. The intercalation of metal cations and solvent in these materials increases the spacing between amorphous ribbons which accommodates

more diffusant. Crystalline V_2O_5 exhibits several plateaus corresponding to several phase equilibria in $Li_xV_2O_5$, which may inhibit reversibility or rate capability. For sol-gel systems, a single plateau is present at around 3.1 V.

The theoretical specific capacity for one mole insertion of lithium into V_2O_5 is 147 mAh/g. Experiments have shown that a cutoff voltage of 2.5 V vs Li/Li^+ , $x = 1$ corresponds to a capacity of 147 mAh/g V_2O_5 . [50] This value can be increased by expanding the cycling limits of the system and by architecture modifications as discussed above. The rate capability can also be maximized through adjustments in architecture. Work by Rolison, Dunn, and coworkers in aerogel systems have shown only a 25% decrease in capacity with rate increases from C/40 to C/4. [45] Recently, Baudrin *et al.* have used the vanadium oxide aerogel structure to access a metastable phase with capacities in excess of 500 mAh/g. [51]

There are some advantages to ambigels over that of aerogels as cathode materials. A portion of aerogel interfaces may not be electrifiable, as their small pores are not accessible to ions and solvent on an electrochemical time scale. Results have indicated that ambigels contain a narrow pore size distribution ($\sim 25 \pm 10$ nm) and may therefore exhibit improved overall capacitance over aerogels. Pore size in ambigels are generally between 10 and 30 nm, where electrolyte penetration is facile, and only a small fraction of the pore volume arises from pores with diameters smaller than 5 nm, unlike aerogels. [46] Because vanadium oxides have low electronic conductivity, a conductivity additive remains necessary even with aerogel and ambigel morphologies. This can be simply achieved by crushing and mixing the TMO on a macroscale with carbon black. Other techniques developed by Rolison and coworkers involve mixing acetylene black and wax, termed “sticky carbon black”, with the oxide. [46]

Martin and coworkers produced nanostructured V_2O_5 with high Li-insertion rate capability and improved volumetric charge capacity by membrane-template synthesis. [52] Nanostructured electrodes were prepared by depositing an alkoxide V_2O_5 precursor, such as vanadyl triisopropoxide, within the pores of the etched template membranes. The resulting electrodes consisted of V_2O_5 nanofibrils protruding from a Pt current collector surface like bristles of a brush. In this work, two methods were used to increase volumetric capacity. First, chemically etching the template membrane in NaOH

prior to synthesis (of the V_2O_5 within the pores of the membrane) increased the pore diameter and thereby porosity of the membrane. The second method applied additional V_2O_5 precursor to the nanostructured electrodes prepared from the etched membranes.[50] Results from materials designed in the latter way delivered three times the capacity of thin film electrodes at high discharge, some cycled at over 1000C. More recently, this group has compared the electrochemical performance of 70 nm-sized diameter nanofibers to that of micrometer-sized diameters at low temperature to show that the smaller particle size can address the slow electrochemical kinetics and reduced solid-state diffusion at low temperature. The smaller diameter 70 nm fibers showed increased rate performance over the larger fibers at low temperatures, with the largest improvement seen with current rates of 40C run at -25°C where the cathode composed of 70 nm fibers delivered twice the capacity.[53]

Groups have also reported the incorporation of poly(ethylene oxide) within sol-gel derived V_2O_5 . Work by West *et al.* saw improved mechanical properties but decreased cyclability in films incorporating PEO.[49] Liu *et al.* investigated the structure and reactions of PEO-intercalation in V_2O_5 describing an interlayer expansion of up to 7.7 \AA with an Li:EO ratio of 1:8.82. This expansion provided for enhanced ion insertion.[54]

Other forms of vanadium oxide that have been produced through sol-gel chemistry demonstrated improved capacities when compared to traditional methods. $\text{Li}_{1+\alpha}\text{V}_3\text{O}_8$ was prepared via sol-gel routes and the phase formation upon heating at 350°C has lead to capacities with large first discharges of $\sim 300 \text{ mAh/g}$, which decreased upon further cycling. In this procedure gelation was obtained after reacting V_2O_5 with $\text{LiOH}\cdot\text{H}_2\text{O}$ at 50°C for several days. The resulting structure was a mix of solid and liquid phases with partial crystallinity.[55]

Vanadium Oxide Nanotube and Nanowire Structures

Spahr *et al.* produced vanadium oxide nanotubes and nanorolls from vanadyl triisopropoxide by a ligand-assisted templating approach using hexadecylamine.[56] These tubes consisted of several concentric shells each 2.8-3 nm in thickness (with some structural instability). After mixing the nanotubes and rolls with carbon black, these batteries achieved capacities of 120 mAh/g with some reversibility.[57] Nanoroll

anisotropy may be useful for certain applications and recently Sun *et al.* have shown that the wall structure and defect content play a role in the electrochemical properties. Defect-rich nanorolls, which behaved like sol-gel partially crystalline V_2O_5 , showed increases in specific capacity, while the well-ordered nanorolls showed crystalline-like plateaus in their discharge profiles.[58] The group hypothesized that the defects provided additional Li-ion redox sites resulting from atomic-scale disorder.

Recently, researchers at Stanford studied Li^+ insertion in one-dimensional vanadium oxide nanowires synthesized by chemical vapor transport methods. They showed improved phase transformation of the oxide on this size scale enabling complete delithiation of $Li_3V_2O_5$ (the ω phase) to pristine V_2O_5 for these nanoscale structures, citing a factor of 3 improvement in the Li^+ diffusion constant compared to bulk materials.[59]

Electronic Conductivity

As has been mentioned previously, high electronic conductivity in the cathode is vital to a working battery and using vanadium oxide as a cathode material requires the addition of a conductivity additive, except in the case of thin films. Lower electronic conductivity leads to severe ohmic polarization losses that reduce the useful voltage of the cell. In addition, the intrinsic electronic conductivity of vanadium oxide will change upon the insertion of Li ions. Several approaches to increasing electronic conductivity have been addressed in the literature, and the following examples serve to illustrate some of the possibilities. Overall, carbon black is most prevalent as a conductivity additive in these systems because of its low density, high conductivity, and low cost/wide availability.

Huang *et al.* prepared nanocomposites by chemically wiring both polyethylene glycol(PEG) and the active metal oxide V_2O_5 onto the surface of semigraphitic carbon black nanoparticles that serve as an electronically conductive core.[60] V_2O_5 sol was coated onto PEG-grafted carbon nanoparticles, and the system was dried at 140°C.

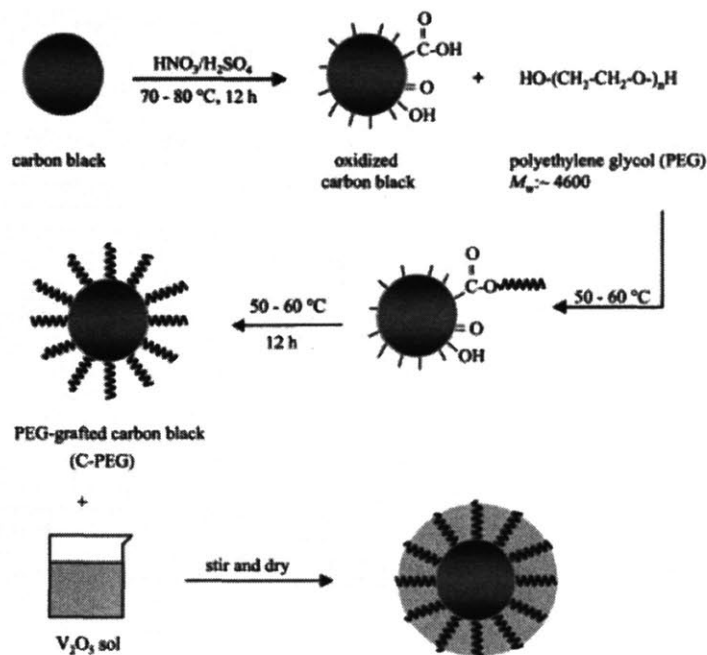


Figure 2-5: Process for coating V_2O_5 on PEG-carbon nanoparticles. Reproduced from Huang *et al.* [60]

Sakamoto and Dunn have used single-wall carbon nanotubes for electronic conductivity along with V_2O_5 aerogel as the active material. These show increased rate capability when compared to aerogel V_2O_5 mixed with carbon black.[61] They point to the similarity in morphology between the nanotubes and the aerogel structure of sol-gel vanadium oxide that enables contact between the two phases at the nanometer length scale.

Doping of V_2O_5 with other metal ions, such as copper and silver, by direct redox reaction to increase electronic conductivity was reported by Coustier *et al.*[62] Their materials exhibited improved rate capability and kinetic behavior, with capacities up to 400 mAh/g for AgV_2O_5 [63]. Their study used a lithium perchlorate electrolyte in a cell cycled between 1.5 and 4 V at a C/40 rate. The discharge rate was calculated assuming the full capacity of the doped V_2O_5 to be four equivalents of lithium per mole of material (560 mAh/g for V_2O_5). Work by Zhang *et al.* incorporated RuO_2 nanoparticles to form an electronically conductive material.[64] Doping increased electronic conduction and also improved cycle life, as the metallic species acted as pillars between vanadium oxide layers. Morcrette *et al.*, while using copper as a dopant, observed large metallic extrusions that emerged upon discharge and reversibly disappeared upon charge, with

270 mAh/g of capacity.[65] However, these doped materials still required the addition of carbon black to further boost their conductivity.

A final approach to conductivity using carbon has been the carbon coating of TMO particles. Odani *et al.* have circumvented the need for carbon black additive by producing carbon-coated vanadium oxide through their RAPET method (reaction under autogenic pressure at elevated temperatures) using a vanadyl alkoxide precursor.[66] Sides *et al.* have used similar carbonization strategies to improve the conductivity of LiFePO₄ systems.[67] In the vanadium oxide system, unlike the iron phosphate system, there is a balance between preserving the graphitized carbon from pyrolyzed hydrocarbons in the system and avoiding reduction of the Li⁺ insertion material V₂O₅ to less desirable oxides such as VO₂ and V₂O₃. Therefore, for vanadium oxide an additional oxidation step is needed. Heating vanadium oxide structures has been studied to further understanding of the Li⁺ insertion mechanisms. Work by Swider-Lyons *et al.* has shown that heating in O₂/H₂O gives higher Li⁺ capacity than heating under Ar/ H₂O, which they attribute to higher concentration of cation vacancies.[68]

Conjugated Polymers

This section will describe the use of conjugated polymers as conductivity additives. The majority of these systems are p-type hole-injecting materials, and their conductivity results from delocalization of electrons along the backbone in their oxidized form. Several polymers have been combined with various TMOs including polypyrrole (Ppy), polyaniline (PANI), and poly (3,4-ethylene dioxythiophene) (PEDOT). The mechanism for conduction involves mixed conduction between the oxide and the polymer. In the case of vanadium oxide there is electron hopping between V⁴⁺ and V⁵⁺ while the polymer conducts by movement of charge carriers (polarons and bipolarons) generated in an oxidized polymer. Once reduced, they no longer conduct electrons, but in oxidized form they are a conduit for electron transfer. In these hybrid organic/inorganic composites, the conducting polymers serve to increase the interlayer spacing of the TMO to provide more room for lithium ion insertion (as shown with PEO intercalation) as well as increasing conductivity. An important factor when using conjugated polymers is the necessary transport of counter ions to maintain charge neutrality of the doped polymer. The performance can be limited by mobility of these ions.[69] In addition to acting as a

conductivity additive, these polymers also enhance the binding of the composite cathode and substitute for alternative polymer binders.

Polypyrroles have been combined with several TMOs including V_2O_5 , by techniques such as *in situ* chemical polymerization (oxidation by TMO), simultaneous V_2O_5 and Ppy electropolymerization or deposition processes.[70] Studies incorporated pyrrole monomer via *in situ* oxidative polymerization with sol-gel vanadium oxide.[71] This resulted in Ppy intercalation within the interlayers of V_2O_5 (partial reduction of V^{5+} to V^{4+} that oxidizes Ppy) increasing the domain spacing and resulting in an increase in specific capacity from 236 to 283 Ah/kg.[71] Another synthesis of a similar PPY/ V_2O_5 composite resulted in materials cycling at 120 mAh/g up to 100 cycles at 0.1 mA/cm² *without* the use of carbon black or binder. This was an important demonstration of PPY's use as a binder and electronic conductor.[72] This ability was not consistent throughout the literature, however. For example, Harreld *et al.* have also used sol-gel routes to make Ppy/ V_2O_5 systems, similarly employing supercritical drying strategies to increase surface area. Their system saw little to no improvement in conductivities or capacities without the further addition of carbon black.[73, 74] Often, as a result of these *in situ* polymerizations, V^{4+} was generated at the surface of the oxide,[72] which may effect the Li/ V_2O_5 electrochemistry.

Polyaniline is another conjugated polymer that has been used to enhance the electrochemical properties of V_2O_5 . However, carbon black was again needed to create cyclable composite cathode films.[75-78] PANI/ V_2O_5 hybrid materials prepared by oxidative intercalation reaction exhibited polymer chains lying parallel in the interlayer of V_2O_5 xerogel.[79, 80] Conductivities for V_2O_5 /PANI composites were found to be several orders of magnitude higher than the oxide alone, ranging from 10^{-2} to 10^{-6} S/cm for decreasing amounts of PANI [81] Diffusion coefficients of lithium within the hybrid structure were also improved by PANI addition.[82] For example, *in situ* oxidative polymerization of aniline in the sol solution with $VO(O^iPr)_3$ gave enhanced lithium diffusion in a PANI/ V_2O_5 composite of 2×10^{-11} over 3×10^{-12} cm²/s for diffusion in V_2O_5 alone.[78] Further work combined PEO and PANI within V_2O_5 galleries by insertion of PANI into PEO- V_2O_5 by intercalative polymerization of aniline *in situ* or by

direct intercalation of conducting polymer macromolecules (containing carbon black as well) and a slight improvement in capacity with the ternary system was observed.[77]

Poly (3,4-ethylene dioxythiophene), or PEDOT, can be oxidized, as shown in Figure 2-7, to give conductivities on the order of 100 S/cm.[83] One out of every three monomer units is oxidized. This polymer showed enhanced stability in combination with TMO cathode materials and could be substituted for carbon black for some TMO chemistries.

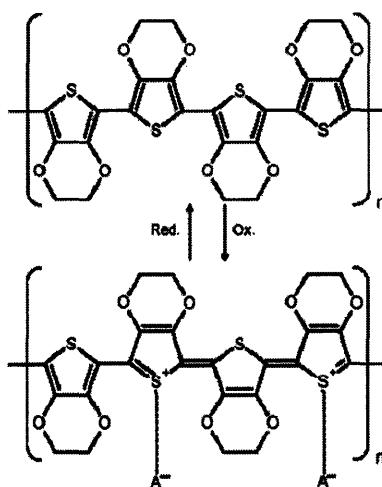


Figure 2-6: Chemical structure of poly(3,4-ethylene dioxythiophene), neutral PEDOT oxidized to form conducting polycation balanced by dopant anions. Reproduced from Lock *et al.* [83]

PEDOT has been incorporated by insertion into the V_2O_5 layers by oxidative polymerization/intercalation. Incorporation occurs by *in situ* reaction of the EDOT monomer with V_2O_5 powder. This results in one and two layers of intercalated PEDOT, as shown in Figure 2-7.[84] This structure showed enhanced discharge capacity for PEDOT/ V_2O_5 composites of 240 mAh/g compared to 140 mAh/g for pristine V_2O_5 (cathodes contained carbon black as well).[85] Although it is difficult to compare directly because the voltage ranges for each system are different, with the addition of PEDOT an approximately 30% increase in capacity is seen with even further enhancement (up to 35%) through a microwave irradiation procedure.[86, 87] This increase was attributed to increased electronic conductivity (from 9.1×10^{-5} S/cm for pristine V_2O_5 up to 3.6×10^{-3} S/cm for a PEDOT/ V_2O_5 ratio of 0.015) and more facile phase transitions.[87] The

plateaus exhibited in crystalline systems that indicate a phase transformation became more gradual, improving reversibility.

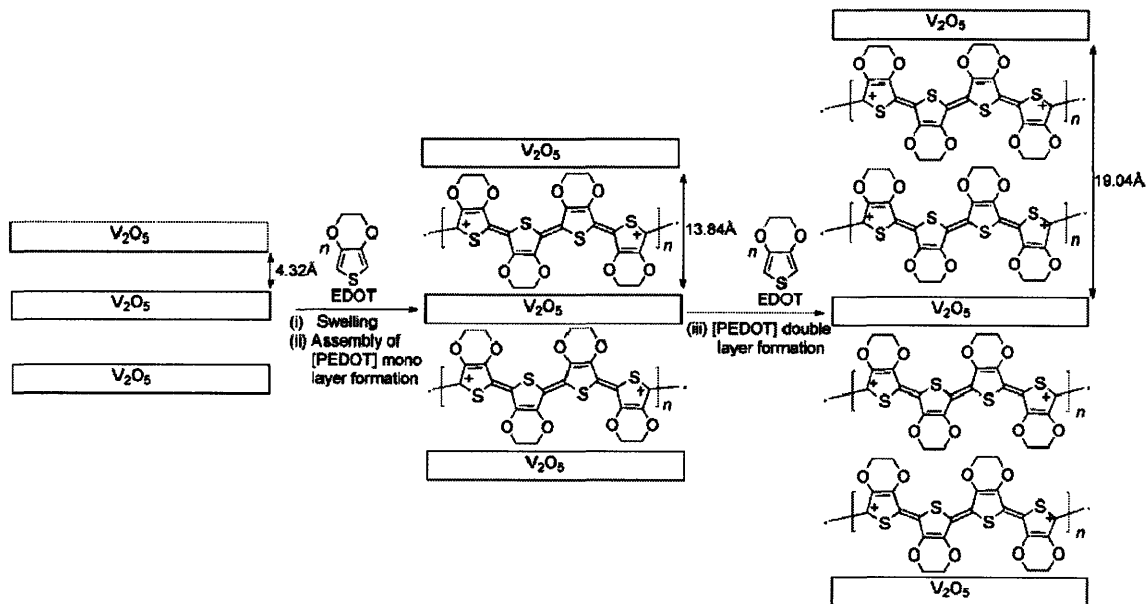


Figure 2-7: Schematic diagram of assembly of PEDOT into V₂O₅ layers. Reproduced from Murugan *et al.* [88]

Arbizanni *et al.* synthesized non-stoichiometric manganese oxide, Li_{1.03}Mn_{1.97}O₄/PEDOT, which had an open circuit voltage of 4 V. In this case, the PEDOT substituted for carbon and was also electroactive (conductive, p-type, cyclable) in the same potential range as LiMn₂O₄. [89] It further acted as the polymeric binder typically required in these systems. In this work the TMO was made via sol-gel methods and the EDOT polymerized in the same fashion as described above, by *in situ* EDOT polymerization. The non-stoichiometry of the Li_{1.03}Mn_{1.97}O₄ compound reduces the Jahn-Teller distortion that typically occurs upon cycling LiMn₂O₄ and causes capacity fading (the stoichiometric compound contains equal Mn³⁺ and Mn⁴⁺). The choice of PEDOT was quite compelling based on the controls run by this group because of PEDOT's ability to serve as a conductivity additive *substituting* for carbon black. As shown Figure 2-8, the capacity is similar for the TMO mixed with PEDOT and the TMO mixed with carbon, with the TMO/PEDOT composite showing slight improvement over TMO/CB at lower current.

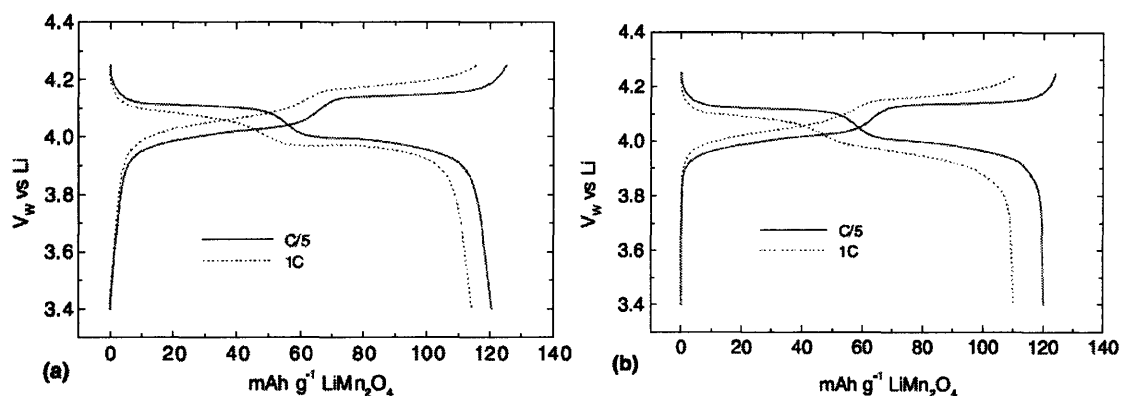


Figure 2-8: Galvanostatic charge-discharge cycles of: a) $\text{Li}_{1.03}\text{Mn}_{1.97}\text{O}_4/\text{PEDOT}$ composite electrode; b) $\text{Li}_{1.03}\text{Mn}_{1.97}\text{O}_4/\text{C}$ composite electrode at 1C and C/5. Data from Arbizzani *et al.* [89]

Summary and Introduction to the Next Chapter

This work investigates the utility of the self-organizing character of amphiphilic, graft and block copolymers to incorporate inorganic Li^+ -intercalating compounds on the nanoscale to generate cathode materials for solid-state, rechargeable batteries. The *in situ* growth of inorganic active phases in ion-conducting domains of copolymers allows for control of morphology and increases the interface-to-volume ratio, thereby reducing the distances over which both ion and electron transport must occur and increasing the maximum current that the battery can deliver. A study of the literature finds that templating inorganic compounds with copolymers offers benefits in terms of synergies between the components and control over architectures.[1, 21, 22, 90] It is also clear that altering the architecture of the TMO, vanadium oxide, offers electrochemical benefit,[43, 46, 53, 59] although the electronic conductivity of the cathode must be addressed to access this capacity. Strategies for improving electronic conductivity have included use of carbon black, carbon nanotubes, doping with metallic species and the use of conjugated polymers.

The next chapter will discuss the methods used in this work to synthesize the materials, and to characterize their morphologies and electrochemical behavior. It will then present techniques used to increase the electronic conductivity of the system.

References

1. Park, C., Yoon, J. & Thomas, E. L. "Enabling Nanotechnology with Self Assembled Block Copolymer Patterns." *Polymer*, **2003**, 44, 6725-6760.
2. Lin, Y. et al. "Self-directed self-assembly of nanoparticle/copolymer mixtures." *Nature*, **2005**, 434, 55-59.
3. Yang, P., Zhao, D., Margolese, D., Chmelka, B. F. & Stucky, G. D. "Generalized synthesis of large-pore mesoporous metal oxides with semicrystalline frameworks." *Nature*, **1998**, 396, 152-155.
4. Zhao, D., Huo, Q., Feng, J., Chmelka, B. F. & Stucky, G. D. "Nonionic Triblock and Star Diblock Copolymer and Oligomeric Surfactant Syntheses of Highly Ordered, Hydrothermally Stable, Mesoporous Silica Structures." *Journal of the American Ceramic Society*, **1998**, 120, 6024-6036.
5. Fan, J., Boettcher, S. W. & Stucky, G. D. "Nanoparticle Assembly of Ordered Multicomponent Mesostructured Metal Oxide via a Versatile Sol-Gel Process." *Chemistry of Materials*, **2006**, 18, 6391-6396.
6. Lopes, W. A. & Jaeger, H. M. "Hierarchical self-assembly of metal nanostructures on diblock copolymer scaffolds." *Nature*, **2001**, 414, 735-738.
7. Brown, G. D. & Watkins, J. J. in *Materials Research Society Proceedings* 169-174 (2000).
8. Brown, G. D., Smith, S. D. & Watkins, J. J. "Preparation of Platinum and Silver Nanoclusters via Templating Reactions in CO₂-Swollen Diblock Copolymers." *Polymeric Materials: Science and Engineering*, **2000**, 82.
9. Brown, G. D. & Watkins, J. J. "Preparation of Nanocomposites by Selective Metallization in CO₂ Swollen Cylindrical Diblock Copolymers Templates." *Polymeric Materials: Science and Engineering*, **2001**, 84.
10. Watkins, J. J., Brown, G. D. & RamachandraRao, V. S. "Phase Separation in Polymer Blends and Diblock Copolymers Induced by Compressible Solvents." *Macromolecules*, **1999**, 32, 7737-7740.
11. Cooper, A. I. "Recent Developments in Materials Synthesis and Processing Using Supercritical CO₂." *Advanced Materials*, **2001**, 13, 1110-1113.

12. Cooper, A. I. "Polymer Synthesis and Processing using Supercritical Carbon Dioxide." *Journal of Materials Chemistry*, **2000**, 10, 207-234.
13. Cieben, J. F., Clay, R. T., Sohn, B. H. & Cohen, R. E. "Brief review of metal nanoclusters in block copolymer films." *New Journal of Chemistry*, **1998**, 22, 685-691.
14. Cohen, R. E. "Block Copolymers as Templates for Functional Materials." *Current Opinion in Solid State and Materials Science*, **1999**, 4, 587-590.
15. Boontongkong, Y., Cohen, R. E. & Rubner, M. F. "Selective electroless copper deposition within block copolymer microdomains." *Chemistry of Materials*, **2000**, 12, 1628-1633.
16. Wang, T. C., Chen, B., Rubner, M. F. & Cohen, R. E. "Selective Electroless Nickel Plating on Polyelectrolyte Multilayer Platforms." *Langmuir*, **2001**, 17, 6610-6615.
17. Abes, J. I., Cohen, R. E. & Ross, C. A. "Block-copolymer-templated synthesis of iron, iron-cobalt, and cobalt-nickel alloy nanoparticles." *Materials Science & Engineering, C: Biomimetic and Supramolecular Systems*, **2003**, C23, 641-650.
18. Templin, M. et al. "Organically Modified Aluminosilicate Mesostructures from Block Copolymer Phases." *Science*, **1997**, 278, 1795-1798.
19. Ulrich, R., Du Chesne, A., Templin, M. & Wiesner, U. "Nano-objects with Controlled Shape, Size, and Composition from Block Copolymer Mesophases." *Advanced Materials*, **1999**, 11, 141-146.
20. De Paul, S. M., Zwanziger, J. W., Ulrich, R., Wiesner, U. & Spiess, H. W. "Structure, Mobility, and Interface Characterization of Self-Organized Organic-Inorganic Hybrid Materials by Solid-State NMR." *Journal of the American Chemical Society*, **1999**, 121, 5727-5736.
21. Garcia, C., Wiesner, U., DiSalvo, F., Zhang, Y. & Mahajan, M. "Self-Assembly Approach toward Magnetic Silica-Type Nanoparticles of Different Shapes from Reverse Block Copolymer Mesophases." *Journal of the American Chemical Society*, **2003**, 125, 13310-13311.

22. Garcia, C., Zhang, Y., DiSalvo, F. & Wiesner, U. "Mesoporous Aluminosilicate Materials with Superparamagnetic γ -Fe₂O₃ particles Embedded in the Walls." *Angewandte Chemie Intern. Ed.*, **2003**, 42, 1526-1530.
23. Ulrich, R. et al. "Solid hybrid polymer electrolyte networks: Nano-structurable materials for lithium batteries." *Advanced Materials*, **2002**, 14, 1134-1137.
24. Sides, C. R., Li, N., Patrissi, C. J., Scrosati, B. & Martin, C. R. "Nanoscale Materials for Lithium-Ion Batteries." *MRS Bulletin*, **2002**, 604-606.
25. Martin, C. R. "Nanomaterials: A Membrane-Based Synthetic Approach." *Science*, **1994**, 266, 1961-1966.
26. Li, N., Patrissi, C. J., Che, G. & Martin, C. R. "Rate Capabilities of Nanostructured LiMn₂O₄ Electrodes in Aqueous Electrolyte." *Journal of the Electrochemical Society*, **2000**, 147, 2044-2049.
27. Li, N., Martin, C. R. & Scrosati, B. "A High-Rate, High-Capacity, Nanostructured Tin Oxide Electrode." *Electrochemical and Solid-State Letters*, **2000**, 3, 316-318.
28. Li, N. & Martin, C. R. "A High-Rate, High-Capacity, Nanostructured Sn-Based Anode prepared by sol gel template synthesis." *Journal of the Electrochemical Society*, **2001**, 148, A164-A170.
29. Nam, K. T. et al. "Virus-Enabled Synthesis and Assembly of Nanowires for Lithium Ion Battery Electrodes." *Science*, **2006**, 312, 885-888.
30. Bullock, S. & Kofinas, P. "Nanoscale battery materials based on the self-assembly of block copolymers." *Journal of Power Sources*, **2004**, 132, 256-260.
31. Mui, S. C. et al. "Block Copolymer-Templated Nanocomposite Electrodes for Rechargeable Lithium Batteries." *Journal of the Electrochemical Society*, **2002**, 149, A1610-A1615.
32. Livage, J. "Sol-gel chemistry and electrochemical properties of vanadium oxide gels." *Solid State Ionics*, **1996**, 86-88, 935-942.
33. Brinker, J. & Scherer, G. *Sol-gel Science* Academic Press, Inc.: San Diego, CA, 1990.
34. Livage, J., Beteille, F., Roux, C., Chatry, M. & Davidson, P. "Sol-gel synthesis of oxide materials." *Acta Materialia*, **1998**, 46, 743-750.

35. Schubert, U. in *Comprehensive Coordination Chemistry II* (eds. McCleverty, J. A. & Meyer, T. J.) 629-656 (Elsevier Science Ltd, Amsterdam, 2004).
36. Livage, J. "Sol-gel Ionics." *Solid State Ionics*, **1992**, 50, 307-313.
37. Chaput, F., Dunn, B., Fuqua, P. & Salloux, K. "Synthesis and Characterization of Vanadium Oxide Aerogels." *Journal of Non-Crystalline Solids*, **1995**, 188, 11-18.
38. Sudant, G., Baudrin, E., Dunn, B. & Tarascon, J. M. "Synthesis and Electrochemical Properties of Vanadium Oxide Aerogels Prepared by a Freeze Drying Process." *Journal of the Electrochemical Society*, **2004**, 151, A666-A671.
39. Harreld, J. H., Dong, W. & Dunn, B. "Ambient Pressure Synthesis of Aerogel-like Vanadium oxide and molybdenum oxide." *MRS Bulletin*, **1998**, 33, 561-567.
40. Coustier, F., Lee, J.-M., Passerini, S. & Smyrl, W. H. "V₂O₅ aerogel-like lithium intercalation host." *Solid State Ionics*, **1999**, 116, 279-291.
41. Coustier, F., Passerini, S. & Smyrl, W. H. "A 400mAh/g Aerogel-like V₂O₅ cathode for rechargeable lithium batteries." *Journal of the Electrochemical Society*, **1998**, 145, L73-L74.
42. Sudoh, K. & Hirashima, H. "Preparation and Physical Properties of V₂O₅ Aerogel." *Journal of Non-Crystalline Solids*, **1992**, 147-148, 386-388.
43. Passerini, S., Ressler, J. J., Le, D. B., Owens, B. B. & Smyrl, W. H. "High rate of electrodes of V₂O₅ aerogel." *Electrochimica Acta*, **1999**, 44, 2209-2217.
44. Liu, P., Zhang, J.-G., Tracy, C. E. & Turner, J. A. "Electrochemical Deposition of Vanadium Oxide in the Presence of Surfactants." *Electrochemical and Solid-State Letters*, **2000**, 3, 163-166.
45. Rolison, D. R. & Dunn, B. "Electrically conductive Oxide Aerogels: new materials in electrochemistry." *Journal of Materials Chemistry*, **2001**, 11, 963-980.
46. Dong, W., Rolison, D. R. & Dunn, B. "Electrochemical Properties of High Surface Area Vanadium Oxide Aerogels." *Electrochemical and Solid-State Letters*, **2000**, 3, 457-459.
47. Wang & Cao, G. "Synthesis and Enhanced Intercalation Properties of Nanostructured Vanadium Oxides." *Chemistry of Materials*, **2006**, 18, 2787-2804.
48. Singhal, A. et al. "Nanostructured Electrodes for Next Generation Rechargeable Electrochemical Devices." *Journal of Power Sources*, **2004**, 129, 38-44.

49. West, K., Zachau-Christiansen, B., Jacobsen, T. & Skaarup, S. "Vanadium Oxide Xerogels as Electrodes for Lithium Batteries." *Electrochimica Acta*, **1993**, 38, 1215-1220.
50. Patrissi, C. J. & Martin, C. R. "Improving the Volumetric Energy Densities of Nanostructured V_2O_5 Electrodes Prepared Using the Template Method." *Journal of the Electrochemical Society*, **2001**, 148, A1247-A1253.
51. Baudrin, E., Sudant, G., Larcher, D., Dunn, B. & Tarascon, J. M. "Preparation of Nanotextured $VO_2[B]$ from Vanadium Oxide Aerogels." *Chemistry of Materials*, **2006**, 18, 4369-4374.
52. Patrissi, C. J. & Martin, C. R. "Sol-Gel-Based Template Synthesis and Li-Insertion Rate Performance of Nanostructured Vanadium Pentoxide." *Journal of the Electrochemical Society*, **1999**, 146, 3176-3180.
53. Sides, C. R. & Martin, C. R. "Nanostructured Electrodes and the Low-Temperature Performance of Li-ion Batteries." *Advanced Materials*, **2005**, 17, 125-128.
54. Liu, Y. J. et al. "Synthesis, Structure, and Reactions of Poly(ethylene oxide)/ V_2O_5 Intercalative Nanocomposites." *Chemistry of Materials*, **1996**, 8, 525-534.
55. Dubarry, M. et al. "Sol Gel Synthesis of $Li_{1+a}V_3O_8$ from Precursors to Xerogel." *Chemistry of Materials*, **2005**, 17, 2276-2283.
56. Spahr, M. E., Stoschitzki-Bitterli, P., Nesper, R., Haas, O. & Novak, P. "Vanadium Oxide Nanotubes." *Journal of the Electrochemical Society*, **1999**, 146, 2780-2783.
57. Norlinder, S., Edstrom, K. & Gustafsson, T. "The Performance of Vanadium Oxide Nanorolls as Cathode Material in a Rechargeable Lithium Battery." *Electrochemical and Solid-State Letters*, **2001**, 4, A129-A131.
58. Sun, D. et al. "The Relationship between Nanoscale Structure and Electrochemical Properties of Vanadium Oxide Nanorolls." *Advanced Functional Materials*, **2004**, 14, 1197-1204.
59. Chan, C. K. et al. "Fast, Completely Reversible Li Insertion in Vanadium Pentoxide Nanoribbons." *Nano Letters*, **2007**, 7, 490-495.

60. Huang, H. & Nazar, L. F. "Grafted Metal Oxide/Polymer/Carbon Nanostructures Exhibiting Fast Transport Properties." *Angewandte Chemie Intern. Ed.*, **2001**, 40, 3880-3884.
61. Sakamoto, J. S. & Dunn, B. "Vanadium Oxide-Carbon Nanotube Composite Electrodes for Use in Secondary Lithium Batteries." *Journal of the Electrochemical Society*, **2002**, 149, A26-A30.
62. Coustier, F., Hill, J., Owens, B. B., Passerini, S. & Smyrl, W. H. "Doped Vanadium Oxides as Host Materials for Lithium Intercalation." *Journal of the Electrochemical Society*, **1999**, 146, 1355-1360.
63. Owens, B. B., Passerini, S. & Smyrl, W. H. "Lithium Ion Insertion in Porous Metal Oxides." *Electrochimica Acta*, **1999**, 45, 215-224.
64. Zhang, F., Passerini, S., Owens, B. B. & Smyrl, W. H. "Nanocomposites of V₂O₅ aerogel and RuO₂ as cathode materials." *Electrochemical and Solid-State Letters*, **2001**, 4, A221-A223.
65. Morcrette, M. et al. "A reversible copper extrusion-insertion electrode for rechargeable Li batteries." *Nature Materials*, **2003**, 2, 755-761.
66. Odani, A. et al. "Testing Carbon-Coated VO_x Prepared vis Reaction under Autogenic Pressure at Elevated Temperature as Li-Insertion Materials." *Advanced Materials*, **2006**, 18, 1431-1436.
67. Sides, C. R., Croce, F., Young, V. Y., Martin, C. R. & Scrosati, B. "A High-Rate, Nanocomposite LiFePO₄/Carbon Cathode." *Electrochemical and Solid-State Letters*, **2005**, 8, A484-A487.
68. Swider-Lyons, K. E., Love, C. T. & Rolison, D. R. "Improved Lithium Capacity of Defective V₂O₅ Materials." *Solid State Ionics*, **2002**, 152-153, 99-104.
69. Skotheim, T. A., Elsenbaumer, R. L. & Reynolds, J. R. *Handbook of Conducting Polymers* M Dekker: New York, 1998.
70. Kuwabata, S., Masui, S. & Yoneyama, H. "Charge-discharge properties of composites of LiMn₂O₄ and polypyrrole as positive electrode materials for 4V class of rechargeable Li batteries." *Electrochimica Acta*, **1999**, 44, 4593-4600.

71. Huguenin, F., Giroto, E., Torresi, R. M. & Buttry, D. A. "Transport properties Of V_2O_5 /polypyrrole nanocomposite prepared by a sol-gel alkoxide route." *Journal of Electroanalytical Chemistry*, **2002**, 536, 37-45.
72. Kuwabata, S., Masui, S., Tomiyori, H. & Yoneyama, H. "Charge-discharge properties of chemically prepared composites of V_2O_5 and polypyrrole as positive electrode materials in rechargeable Li batteries." *Electrochimica Acta*, **2000**, 46, 91-97.
73. Harreld, J. H., Dunn, B., Cheng, W., Leroux, F. & Nazar, L. F. in *Materials Research Society Symposium Materials* (1998).
74. Harreld, J. H., Wong, H. P., Dave, B. C., Dunn, B. & Nazar, L. F. "Synthesis and properties of polypyrrole-vanadium oxide hybrid aerogels." *Journal of Non-crystalline Solids*, **1998**, 225, 319-324.
75. Ryu, K. S. et al. "Polyaniline doped with dimethylsulfate as a polymer electrode for all solid-state power source system." *Solid State Ionics*, **2004**, 175, 759-763.
76. Malta, M., Louarn, G., Errien, N. & Torresi, R. M. "Nanofibers composite vanadium oxide/polyaniline: synthesis and characterization of an electroactive anisotropic structure." *Electrochemistry Communications*, **2003**, 5, 1011-1015.
77. Posudievsky, O. Y., Biskulova, S. A. & Pokhodenko, V. D. "New hybrid guest-host nanocomposites based on polyaniline, poly(ethylene oxide) and V_2O_5 ." *Journal of Materials Chemistry*, **2004**, 14, 1419-1423.
78. Leroux, F., Goward, G., Power, W. P. & Nazar, L. F. "Electrochemical Li Insertion into Conductive Polymer/ V_2O_5 Nanocomposites." *Journal of the Electrochemical Society*, **1997**, 144, 3886-3894.
79. Kang, S.-G., Kim, K. M., Park, N.-G., Ryu, K. S. & Chang, S. H. "Factors affecting the electrochemical performance of organic/ V_2O_5 hybrid cathode materials." *Journal of Power Sources*, **2004**, 133, 263-267.
80. Lira-Cantu, M. & Gomez-Romero, P. "The Organic-Inorganic Polyaniline/ V_2O_5 System Application as a High-Capacity Hybrid Cathode for Rechargeable Lithium Batteries." *Journal of the Electrochemical Society*, **1999**, 146, 2029-2033.

81. Huguenin, F., Torresi, R. M. & Buttry, D. A. "Lithium Electroinsertion into an Inorganic-Organic Hybrid Material Composed from V_2O_5 and Polyaniline." *Journal of the Electrochemical Society*, **2002**, 149, A546-A553.
82. Leroux, F., Koene, B. E. & Nazar, L. F. "Electrochemical Lithium Intercalation into a Polyaniline/ V_2O_5 Nanocomposite." *Journal of the Electrochemical Society*, **1996**, 143, L181-L183.
83. Lock, J. P., Im, S. G. & Gleason, K. K. "Oxidative Chemical Vapor Deposition of Electrically Conducting Poly(3,4-ethylenedioxythiophene) Films." *Macromolecules*, **2006**, 39, 5326-5329.
84. Kwon, C.-W. et al. "Poly(3,4-ethylenedioxythiophene) V_2O_5 hybrids for lithium batteries." *Electrochemistry Communications*, **2002**, 4, 384-387.
85. Murugan, A. V. et al. "Electrochemical lithium insertion into a poly(3,4-ethylenedioxythiophene)PEDOT/ V_2O_5 nanocomposite." *Journal of Power Sources*, **2002**, 105, 1-5.
86. Murugan, A. V. et al. "A novel approach to prepare poly(3,4-ethylenedioxythiophene) nanoribbons between V_2O_5 layers by microwave irradiation." *Journal of Physical Chemistry B*, **2004**, 108, 10736-10742.
87. Murugan, A. V. "Electrochemical properties of microwave irradiated synthesis of poly(3,4-ethylenedioxythiophene)/ V_2O_5 nanocomposites as cathode materials for rechargeable lithium batteries." *Electrochimica Acta*, **2005**, 50, 4627-4636.
88. Murugan, A. V., Kale, B. B., Kwon, C.-W., Campet, G. & Vijayamohanan, K. "Synthesis and characterization of a new organo-inorganic poly(3,4-ethylene dioxythiophene) PEDOT/ V_2O_5 nanocomposite by intercalation." *Journal of Materials Chemistry*, **2001**, 11, 2470-2475.
89. Arbizzani, C., Mastragostino, M. & Rossi, M. "Preparation and Electrochemical Characterization of a polymer $Li_{1.01}Mn_{1.97}O_4$ /pEDOT Composite Electrode." *Electrochemistry Communications*, **2002**, 4, 545-549.
90. Abes, J. I., Cohen, R. E. & Ross, C. A. "Selective growth of cobalt nanoclusters in domains of block copolymer films." *Chemistry of Materials*, **2003**, 15, 1125-1131.

Chapter 3 : Processing and Characterization Techniques

This chapter describes the synthesis and characterization techniques used in this research. The first portion describes the synthesis and characterization of the copolymers and then describes the methods used to create the composite films. The second section presents techniques used towards improved electronic conductivity and provides explanation of the electrochemical analysis techniques performed on the films. Finally, the methods and instrumentation used for *in situ* and *ex situ* characterization are detailed.

Polymer synthesis

Materials

The materials used in the synthesis of the block copolymer were butyl methacrylate, poly(ethylene glycol) methyl ether methacrylate monomer (OEM) ($M_n = 475$ g/mol), 1,1,4,7,10,10-hexamethyltriethylenetetramine (HMTETA), copper (I) chloride (CuCl), and methyl-2-bromopropionate, all from Sigma Aldrich. For the graft copolymer synthesis the materials used were poly(dimethyl siloxane) monomethacrylate purchased from Gelest, 2,2'-azobisisobutyronitrile initiator (AIBN) from Sigma Aldrich, along with the PEO macromonomer as used in the block copolymer synthesis. Reagent grades of dichloromethane (DCM), benzene, and toluene were purchased from Sigma Aldrich, while ethyl acetate, hexanes, and methanol were purchased from VWR Scientific; all solvents were used as received unless otherwise specified.

Block copolymer synthesis

The block copolymer poly[(oxyethylene)₉ methacrylate]-*block*-poly(butyl methacrylate), POEM-*b*-PBMA, was synthesized by atom transfer radical polymerization (ATRP) based on work previously done in our laboratory.[1] Some departures were made from the initial procedure to achieve the desired composition. Several batches of POEM-*b*-PBMA were synthesized over the course of this dissertation research. The first several batches, used in Chapter 4, were made by the author, assisted by postdoctoral researcher Dr. Jong Hak Kim. Postdoctoral researcher, Dr. Ikuo Tanaguichi made the final batch. Forty-eight mL (300 mmol) of butyl methacrylate was purified by passing through a basic alumina column to remove an inhibitor and combined with 96 mg (1 mmol) of

CuCl catalyst and 262 μL (1 mmol) of HMTETA ligand. The solution was capped with a rubber stopper and purged with argon for 20 minutes. The injection of 80 μL (0.3 mol) of the initiator, methyl-2-bromopropionate (monomer: initiator ratio 1,000:1 on a molar basis) began the polymerization reaction. The system was purged for ten more minutes with Ar and then kept at 90°C. This bulk polymerization was monitored visually until the solution became viscous after about 45-50 minutes. Some iterations of the polymerization also employed the addition of 20 mL of toluene using a longer reaction time. After the first block had reacted, the polymerized butyl methacrylate (PBMA) was dissolved in DCM and precipitated in methanol, followed by washing in methanol.

The POEM block of the polymer was added in the following manner. Twelve grams of PBMA were dissolved in 25 mL of toluene and combined with 28 grams of the macromonomer, polyethylene glycol methylether methacrylate, a 9-unit oxyethylene (EO) chain terminated at one end with a methacrylate group, and having a molecular weight of 475 g/mol. Nine EO units are long enough to solvate and provide a conduction mechanism for a lithium salt such as LiCF_3SO_3 , but not so long as to allow for room-temperature crystallization, which would lower conductivity. Prior to use, the macromonomer was purified by passing through an alumina column as described above. The PBMA/toluene/OEM solution was combined with 44 mg CuCl and 244 μL HMTETA, purged with Ar for 20 minutes, and allowed to react for three to four hours at 90°C. The crude product was first precipitated in hexane and dissolved in DCM. The resulting solution was run through a basic alumina column to remove the catalyst and then dialyzed against methanol to separate unreacted monomer with a Spectra/Por 7 dialysis membrane (MW cut off 15,000). After evaporation of DCM, the resulting polymer, POEM-*b*-PBMA, was lyophilized from benzene. The weight ratio of each block was calculated from the proton NMR spectrum by integration of the peaks for methylenes adjacent to the ester linkage at 3.9-4.0 (PBMA) and 4.1 (POEM) ppm. Taking the ratio gave a final POEM:PBMA of 70:30. The molecular weight of the resulting polymer was characterized by gel permeation chromatography (GPC). Figure 3-1 shows the chemical formula of POEM-*b*-PBMA.

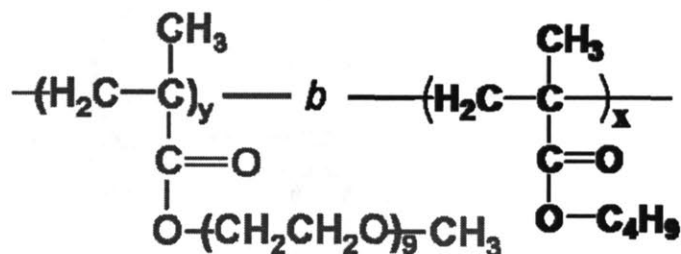


Figure 3-1: POEM-*b*-PBMA chemical structure

Graft copolymer synthesis

Another copolymer system that was investigated was the free-radically synthesized graft copolymer poly[(oxyethylene)₉ methacrylate]-*graft*-poly(dimethyl siloxane), POEM-*g*-PDMS.[2] This synthesis was carried out by either the author or by Dr. Jong Hak Kim. This material is prepared by a simple one-pot synthesis combining 6 mL of the macromonomer poly(dimethyl siloxane) monomethacrylate with 13 mL of poly(ethylene glycol) methyl ether methacrylate monomer (M_n = 475 g/mol) and 80 mL ethyl acetate. This solution was stirred and the polymerization was initiated with 6 mg of AIBN. After 30 minutes of purging with Ar, the reaction was stirred for 24 hours in a 68°C oil bath. The product was precipitated in hexane and the final composition for this system was 70:30 POEM:PDMS.

The final polymer structure is shown in Figure 3-2.

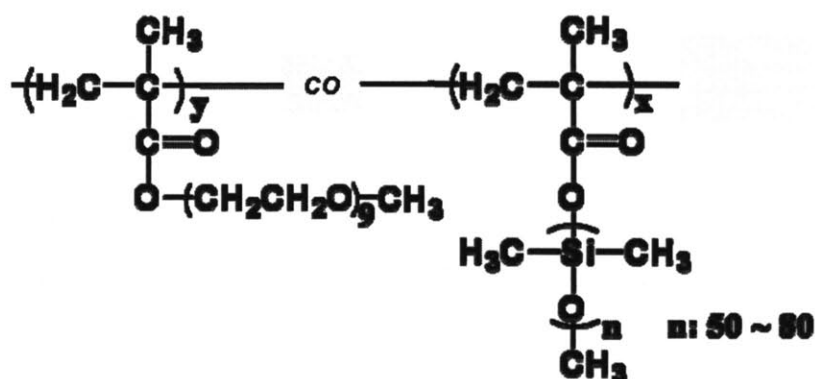


Figure 3-2: POEM-*g*-PDMS chemical structure

Active Battery material

Materials

The incorporation of active cathode material into the block and graft copolymers required the polymers (as described above), acetone (Aldrich), and the precursor, vanadyl triisopropoxide, $\text{VO}(\text{OC}_3\text{H}_7)_3$ ($\text{VO}(\text{O}^i\text{Pr})_3$) (Gelest). Polytetrafluoroethylene (PTFE) dishes (VWR Scientific) were used for film casting. Deionized (DI) water was produced using a Millipore Milli-Q unit.

Synthesis of Composite Films

Co-assembled nanocomposites were obtained by first dissolving 5 wt% polymer in acetone. Varying amounts (20-60 wt%) of the precursor $\text{VO}(\text{O}^i\text{Pr})_3$, were added to the polymer solution and the resulting solutions stirred for thirty minutes. To catalyze the sol-gel process, deionized water was added, maintaining the mole ratio of $\text{H}_2\text{O}:\text{V}$ at 40:1. After stirring for one hour the solutions were solvent cast into PTFE dishes and dried in air at room temperature under glass Petri dishes to slow the evaporation process. After air drying for at least 48 h, films were heated under vacuum at 80°C overnight to remove residual solvent. As the wet gel aged, the film color changed from dark red to green, due to partial reduction of V^{5+} to V^{4+} . [3] This procedure is shown below in Figure 3-3. The resulting films will be termed $\text{POEM-}b\text{-PBMA}/\text{VO}_x$.

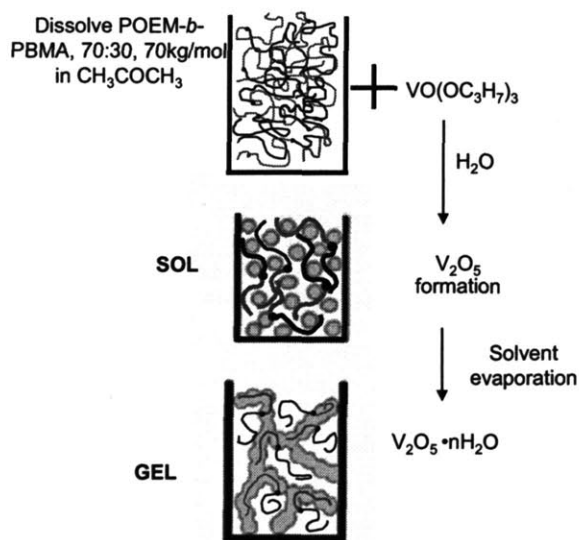


Figure 3-3: Scheme for growth of vanadium oxide *in situ* in the polymer domains to prepare composite films

Electronic Conductivity

Several approaches were taken to improve the electronic conductivity of the composite films so they could be used as cathodes in rechargeable batteries. Without any conductivity additive, the POEM-*b*-PBMA/VO_x composites provided little to no capacity when cycled galvanostatically, owing to the large ohmic resistance which results in a reduction of useful cell voltage. The following section will describe the methods used to synthesize these films.

Materials

For the carbon black procedure, fuming sulfuric acid from VWR Scientific and Super P carbon black from Cabot Corp were used. The monomer 3,4-ethylene dioxothiophene (EDOT) was obtained from Sigma Aldrich, along with other additives, including surface-modified carbon nanotubes, silver nitrate (AgNO₃), silver tetrafluoroborate (AgBF₄), and silver trifluoromethanesulfonate (AgCF₃SO₃). The nonaqueous reference electrode consisting of a silver wire in a solution of acetonitrile saturated with AgNO₃ was purchased from Ametek. Tetrabutylammonium perchlorate, (C₄H₉)₄NClO₄, (TBAClO₄), lithium perchlorate (LiClO₄), and propylene carbonate (PC) were purchased from VWR Scientific. Glass slides coated with indium tin oxide (ITO) were purchased from Delta Technologies and those coated with gold were purchased from Evaporated Metal Films Corp. Reagent grades of isopropyl alcohol (IPA), tetrahydrofuran (THF), and acetone were purchased from Sigma Aldrich. Deionized (DI) water was produced using a Millipore Milli-Q unit.

In order to cycle the films electrochemically, modifications were made to the previously described procedure so that these films could be used as cathodes in Li batteries. In all cases lithium trifluoromethanesulfonate, LiCF₃SO₃ (Sigma Aldrich) was added to 0.1 g of POEM-*b*-PBMA in the ratio 20:1 EO:Li to the polymer in the argon-filled glove box. Then the polymer/salt mixture was dissolved in 5 g acetone outside the glove box. After stirring, 0.1 g vanadyl triisopropoxide, VO(OC₃H₇)₃ (VO(OⁱPr)₃) from Gelest as before, was added to the polymer/salt mixture.

To test the salt stability in air, a solution of POEM-*b*-PBMA electrolyte in THF was doped with LiCF₃SO₃, brought out of the glove box, and cast on sputtered vanadium oxide thin films. These films were brought back into the glove box after drying for 40 min in the side arm under vacuum and made into cells with washers and lithium foil disks as described before. These showed similar behavior to films synthesized entirely inside the glove box.

Carbon Black

Films were synthesized with 5 wt% acid-treated and non-acid-treated CB acting as a conductivity additive. The scheme used to add carbon black is shown in Figure 3-4. To acidify the carbon black, the powder was refluxed with fuming sulfuric acid for one hour at 80°C.[4] After rinsing and drying steps, the carbon black was cryo-ground in liquid nitrogen to break up the particles, dried at 100°C and sonicated in acetone for 1 hour before addition to precursor/polymer solution.

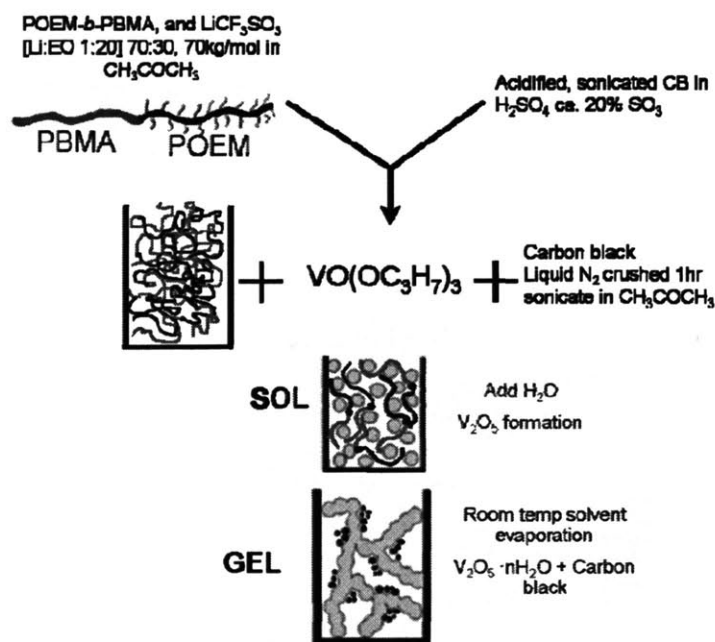


Figure 3-4: Scheme for adding carbon black to composite films

The mixture containing POEM-*b*-PBMA, VO(OⁱPr)₃, and CB was allowed to stir for 15 minutes. To catalyze the sol-gel process, deionized water was added, maintaining

the mole ratio of H₂O:V at 40:1. The solution was cast in a PTFE dish and dried under a glass Petri dish at room temperature overnight. The resulting 100 μm films were vacuum dried at 80°C overnight. The amount of precursor added to the POEM-*b*-PBMA resulted in 33 wt% of vanadium oxide in the final film, confirmed by thermogravimetric analysis (TGA). The final films made according to these methods will be referred to as POEM-*b*-PBMA/VO_x/CB films.

Conducting Polymers

EDOT monomer was added to the acetone, VO(OⁱPr)₃, POEM-*b*-PBMA solution. After the addition of water the system was cast and dried as described previously. The polymerization of the monomer proceeded chemically by the oxidative properties of V₂O₅. [5-7] A survey of the literature indicated PEDOT might serve as an exclusive conductivity additive eliminating the need for carbon black. [8] The polymerization of PEDOT from EDOT monomer added to the initial solution was verified electrochemically. Cross-sectional imaging via STEM was used to verify the presence of sulfur groups within the film to confirm VO_x/PEDOT interaction.

In addition, the deposition of PEDOT on the surface of the vanadium oxide structure was performed by electrodeposition. The deposition was performed in a three electrode cell, described in detail below in the section entitled, Electrochemical Characterization, with platinum as a counter electrode and an Ag/AgNO₃ reference electrode (in two instances a Ag wire alone was used as a reference). The electrolyte was 0.05 M TBAClO₄ in PC, mixed in the glove box and 300 μL of EDOT was added after the system had been purged with argon for 40 min. The working electrode was composite POEM-*b*-PBMA/VO_x spun coat or cast on ITO or gold coated glass slides. For the electrodes on gold-coated glass slides, a slide was placed into the PTFE dish and the solution was cast into the dish as described before. Spin coating involved dropping 100 μL of 3 wt% VO(OⁱPr)₃ in 50:50 vol IPA:acetone solution onto 2.5 cm squares of acetone and water-cleaned ITO and spinning for 30 sec at 1800 rpm. The resulting working electrode was subjected to a series of cyclic voltammetry sweeps between -0.5V – 1.6 V vs. Ag/Ag⁺ or a potential hold step to allow for deposition and electropolymerization. These results were confirmed electrochemically and compared to data found in the literature. [9-11]

Finally, PEDOT was also deposited through chemical vapor deposition (CVD) onto the composite film of POEM-*b*-PBMA/VO_x. This was done by Sung Gap Im in Prof. Karen Gleason's group of the M.I.T. Department of Chemical Engineering. An image of the CVD reactor is shown in Figure 3-5.

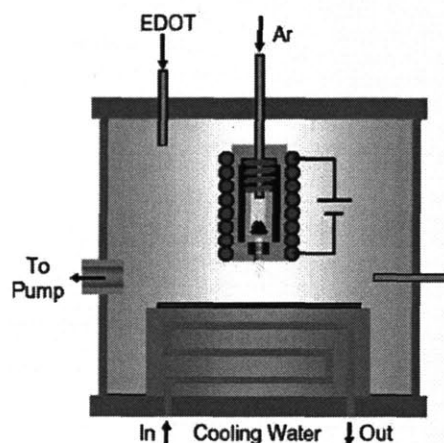


Figure 3-5: CVD reactor, Reproduced from Lock *et al.* [12]

For the deposition, the vacuum level was maintained at 150 mTorr and EDOT monomer was introduced into the reactor chamber at 3 sccm. The oxidizing agent was sublimated Fe(III)Cl₃ (Aldrich), and the process time was 30 min. After the film was formed, it was annealed under vacuum at 70°C for two hours and rinsed with water to remove excess oxidizing agent. These films were cycled galvanostatically (described below) and STEM was performed to examine the state of the PEDOT film. A control film of PEDOT was deposited on ITO to cycle with potential sweep methods to determine its capacity.

Silver Salt

Several types of silver salt were added to the films as an electronic conductivity dopant. Post-doctoral researcher, Jong Hak Kim, assisted with this strategy to enhance conductivity. Several weight percentages from 2% -10% of silver in the form of silver nitrate, AgNO₃, silver tetrafluoroborate, AgBF₄, or silver trifluoromethanesulfonate, AgCF₃SO₃ were dissolved in the water used to catalyze the sol-gel processes. The acetone, VO(OⁱPr)₃, POEM-*b*-PBMA solution was added to the silver salt solution. The

films were cast and dried as described above, except that some were cast onto aluminum foil. The reduction of silver particles was performed through thermal reduction assisted by ethylene oxide at 150°C. The reduction mechanism is discussed further in Chapter 5.

Carbon Nanotubes

Finally, additional films were made using carbon nanotubes functionalized with carboxylic acid groups. These were sonicated for an hour prior to addition to the solution of acetone, POEM-*b*-PBMA and VO(OⁱPr)₃ as before.

Electrochemical Characterization

Materials

The majority of materials used in this section have been mentioned before with the exception of 1-methyl-2-pyrrolidinone (NMP) purchased from Sigma Aldrich, polyvinylidene fluoride (PVDF) purchased from Kynar, and lithium foil purchased from VWR Scientific.

Methods

Samples were prepared in an argon-filled glove box with moisture levels below 2 ppm. Coin cells used in cycling and conductivity measurements were of the two-electrode variety consisting of stainless steel plugs as current collectors within PTFE sleeves sealed with brass lids as shown in Figure 3-6 and a schematic shown in Figure 3-7. ParaFilm was wrapped around the outside of all cells and the cells housed in plastic containers to prevent atmospheric moisture contamination.

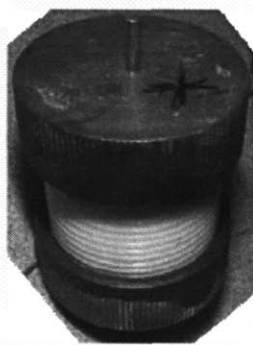


Figure 3-6: Coin cell used in battery testing

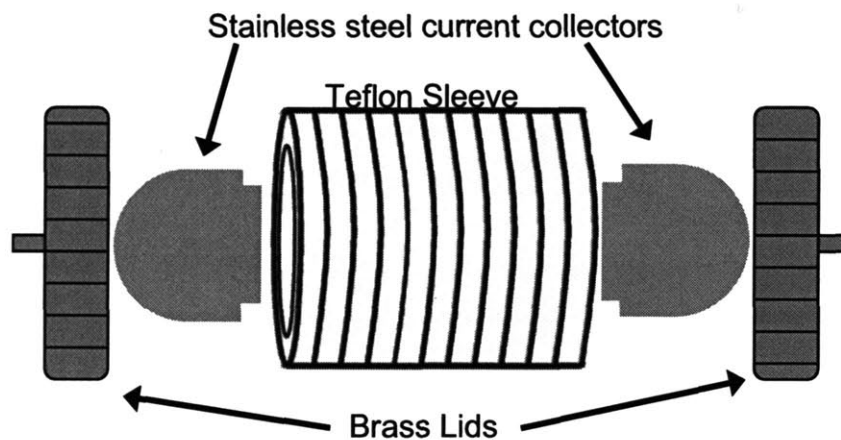


Figure 3-7: Schematic of coin cell used in battery testing

Tests were performed as indicated on either a Solartron 1286 or 1287 potentiostat (Solartron Analytical, Oak Ridge, TN) controlled by a PC running CorrWare (Scribner Associates, Inc., Southern Pines, NC) or a MACCOR 4000 Series 32 Channel system. Impedance spectroscopy was measured using a frequency response analyzer (Solartron 1255, Solartron Analytical, Oak Ridge, TN), coupled to a potentiostat (Solartron 1287, Solartron Analytical, Oak Ridge, TN) and controlled by a PC running commercially available software (Zplot, Scribner Associates, Inc., Southern Pines, NC).

Techniques

Cathode films were tested by galvanostatic cycling where constant current is forced through the cell and the cell voltage recorded. For these systems, a discharge current will cause a reduction at the cathode with the insertion of lithium into V_2O_5 which triggers a valence shift from V^{5+} to V^{4+} . Potential sweep methods such as cyclic voltammetry were used to obtain information on the faradaic processes occurring in the cathode. **Cyclic voltammetry (CV)** was conducted in a three-electrode cell, as shown in Figure 3-8, with an electrolyte of 1 M $LiClO_4$ in PC. The reference electrode (RE) was a glass tube containing a silver wire immersed in a solution of acetonitrile saturated with $AgNO_3$. A frit at the bottom of the tube enabled electrical contact with the electrolyte in the main chamber. A platinum foil served as the counter electrode (CE). The working electrode (WE) varied depending on the experiment and will be detailed more thoroughly in the specific application of the test. The potential was swept from -1.0 - 1.5 V (or as

otherwise specified) vs. Ag/Ag^+ at various sweep rates. In some instances lithium foil served as both the counter and reference electrodes. Argon was bubbled through a fourth port in the reactor (shown in figure only by bubbles).

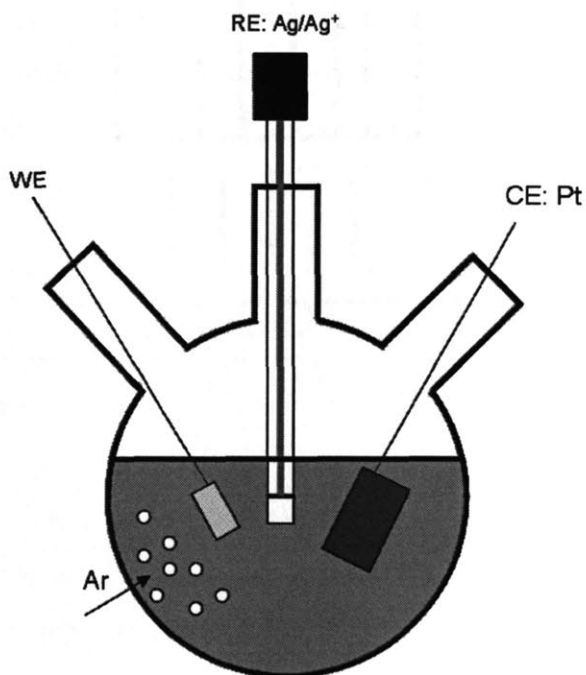


Figure 3-8: Schematic of 3-electrode cell showing WE, RE and CE. Small bubbles indicate bubbling with argon.

Impedance measurements subjected the working electrolyte to small ac perturbations in potential while recording the ac current response as well as the phase shift between the current and the voltage. The dc potential can also be controlled. The electrical behavior of a battery can be modeled by discrete circuit elements such as resistors or capacitors in series and parallel. Each element represents physical processes occurring within the cell, such as charge-transfer at an interface, or ion transport through the electrolyte.

Electrochemical Tests Performed

CV run in a three-electrode cell configuration compared the redox behavior of vanadium oxide in the nanocomposite to that of vanadium oxide alone. The working electrode was made by spin coating the vanadium oxide sol with and without POEM-*b*-PBMA onto indium tin oxide-coated (ITO) glass substrates. Solutions for spin casting

were 3 wt% VO(OⁱPr)₃ in 50:50 IPA:acetone solution containing 5 wt % polymer for those films with POEM-*b*-PBMA. Films were subsequently heated under vacuum at 80°C overnight. The reference and counter electrodes were as described above.

In addition, the conductivity of the block copolymer with and without vanadium oxide was measured. The test fixture consisted of two blocking electrodes made of stainless steel; a Teflon washer of known diameter fixed the specimen area. The thickness of the sample was measured using a micrometer before and after the conductivity measurement to verify its consistency throughout the experiment. Polymer films doped with LiCF₃SO₃ at a Li:EO ratio of 1:20 were cast from THF and dried under vacuum overnight at room temperature. For nanocomposite films, a solution of LiCF₃SO₃ in THF was added dropwise to a film of known thickness and area containing 25 wt% V₂O₅ until a ratio Li:EO of 1:20 was obtained. The film was dried overnight under vacuum at room temperature. The impedance was measured with a Solartron using the frequency range 0.1 – 1 × 10⁶ Hz as described above and the resulting Nyquist plot was fit to an equivalent circuit. The ionic conductivity of Li⁺ through the system was taken to be the real component of the impedance at the low frequency area of the curve calculated according to Equation 3-1.

$$\sigma = l/RA$$

Equation 3-1

where R is the resistance calculated from impedance measurements, L is the length of the material and A is the area.

Coin cells of several configurations were prepared in an argon-filled glove box to confirm the electrochemical behavior of the composite films. Three cells will be described in the following paragraphs and schematics of the various cell configurations assembled are shown in Figure 3-9. More specifics of each test will be given in the subsequent chapters as results are presented. (1) Cells containing POEM-*b*-PBMA/VO_x films (with and without some electronic conductivity additive as described above, termed POEM-*b*-PBMA/VO_x/+) as cathodes were made with solid polymer (POEM-*b*-PBMA) electrolyte (SPE). Polymer films (~35 μm) doped with LiCF₃SO₃ at a Li:EO ratio of 1:20 acted as the solid electrolyte and were cast from tetrahydrofuran on a 15 mm diameter lithium metal disk used as the anode. After casting the electrolyte, the film was vacuum

dried for 40 min. in the glove box side-arm to remove residual solvent. A porous polypropylene washer with an 8 mm diameter hole (Celgard 2300, Celgard, Inc., Charlotte, NC) was placed on the Li disc to prevent edge shorting and the POEM-*b*-PBMA/VO_x/+ film was placed on top. The electrodes and electrolyte stack was placed within a Teflon sleeve flanked by stainless steel current collector plugs and capped with brass lids on either end as shown in Figure 3-6 and Figure 3-7. The cell was sealed with Parafilm and placed in plastic housing.

(2) Cells were also made with POEM-*b*-PBMA/VO_x/+ films using liquid electrolyte containing 1 M LiPF₆ in ethylene carbonate (EC): dimethyl carbonate (DMC) 1:1 by mass (herein referred to as LP50) with a Celgard 2300 disk as a separator to prevent shorting.

(3) As controls, cells were prepared using conventional composite cathodes (CCC) made of sol-gel vanadium oxide, CB and PVDF as a binder, and liquid electrolyte. CCCs were made by mixing the active battery material with 10 wt% PVDF as a binder, and 5 wt% carbon black. Approximately 1 mL of NMP was added and the mixture was cast onto aluminum foil and allowed to dry in the chemical fume hood at room temperature overnight. Lower current rates were explored using the Solartron while cycle testing was conducted galvanostatically at 25°C with a MACCOR series 4000 automated test system. Voltage limits were set at 3.6 V and 2.3 V with varying discharge and charge rates.

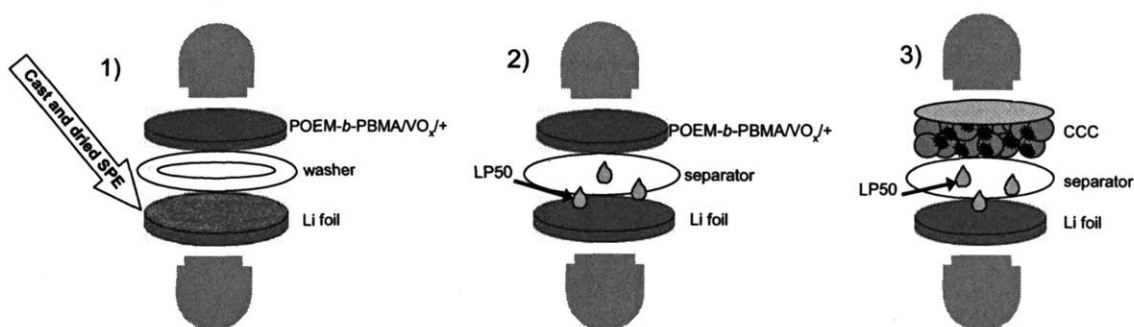


Figure 3-9: Schematics of test cells. SPE: solid polymer electrolyte, LP50: liquid electrolyte, CCC: conventional composite cathode.

Control films containing only polymer and salt with additions of vanadium oxide or carbon black were also synthesized and dried under similar conditions. These films

were cast on indium tin oxide-coated glass substrates for 3-electrode cell measurements. The redox behavior of the POEM-*b*-PBMA/VO_x/CB film was compared to the control films containing only carbon black or vanadium oxide by CV.

Characterization techniques: Ex Situ

Polymer Characterization

¹H nuclear magnetic resonance (Bruker Avance DPX-400 400 MHz NMR Spectrometer) was used to verify polymer compositions. For NMR measurements, approximately 10 milligrams of polymer were placed in a Wilmad 528 NMR tube and dissolved in deuterated chloroform.

Gel permeation chromatography (GPC) was run at 30°C on a Viscotek GPCmax instrument. The columns were calibrated with polystyrene standards.

X-ray Diffraction

Small angle x-ray scattering (SAXS) experiments were carried out on a Molecular Metrology 2D SAXS system with CuK_α radiation ($\lambda = 1.542 \text{ \AA}$) operated at 45 kV and 0.67 mA. A 600 micron x-ray beam was provided via pinhole collimation and a fine focus filament. The sample-to-detector distance was 1.3 m and silver behenate (VWR Scientific) was used as a calibration standard. Two dimensional data were radially averaged to produce $I(q)$ versus q plots, where $I(q)$ is the scattered intensity at wavevector $q = [4\pi \sin\theta]/\lambda$, and θ is the scattering angle. All data were corrected for background scattering and plotted as $\log I(q)$ vs. q to better delineate peaks.

Wide angle x-ray scattering (WAXS) experiments were carried out on a Rigaku Rotaflex 18 kW rotating anode x-ray generator with CuK_α radiation operated at 60 kV and 300 mA. The 2θ range was from 5° to 55° with a scanning speed of 1°/min and sample-to-detector distance of 185 mm. Data were also acquired in transmission mode to obtain stronger signal.

Spectroscopy

X-ray photoelectron spectroscopy (XPS) was used to verify the valence state of the vanadium oxide phase. XPS experiments were performed by graduate researcher Ayse Asatekin on a Kratos Axis Ultra (Kratos Analytical, Manchester, England) XPS

employing a monochromatic Al K_{α} source ($h\nu = 1486.7$ eV) and an electron take-off angle of 90° relative to the sample plane. A survey scan (0-1100 eV binding energy range, 160 eV pass energy) and high resolution scans of the V 2p and O 1s peaks (10 eV pass energy) were run for each sample.

Fourier transform infrared spectroscopy (FTIR) spectra were measured using Nicolet Magna 860 FTIR spectrometer; 64-64 scans were signal-averaged at a resolution 4 cm^{-1} . FTIR experiments were performed with the assistance of Dr. Jong Hak Kim. Samples were prepared by casting 10 μL of solution onto 13 mm diameter silicon substrates (2 mm thick, Sigma Aldrich) and placed under vacuum overnight to remove moisture.

Thermal Characterization

Thermogravimetric analysis (TGA) was used to determine the vanadium oxide content of nanocomposite films after solvent evaporation. TGA (Model Q50, TA Instruments, Inc.) was performed under a nitrogen atmosphere using a heating rate of $20^{\circ}\text{C}/\text{min}$ and a temperature range of 30°C to 600°C .

Differential scanning calorimetry (DSC) was performed on a DSC Q100 (TA Instruments, Inc.). Samples were sealed in Al pans and heated at a rate of $20^{\circ}\text{C}/\text{min}$ in a flowing atmosphere of nitrogen (50 mL/min). The temperature range for DSC measurements was -100°C to 90°C and the data were taken upon heating.

Rheology

The dynamic mechanical properties of the nanocomposite films were probed using a strain-controlled rheometer (ARES, Rheometrics). The rheometer was operated in the parallel-plate oscillatory shear mode with a 1 mm gap at 30°C . The sample was molded on the 25 mm diameter test fixture by pressing a film of the material to the measurement gap width. The frequency dependence of the dynamic storage and loss moduli (G' and G'' , respectively) were recorded for the frequency range from 200 to 0.1 rad/s at a relatively small strain amplitude of 1.5%. Dr. Jong Hak Kim performed these experiments.

Electron Microscopy

Microstructural characterization of the nanocomposite films was carried out using transmission electron microscopy (TEM JEOL 2010 CX) in bright field mode at 200 keV. This microscope uses electron emission from a LaB₆ filament under high vacuum accelerated through a magnetic field. Samples for TEM were prepared by cryomicrotoming ~50 nm sections using a diamond knife (Diatome), placing the sections on copper grids (400 mesh, Ted Pella) and coating them with ~15 nm of carbon through thermal evaporation. Some polymer samples with and without vanadium oxide were stained with ruthenium tetroxide, RuO₄, for image contrast. For staining purposes, grids were placed onto a glass slide and loaded into a chamber containing RuO₄ vapor freshly added from ampoules (EMS Acquisition Corp.), where they were exposed for 30 min. For powder samples, dispersions were placed on carbon-coated copper grids (Ernest Fullam).

Scanning transmission electron microscopy (STEM, VGHB603) was performed on the same samples for chemical mapping within the films with the assistance of Tony Garrett-Reed in the Center for Materials Science and Engineering shared microscopy facility. Chemical analysis was performed using an Oxford EDX detector and Inca Vision software for elemental analysis.

Scanning electron microscopy (SEM) was performed on the films. The samples were coated with Au/Pd and mounted with carbon tape onto aluminum posts. The microscopy was performed on a JEOL 6320FV Field-Emission high-resolution SEM at 1 kV.

Surface Area

The surface area of the samples was determined using the Brunauer, Emmet and Teller (BET) technique on a Micrometrics ASAP2020 instrument. Prior to the measurement, the samples underwent degassing for 2 hours under flowing nitrogen at 100°C.

The next chapters will describe the results of the *in situ* growth of vanadium oxide within the domains of block and graft copolymers and attempts to cycle these films as cathodes in lithium rechargeable batteries.

References

1. Trapa, P. E., Huang, B., Won, Y.-Y., Sadoway, D. R. & Mayes, A. M. "Block Copolymer Electrolytes Synthesized by Atom Transfer Radical Polymerization for Solid-State, Thin-Film Batteries." *Electrochemical and Solid-State Letters*, **2002**, 5, A85-A88.
2. Trapa, P. E. et al. "Rubbery Graft Copolymer Electrolytes for Solid-State, Thin-film Lithium Batteries." *Journal of the Electrochemical Society*, **2005**, 152, A1-A5.
3. Tang, P., Sakamoto, J. S., Baudrin, E. & Dunn, B. "V₂O₅ aerogel as a versatile host for metal ions." *Journal of Non-crystalline Solids*, **2004**, 350, 67-72.
4. Huang, H. & Nazar, L. F. "Grafted Metal Oxide/Polymer/Carbon Nanostructures Exhibiting Fast Transport Properties." *Angewandte Chemie Intern. Ed.*, **2001**, 40, 3880-3884.
5. Murugan, A. V., Kale, B. B., Kwon, C.-W., Campet, G. & Vijayamohanan, K. "Synthesis and characterization of a new organo-inorganic poly(3,4-ethylene dioxythiophene) PEDOT/V₂O₅ nanocomposite by intercalation." *Journal of Materials Chemistry*, **2001**, 11, 2470-2475.
6. Kuwabata, S., Masui, S. & Yoneyama, H. "Charge-discharge properties of composites of LiMn₂O₄ and polypyrrole as positive electrode materials for 4V class of rechargeable Li batteries." *Electrochimica Acta*, **1999**, 44, 4593-4600.
7. Huguenin, F., Giroto, E., Torresi, R. M. & Buttry, D. A. "Transport properties Of V₂O₅/polypyrrole nanocomposite prepared by a sol-gel alkoxide route." *Journal of Electroanalytical Chemistry*, **2002**, 536, 37-45.
8. Arbizzani, C., Mastragostino, M. & Rossi, M. "Preparation and Electrochemical Characterization of a polymer Li_{1.01}Mn_{1.97}O₄/pEDOT Composite Electrode." *Electrochemistry Communications*, **2002**, 4, 545-549.
9. Du, X. & Wang, Z. "Effects of polymerization potential on the properties of electrosynthesized PEDOT films." *Electrochimica Acta*, **2003**, 48, 1713-1717.

10. Chang, C.-C., Her, L.-J. & Hong, J.-L. "Copolymer from electropolymerization of thiophene and 3,4-ethylenedioxythiophene and its use as cathode for lithium ion battery." *Electrochimica Acta*, **2005**, 50, 4461-4468.
11. Lapkowski, M. & Pron, A. "Electrochemical oxidation of poly(3,4-ethylenedioxythiophene)- "in situ" conductivity and spectroscopic investigations." *Synthetic Metals*, **2000**, 110, 79-83.
12. Lock, J. P., Im, S. G. & Gleason, K. K. "Oxidative Chemical Vapor Deposition of Electrically Conducting Poly(3,4-ethylenedioxythiophene) Films." *Macromolecules*, **2006**, 39, 5326-5329.

Chapter 4 : Structure-Directed Vanadium Oxide

In this thesis continuous, nanoscale composites were synthesized using the microphase-separation of block and graft copolymers as matrices to structure-direct the growth of active inorganic compounds, towards use as cathodes for lithium rechargeable batteries. This chapter will describe the growth of sol-gel derived vanadium oxide within the hydrophilic domain of block and graft copolymers. This approach makes use of the amphiphilic nature of copolymers to dictate vanadium oxide nanostructures. The chapter begins with the characterization of the block and graft copolymers used in this research. The synthesis of polymer/inorganic composites is subsequently described, followed by the characterization of the composites both chemically and electrochemically.

Questions this chapter will address:

1. Can microphase-separated polymers be used to direct the growth of cathode active materials, such as transition metal oxides?
2. Are the resulting microstructures continuous and on an appropriate size scale?

Polymer Matrix

The final POEM-*b*-PBMA block copolymer used in this work, whose synthesis is described in the previous chapter, had a molecular weight of 70 kg/mol and polydispersity index of 1.26, based on gel permeation chromatography (previously calibrated with polystyrene standards). Unless otherwise stated, the final composition of the polymer used for the matrix was 70 wt% POEM and 30 wt% PBMA. The strategy of incorporating an inorganic active battery phase into a copolymer system relied on the microphase separation of the polymer into regions of hydrophilic, ion-conducting POEM domains and mechanically stabilizing domains of PBMA. The majority of the polymer was POEM, so that this block was able to form a continuous network for ion conduction and for ion insertion into the vanadium oxide phase. A SAXS and TEM study of the pristine 70:30 POEM-*b*-PBMA found it to be microphase separated, with a domain periodicity, d , of ~35 nm. The SAXS pattern for POEM-*b*-PBMA is shown in Figure 4-1

(a) and indicates the structure had a cylindrical morphology owing to the ratio of q between the first scattering peak and the second peak (factor of $3^{1/2}$ for second peak relative to main peak for hexagonally-packed cylinders).[1]

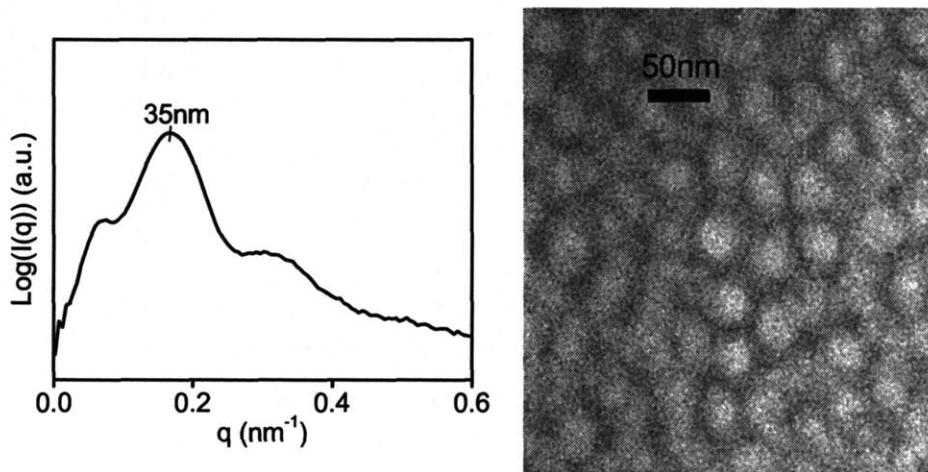


Figure 4-1: Characterization of pristine POEM-*b*-PBMA: (a) SAXS pattern from pristine POEM-*b*-PBMA (b) TEM micrograph of POEM-*b*-PBMA (70:30) stained with RuO_4 (preferentially stains POEM domains, therefore, dark above).

The peak/shoulder visible at $q \sim 0.076 \text{ nm}^{-1}$ is attributed to the beamstop of the instrument, and was deconvolved from the primary reflection in performing peak fitting of the scattering maximum in this and future measurements.

The TEM micrograph for POEM-*b*-PBMA in Figure 4-1 (b) depicts the cylindrical morphology indicated by the SAXS pattern for the neat polymer. The stain, RuO_4 , gives contrast between the phases because it is preferential to the POEM domain. Therefore, in Figure 4-1(b), the POEM domain is dark and the PBMA is light. The 50 nm scale bar shown in the image verifies the domain spacing of the polymer. The DSC trace of POEM-*b*-PBMA, shown in Figure 4-2, indicates two distinct glass transition temperatures (T_g s), further evidence of microphase separation. The first T_g of -69°C for the POEM domain is very distinct and consistent with that reported for PEO; the second T_g of 30°C for PBMA is also consistent with reported values for PBMA homopolymer.[2]

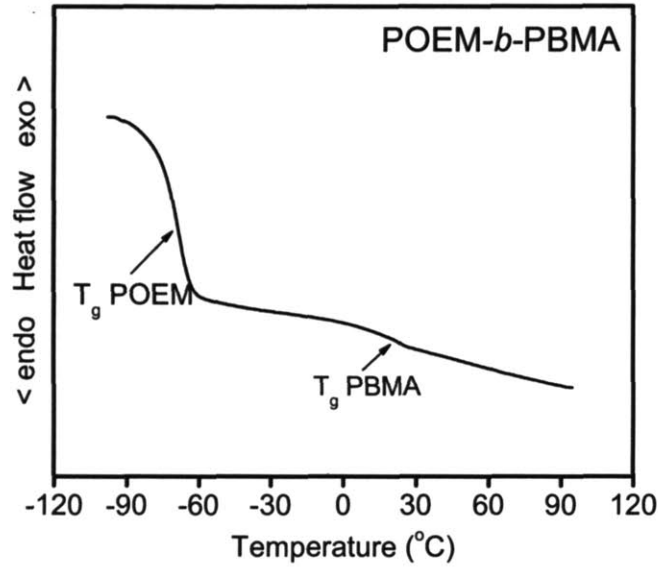


Figure 4-2: DSC trace for POEM-*b*-PBMA.

The final POEM-*g*-PDMS polymer had a composition of 70:30 with a molecular weight of 80 kg/mol and a polydispersity index of 1.7. The SAXS for the pristine polymer is shown below in Figure 4-3 and indicates a *d* spacing of 17 nm. This spacing is substantially smaller than that of the POEM-*b*-PBMA system used. In the SAXS pattern, no higher order peaks are evident, consistent with the random graft structure expected from the free radical synthesis route employed. The TEM image in Figure 4-3 shows the nanodomain morphology to be highly defected.

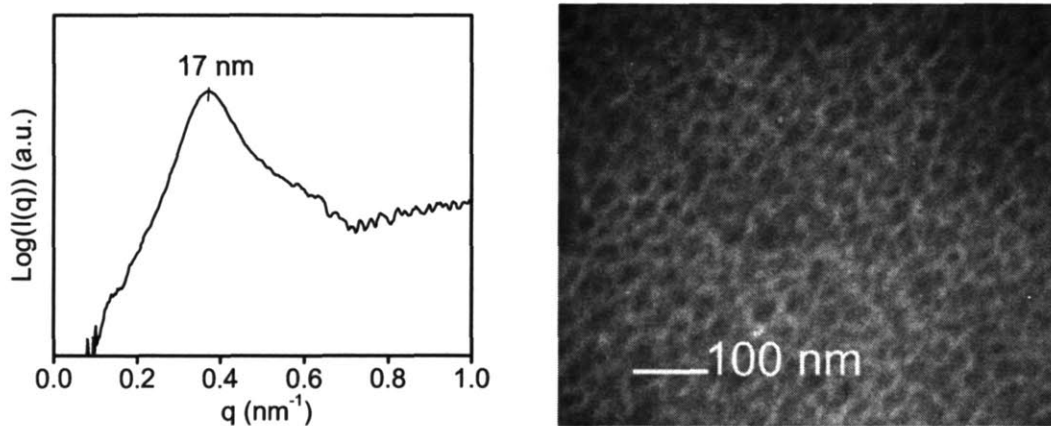


Figure 4-3: Characterization of pristine POEM-*g*-PDMS: (left) SAXS pattern from pristine POEM-*g*-PDMS (right) TEM micrograph of unstained POEM-*g*-PDMS (70:30).

For the POEM-*g*-PDMS micrograph, the sample was not stained and the image contrast results from differences in electron density and beam thinning rates of the PDMS and POEM domains. PDMS appears as the darker phase.

DSC results for this material are shown in Figure 4-4. This trace indicates two T_g values, one at -69°C and one at -130°C , further confirming the microphase separation of POEM and PDMS components of this graft copolymer.

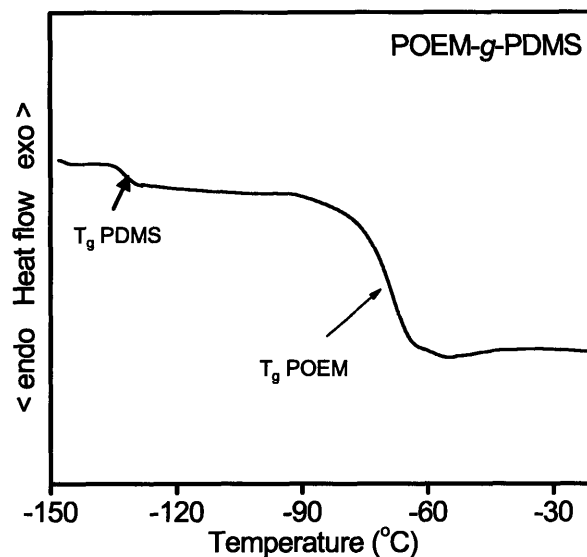


Figure 4-4: DSC trace for POEM-*g*-PDMS.

The ionic conductivities of both the graft and block copolymers have been investigated previously by Trapa *et al.*[2, 3] Here the room temperature conductivities were verified for the polymers synthesized to confirm these results and for comparison with the composite structures. The ionic conduction properties of these polymers are described here as background information. The change in POEM-*b*-PBMA conductivity as a function of temperature is shown in Figure 4-5. Each polymer shown is doped with LiCF_3SO_3 to a Li:[EO] ratio of 1:20.

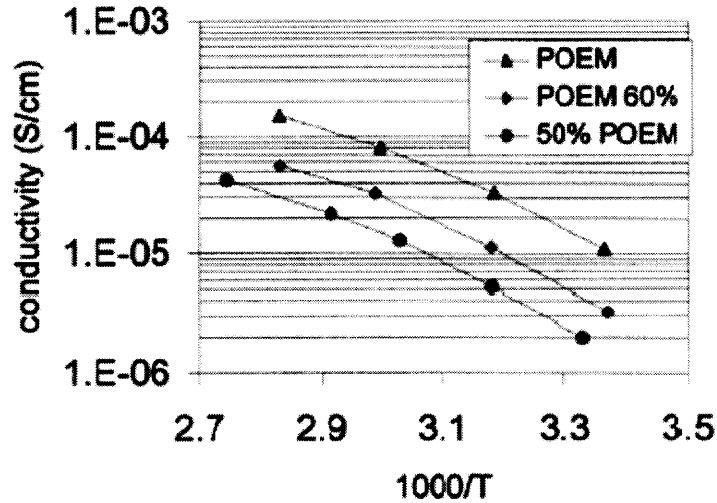


Figure 4-5: Ionic conductivities measured by EIS for POEM and POEM-*b*-PBMA. Reproduced from Trapa *et al.* [2]

The values are shown to be within an order of magnitude as POEM homopolymer and follow the expected Vogel-Tamman-Fulcher relationship with temperature.[4, 5] The graft copolymer system shows similar temperature dependence depicted in Figure 4-6. However, this system has a higher overall ionic conductivity and matches closely that of the conductivity of POEM homopolymer. It has been demonstrated that the conductivity of POEM-based block copolymer electrolytes scales inversely with the T_g of the non-conducting block.[6] Because the glass transition temperature of PBMA is around room temperature, this component has reduced mobility compared to PDMS, causing the block copolymer conductivity to be lower.

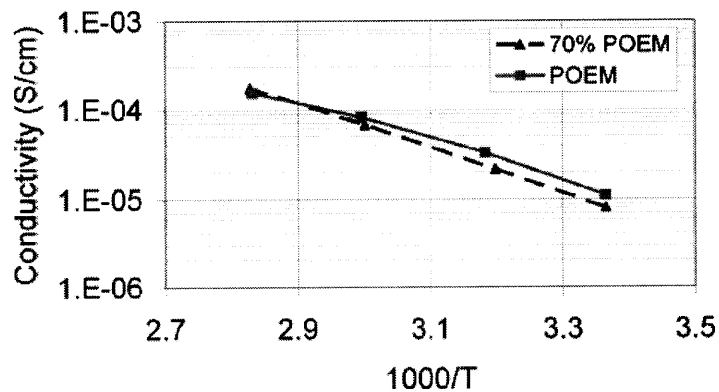


Figure 4-6: Ionic conductivities measured by EIS of POEM and POEM-*g*-PDMS. Reproduced from Trapa *et al.* [3]

Inorganic Characterization: POEM-*b*-PBMA/VO_x

Structure and Chemical Characterization

Several characterization techniques were used to confirm the preservation of microphase separation in the polymers after the addition of vanadium oxide. Solution cast films of POEM-*b*-PBMA incorporating the product vanadium oxide from *in situ* sol-gel synthesis were semi-transparent and flexible for vanadium oxide precursor contents < 60 wt%. Figure 4-7 shows a film sample prepared from a 30 wt% VO(OⁱPr)₃ precursor solution. The semi-transparent nature of the film suggests the absence of macrophase separation of the organic and inorganic phases, and provides a first indication that the vanadium oxide is confined to the POEM domain of the microphase-separated block copolymer.

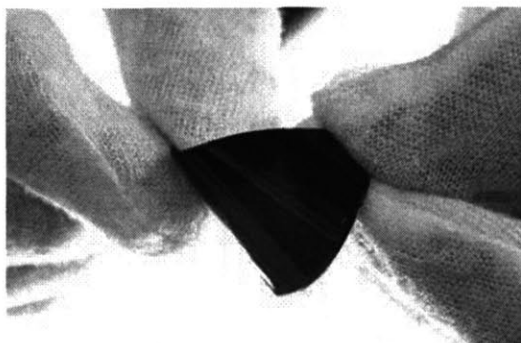


Figure 4-7: POEM-*b*-PBMA film incorporating 18 wt% VO_x (from 30 wt% precursor) grown *in situ* by sol-gel chemistry.

As shown in Figure 4-8, the weight fraction of the vanadium oxide inorganic phase incorporated into the polymer, as determined by TGA, varied linearly with precursor concentration in the casting solution. Figure 4-8 (a) shows the TGA traces for different concentrations of precursor additions and Figure 4-8 (b) shows the consistent linear relation between the amount of precursor added and the amount of vanadium oxide ending up in the final film. The slope of this line was 0.62, indicating approximately 60% conversion between precursor and final inorganic. It is hypothesized that the reduced yield was caused by evaporation of the precursor solution, which has a boiling point of 60°C.

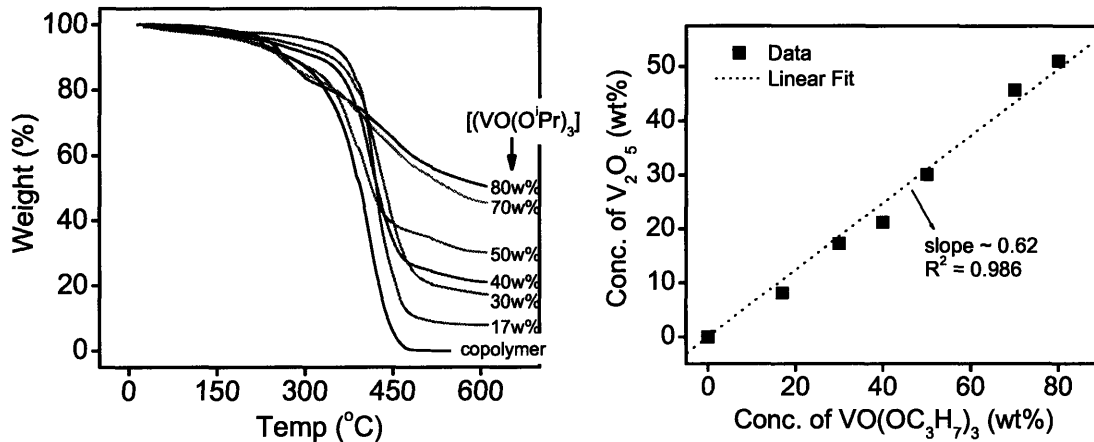


Figure 4-8: Weight% of VO_x determined from TGA as a function of precursor concentration for nanocomposite films. Linear fit of these data shown on the left.

Further evidence for nanodomain confinement of the oxide is given in SAXS patterns taken on POEM-*b*-PBMA incorporating increasing weight fractions of vanadium oxide, as seen in Figure 4-9 (data are offset for clarity). The trace for pristine POEM-*b*-PBMA is included for comparison.

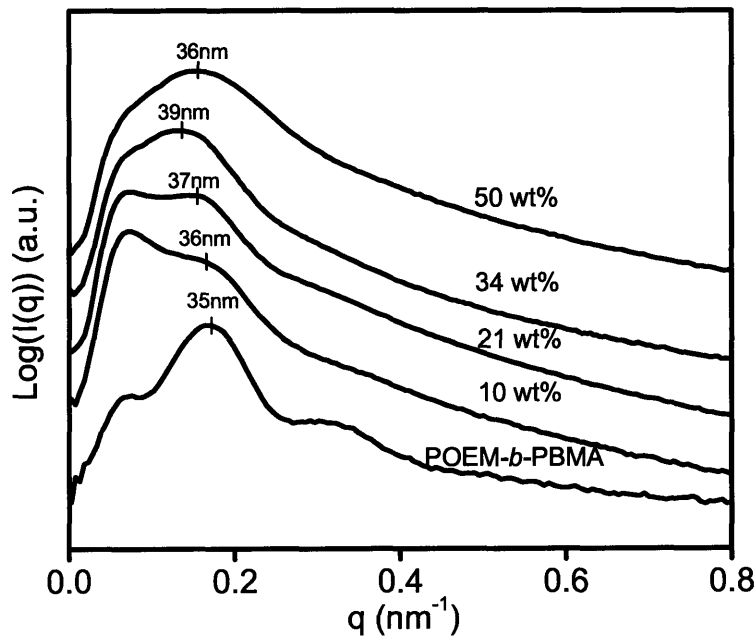


Figure 4-9: SAXS patterns for neat POEM-*b*-PBMA copolymer and nanocomposite films with vanadium oxide weight % as indicated (data are offset for clarity).

The peak/shoulder, still visible for some of the traces at $q \sim 0.076 \text{ nm}^{-1}$, is attributed to the beamstop of the instrument, and was deconvolved from the primary reflection in performing peak fitting of the scattering maximum. The shift to lower q values of the observed maximum in SAXS patterns from nanocomposite films indicates an increase in the periodicity as vanadium oxide content increases. For an oxide fraction of 34 wt%, d increases by 11% over that of the neat copolymer. Additionally, the second order reflection observed for the neat polymer was absent for nanocomposite films, suggesting a change in morphology and/or loss of long range order. At higher inorganic loadings, the peak of the SAXS trace shifts back towards higher q (lower d), suggesting partial macrophase separation of the oxide phase.

Figure 4-10 shows TEM micrographs of the POEM-*b*-PBMA matrix nanocomposite film incorporating 24 wt% vanadium oxide (a), and a film incorporating 50 wt% vanadium oxide (b).

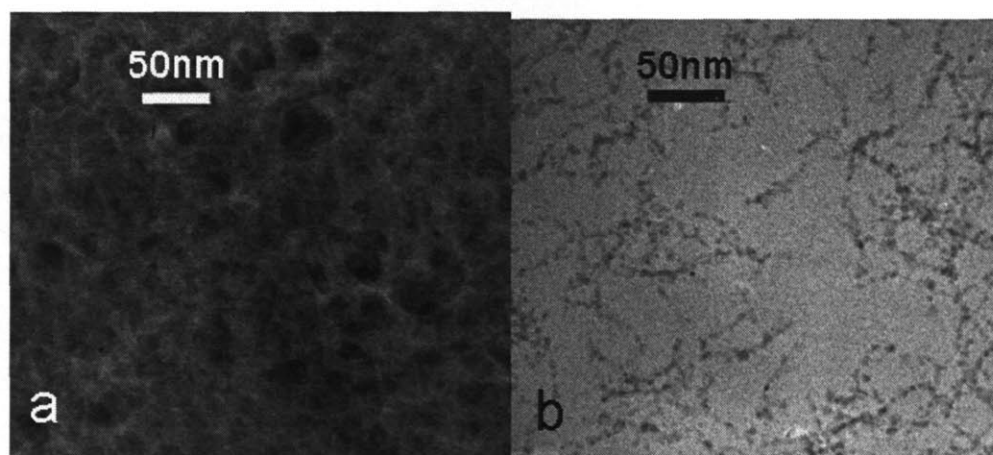


Figure 4-10: TEM micrographs of a) POEM-*b*-PBMA containing 24 wt% V_2O_5 (dark field: light regions are V_2O_5); b) POEM-*b*-PBMA containing 50 wt% V_2O_5 (bright field: dark regions are V_2O_5).

Unlike Figure 4-1 above indicating the neat POEM-*b*-PBMA, Figure 4-10 (a) and (b) are unstained, so that POEM and PBMA would be indistinguishable, but for the vanadium oxide, which offers the contrast present in the micrograph. $\text{VO}(\text{O}^i\text{Pr})_3$ and its hydrolysis products are expected to be preferentially incorporated into the POEM block as a result of POEM's hydrophilic polyethylene oxide (PEO) side chains and ability for hydrogen bonding.[7] Figure 4-10 (a), shown in dark field mode to provide better

contrast, is representative of films containing 10-34 wt% inorganic phase. The vanadium oxide phase (light region) is seen to form a filamentous network, akin to the ribbon-like morphologies reported in the literature for sol-gel synthesized V_2O_5 . [8] Regions devoid of vanadium oxide (dark areas) are visible on the same size scale as the PBMA domains of the neat polymer. However, the structure of the voids is inconsistent with that of cylinder microdomains, indicating a change in morphology with the addition of vanadium oxide as noted from SAXS patterns. Transformation to spherical PBMA domains due to the increase in effective volume of POEM domains might be expected; alternatively, a bicontinuous network could yield a similar oxide microstructure to that seen in Figure 4-10 (a). At still higher oxide contents, macrophase separation was observed, consistent with SAXS results. In Figure 4-10 (b), taken from a sample containing 50 wt% inorganic phase, large regions devoid of vanadium oxide are evidence of macrophase separation between the inorganic phase and the copolymer.

Verification of vanadium oxide confinement to the POEM domains for lower oxide contents was obtained by chemically mapping ruthenium and vanadium in a RuO_4 stained sample using scanning TEM (STEM) of POEM-*b*-PBMA with 24 wt% V_2O_5 . Figure 4-11(a) shows the bright field image of a RuO_4 -stained film incorporating 24 wt% vanadium oxide. Figure 4-11 (b) and (c) display the distribution of ruthenium and vanadium, respectively. The strong similarities in the spatial distribution patterns of these two figures confirm the co-location of vanadium oxide and POEM. These micrographs also appear more consistent with interconnected PBMA domains than isolated PBMA spheres.

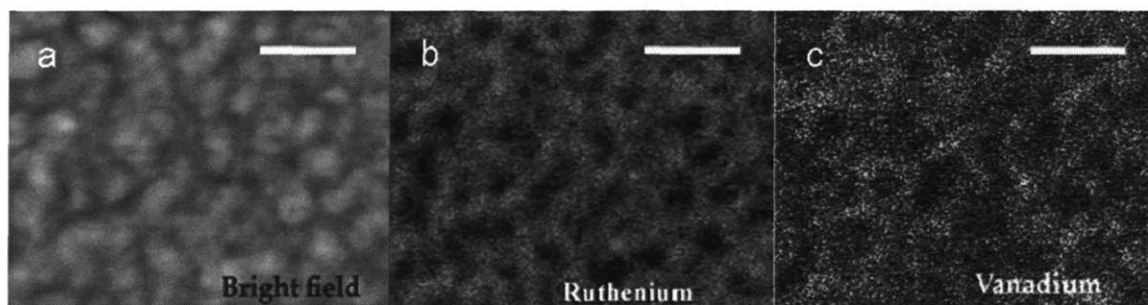


Figure 4-11: STEM micrographs of POEM-*b*-PBMA containing 24 wt% vanadium oxide: a) bright field stained with RuO_4 ; b) ruthenium chemical map; c) vanadium chemical map (scale bar = 50 nm).

DSC measurements in Figure 4-12 provided further evidence for the confinement of vanadium oxide to the POEM domains.

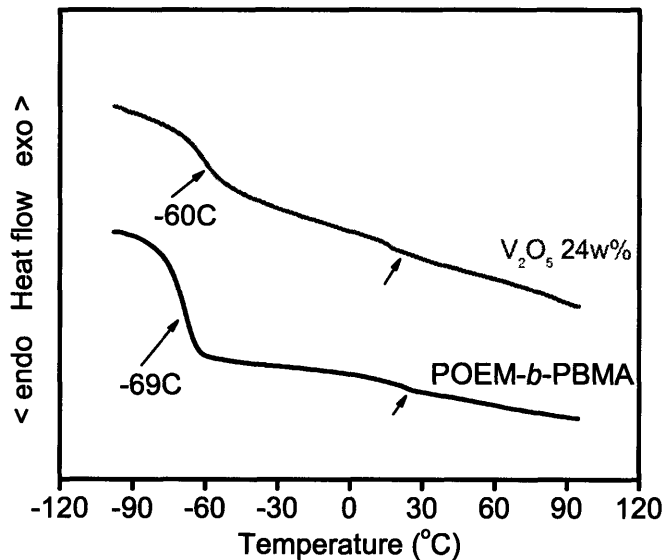


Figure 4-12: DSC trace of pristine polymer and after incorporation of vanadium oxide.

DSC traces from the nanocomposites show that the T_g of the PBMA domains remains constant at 30°C, while the T_g of the POEM domain increases with the addition of the vanadium oxide. The POEM T_g is observed to shift from -69°C for the neat copolymer to -60°C for 24 wt% oxide incorporation. This can be explained by the interaction of the vanadium oxide with the ether oxygen groups of POEM, which serves to reduce the chain mobility.

The material was examined by FTIR to verify the interaction of VO_x with the POEM domain. The absorbance spectra for pristine POEM-*b*-PBMA and that of a film containing 24 wt% VO_x is shown in Figure 4-13. Several bands appear upon the addition of the inorganic phase. The characteristic V_2O_5 bands corresponding to V-O-V at 760 cm^{-1} and V=O at 999 cm^{-1} appear in the 24 wt% film. The broad band between 1050 and 1220 cm^{-1} is attributed to the C-O-C stretching group and the diminishing of the ether oxygen around 1150 cm^{-1} in the composite film corresponds to electron donation to compensate for the presence of vanadium oxide.[9]

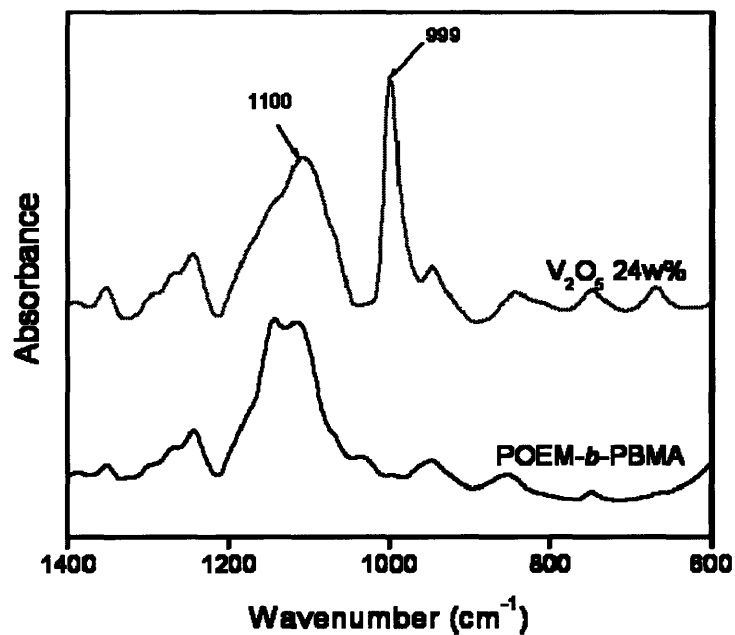
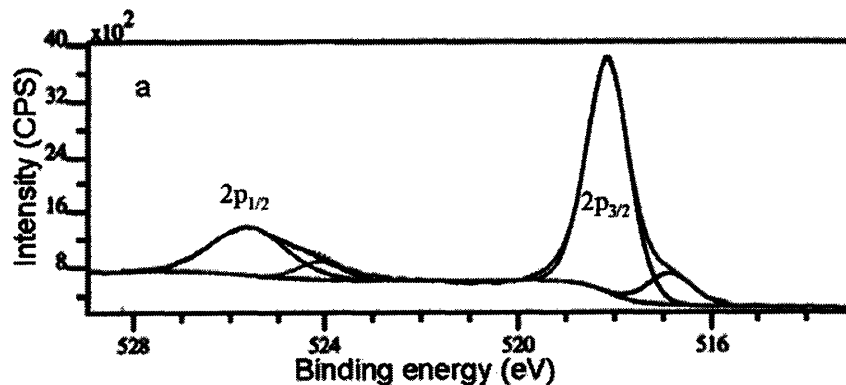


Figure 4-13: FTIR spectra for neat POEM-*b*-PBMA (black, lower) and POEM-*b*-PBMA/V₂O₅ (red, upper).

Characterization of phases

The formation of amorphous V₂O₅ through the sol-gel process was verified by XPS (Figure 4-14) and WAXS (Figure 4-15). Figure 4-14 shows the XPS V 2p high resolution spectrum for sol-gel synthesized vanadium oxide in the absence of the copolymer (a), along with that from a nanocomposite sample prepared by *in situ* hydrolysis (b). The results are presented after Shirley background subtraction.



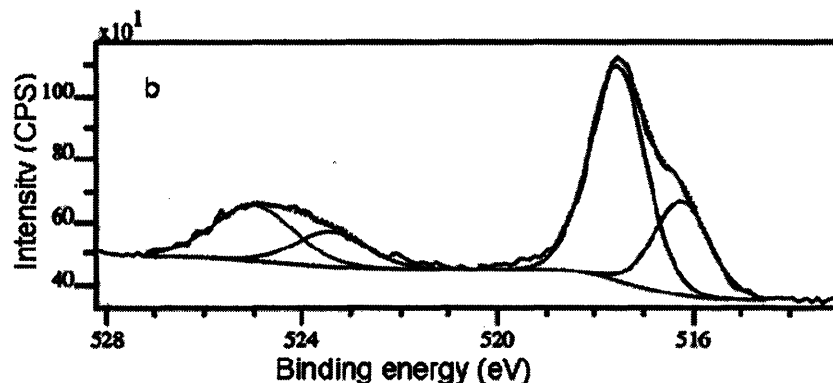


Figure 4-14: XPS high-resolution spectra of V 2p peak for a) neat vanadium oxide prepared by sol-gel synthesis and b) vanadium oxide grown within block copolymer.

The V 2p peaks at 518 eV ($2p_{3/2}$) and 525.5 eV ($2p_{1/2}$) due to V^{5+} observed in the pure vanadium oxide sample (Figure 4-14a) strongly resemble the spectrum for V_2O_5 previously published.[10] The nanocomposite film also shows these peaks in the high resolution 2p spectrum (Figure 4-14b). In addition, both spectra exhibit shoulders at lower binding energies characteristic of the V^{4+} state, consistent with the color change observed in the film preparation. From the relative intensities of the V^{4+} and V^{5+} contributions, ~88% and 70% of the vanadium is in a 5^+ state for the neat oxide and nanocomposite, respectively. From the low resolution XPS spectra, the V:O mole ratio for the neat oxide was 3.1:1, indicating 80% V_2O_5 stoichiometry. The larger V^{4+} content for the nanocomposite samples may be due to incomplete hydrolysis of the vanadium oxide or participation of the polymer in the gelation and condensation process.

WAXS data contained in Figure 4-15 depict patterns from neat POEM-*b*-PBMA, neat V_2O_5 , and a nanocomposite film incorporating 24 wt% V_2O_5 .

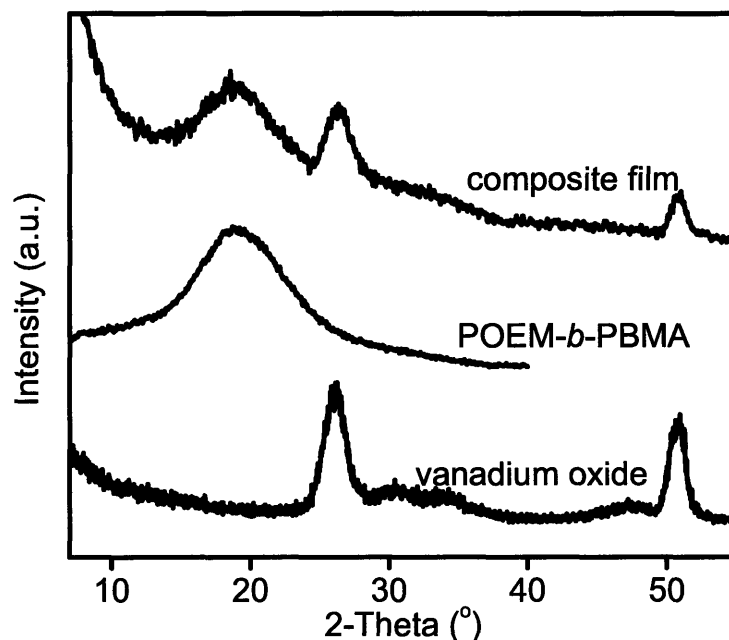


Figure 4-15: WAXS patterns for neat POEM-*b*-PBMA (70:30), neat amorphous vanadium oxide from sol-gel process and nanocomposite film.

The WAXS data reveal the V_2O_5 to be amorphous, with short range order peaks at 26° and 51° , in agreement with values reported in the literature.[11] The WAXS pattern for POEM-*b*-PBMA exhibits a dominant short range order peak at $\sim 18^\circ$ corresponding to the van der Waal's distance between non-bonded atoms (C-C and C-O).[12] The XRD pattern of the composite film is a direct superposition of the patterns from its components.

The combined XPS, WAXS and DSC data indicate only slight modification to the oxide and polymer as a consequence of co-assembly.

Electrochemical Characterization

It was found that both the redox activity of V_2O_5 and the ionic conductivity of POEM, properties essential to this material's use in battery electrodes, were preserved in the nanocomposite films. The cyclic voltammograms (CVs) for the vanadium oxide film with and without POEM-*b*-PBMA are shown in Figure 4-16 (a) and (b), respectively.

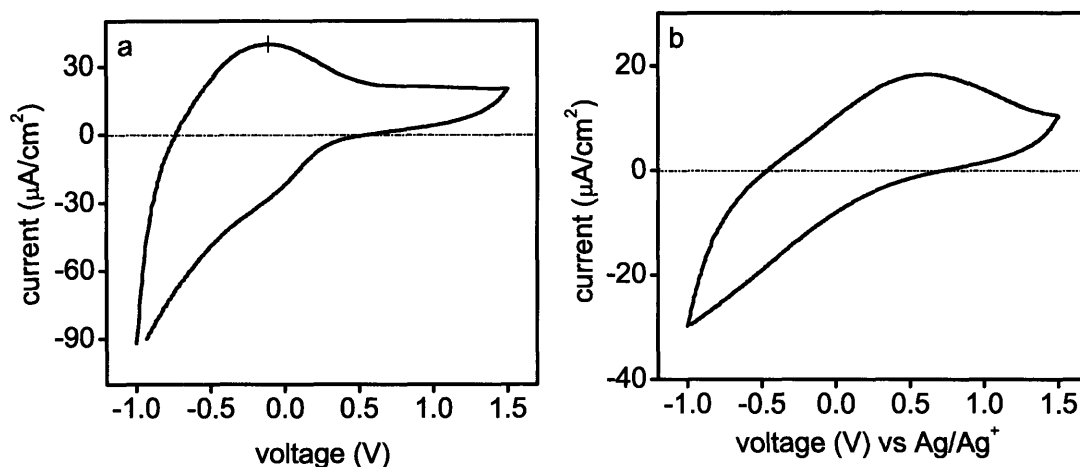


Figure 4-16: CV for a) VO_x and b) POEM-*b*-PBMA/VO_x spun coat films in LiClO₄/PC electrolyte. Swept from -1.0V – 1.5V at 50 mV/s vs. Ag/Ag⁺.

The vanadium oxide film alone is characterized by one set of redox peaks reflecting intercalation/de-intercalation of Li⁺ into/from the V₂O₅ structure. The mixed oxide/polymer electrode exhibited the same peaks, although somewhat broadened and separated by a slightly larger potential, owing to the increased resistance of the polymer matrix as compared to that of the liquid electrolyte alone. Still, the peaks in the voltammogram of the nanocomposite film are the electrical signature of lithiation and delithiation of the vanadium oxide. In the absence of Li⁺ (not shown), these peaks were entirely absent.

The electrical conductivity of POEM-*b*-PBMA films with and without vanadium oxide was measured by impedance spectroscopy. As indicated in Chapter 3, conductivity was measured through a film of known area and thickness using stainless steel blocking electrodes. A washer of known diameter and height fixed the area and thickness. The impedance spectrum of a film of polymer doped with LiCF₃SO₃ is shown below. Taking the geometric factors into account, the conductivity, σ , is calculated by Equation 3-1. The value of the electrical conductivity of POEM-*b*-PBMA doped with LiCF₃SO₃ at an Li:EO ratio of 1:20 was measured to be 3×10^{-6} S/cm at room temperature, which agrees with previous characterizations of this material as a solid electrolyte.[2] When the identical polymer was loaded with vanadium oxide to a level of 25 wt% and doped with LiCF₃SO₃ (Li:EO ratio 1:20), the maximum room-temperature conductivity was determined to be 1.8×10^{-6} S/cm. The slightly lower value of the conductivity of the composite film

compared to that of the neat polymer electrolyte can be attributed to the lower conductivity of V_2O_5 . In addition, interaction between the oxide and POEM, as evidenced by the increase in T_g , retards segmental motion in the polymer.

Inorganic Characterization: POEM-g-PDMS/ VO_x

The POEM-g-PDMS copolymer was also investigated for structure-directing capabilities. It was found that this system could also retain microphase separation with incorporation of vanadium oxide. The characteristics of this system will be described in the following section to illustrate the application of this sol-gel technique to another polymer system. Despite the higher ionic conductivity of the POEM-g-PDMS (8×10^{-6} vs. 3×10^{-6} S/cm at room temperature for POEM-g-PDMS vs. POEM-*b*-PBMA), the majority of investigations were done on the POEM-*b*-PBMA system because of the superior mechanical properties of this system.

Microphase-separated morphologies of the nanocomposites were investigated by SAXS. Figure 4-17 shows the SAXS spectra for nanocomposite films consisting of POEM-g-PDMS and vanadium oxide with various compositions.

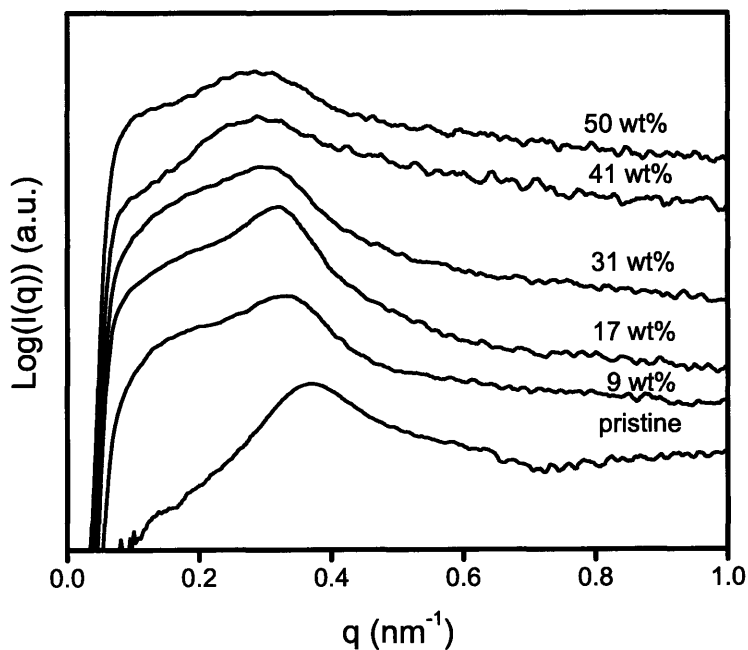


Figure 4-17: SAXS spectra for pristine POEM-g-PDMS (70:30) and its nanocomposite films with various concentration of vanadium oxide.

The SAXS pattern of the pristine system is shown again for comparison. Upon addition of vanadium oxide, the nanocomposite films retain the peak indicating microphase-separation, but as in the POEM-*b*-PBMA case, the d spacing increases up to 31 wt% vanadium oxide. However, a similar maximum in loading capacity is observed for this system at 41 wt% incorporation. The domain spacings of the films increase monotonically from 17.2 to 21.0 nm with the increase of vanadium oxide up to 31 wt%, representing the spatially-selective incorporation of vanadium oxide in POEM domains.

To investigate the formation of vanadium oxide in POEM-*g*-PDMS, WAXS spectra were measured for pristine copolymer and nanocomposite films. Pristine POEM-*g*-PDMS (70:30) show three amorphous peaks at around 8.4° , 11.9° and 20.0° (Figure 4-18). WAXS measurements of homopolymers, i.e. PDMS and POEM, clearly reveal that the peaks at 11.9° (d -spacing = 7.4 \AA) and 20.0° (4.4 \AA) originate from the interchain distances of PDMS and POEM, respectively.

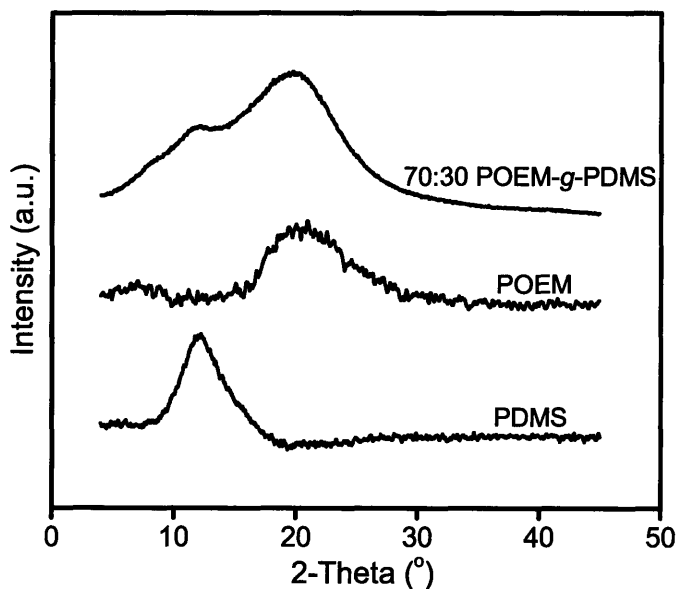


Figure 4-18: WAXS spectra for pristine POEM-*g*-PDMS (70:30) and homopolymer (POEM and PDMS).

The WAXS spectra for nanocomposite films with various concentrations of vanadium oxide are provided in Figure 4-19. As the concentration of vanadium oxide

increases, two peaks at 8.8° and 26.1° , assignable to amorphous vanadium oxide, increase, indicating the *in situ* formation of vanadium oxide in the graft copolymer.

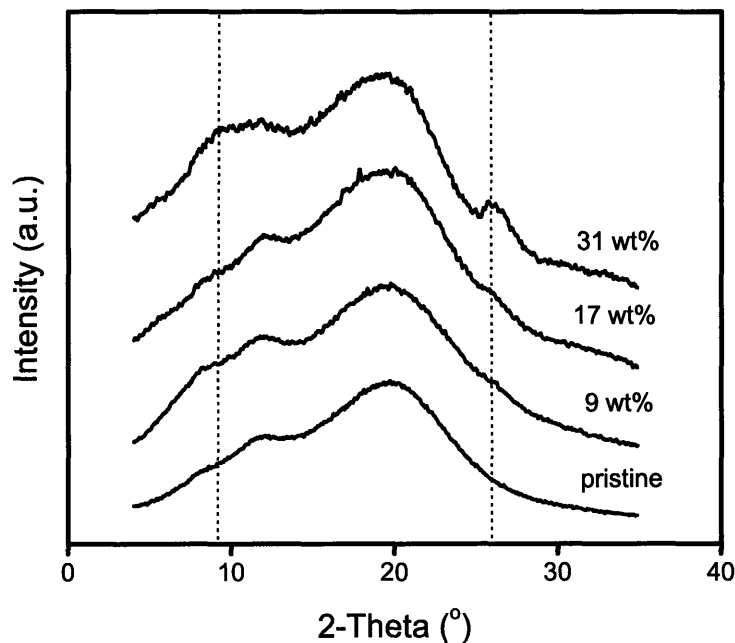


Figure 4-19: WAXS spectra for pristine POEM-*g*-PDMS (70:30) and its nanocomposite films with various concentration of vanadium oxide.

The DSC heating curves of the pristine POEM-*g*-PDMS and its nanocomposites with vanadium oxide are presented in Figure 4-20. The pristine graft copolymer is shown again for comparison. Upon the incorporation of vanadium oxide, the T_g of PDMS remains almost invariant whereas that of POEM increases, due to the interaction of vanadium oxide with the ethylene oxide moiety of POEM domains, restricting chain mobility. The value of T_g increases monotonically with increasing concentration of vanadium oxide up to 31 wt%, above which it slightly decreases. This T_g behavior is consistent with the result of SAXS, demonstrating that the maximum loading of vanadium oxide is between 31 and 41 wt%.

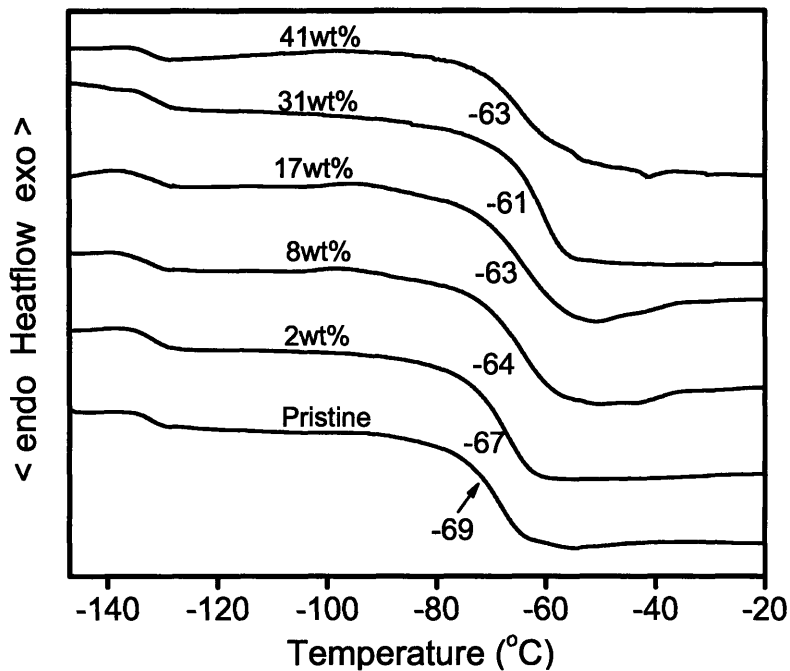


Figure 4-20: DSC curves for pristine POEM-g-PDMS (70:30) and its nanocomposite films with various concentrations of vanadium oxide.

FTIR was used to further demonstrate the interaction of the vanadium oxide with the POEM domain. The spectra for the composite films with various concentrations of vanadium oxide are shown in Figure 4-21. The absence of an -OH stretching band between $3500 - 3300 \text{ cm}^{-1}$ demonstrates that after the heat treatment at 80°C the nanocomposite films do not contain water or alcohol, commonly produced by sol-gel synthesis for the formation of vanadium oxide.[8, 11, 13] With the addition of vanadium oxide a shoulder at 999 cm^{-1} appears and increases with VO_x concentration corresponding to the vanadyl stretching band ($\nu_{\text{V=O}}$).[14] The position and intensity of Si-O at 1105 cm^{-1} remains invariant with increasing VO_x , a further indication of the preferential interaction with POEM over PDMS.[5] The loading of vanadium oxide results in a change in the ether oxygen stretching band of POEM domains at 1146 cm^{-1} , as opposed to the ester oxygen at 1725 cm^{-1} .[15] This peak shifts to lower wave number with increasing vanadium concentration, indicating the electron donation resulting from the presence of the inorganic favors the ether oxygen over the ester oxygen.

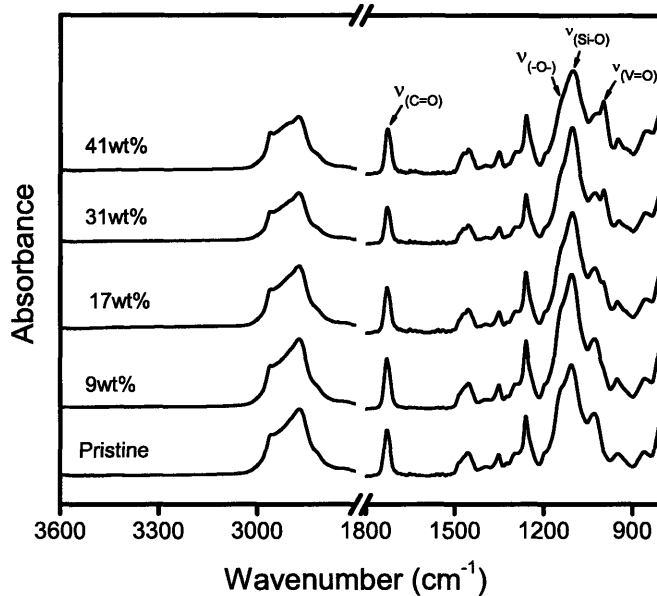


Figure 4-21: FT-IR spectra for pristine POEM-g-PDMS (70:30) and its nanocomposite films with various concentration of vanadium oxide.

Dynamic mechanical properties of POEM-g-PDMS/ VO_x nanocomposite films were investigated using a strain-controlled rheometer as described in the previous chapter. Despite the low glass transition temperatures of both components in POEM-g-PDMS, microphase separation result in rubbery mechanical properties. Figure 4-22 shows the storage (G') and loss moduli (G'') of the graft copolymer/ V_2O_5 nanocomposite films as a function of reduced frequency at 30°C.

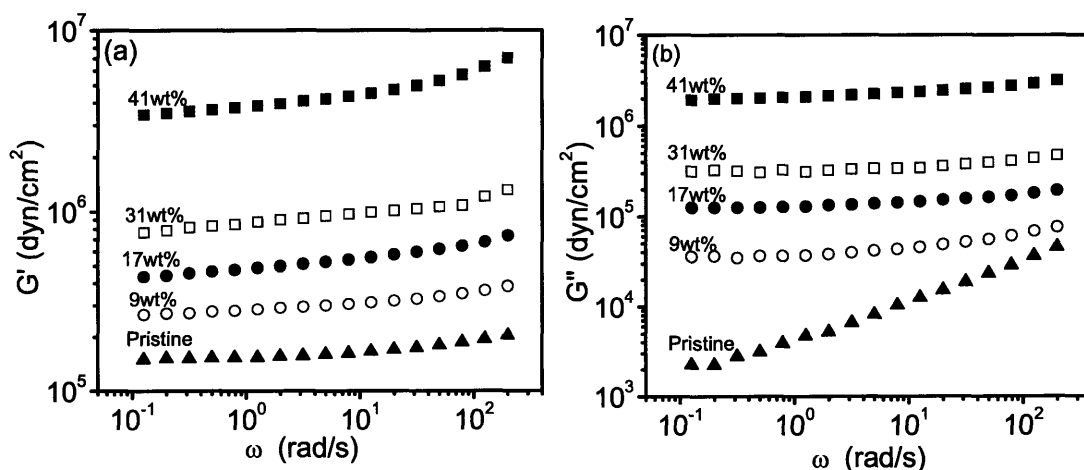


Figure 4-22: (a) Storage (G') and (b) loss (G'') moduli for pristine POEM-g-PDMS (70:30) and its nanocomposite films with various concentration of vanadium oxide.

These figures demonstrate the microphase-separation of the graft copolymer that provides the solid-like nature of the pristine material, showing $G' > 10^5$ dyne/cm² and $G'' \sim \omega^{0.5}$ as described previously.[3] The excellent mechanical properties of the graft copolymer originate from the interfaces created by the microphase separation of the two components. The POEM homopolymer (not shown) exhibits the low-frequency scaling behavior $G'' \sim \omega$, indicating its molten and liquid-like state.[6] Upon the addition of vanadium oxide, both the storage and loss moduli dramatically increase, due to the increased mechanical properties of the inorganic. The mechanical properties of the nanocomposite films increase with vanadium oxide concentration, but jump abruptly at 41 wt%. This composition is consistent with the upper limit in vanadium oxide concentration for the preservation of microphase-separated films, as confirmed by SAXS, and DSC.

Summary

Using sol-gel chemistry, nanostructured vanadium oxide was grown within the POEM domains of rubbery block and graft copolymers. The polymer morphology successfully directed the structure of the vanadium oxide. The microphase separation of the block and graft copolymer films was preserved up to a limit in inorganic compound loading. Co-assembled nanocomposite films incorporating up to 34 wt% vanadium oxide were flexible and semi-transparent within POEM-*b*-PBMA and up to 31 wt% vanadium oxide for POEM-*g*-PDMS. From investigation of the TEM micrographs in Figure 4-10, a factor of 9 increase in surface area was estimated by the structure-direction of vanadium oxide within POEM-*b*-PBMA over that of dense vanadium oxide. Cyclic voltammetry and impedance spectroscopy confirmed the preservation of the redox properties of the vanadium oxide and the ion-conductive properties of the polymer in composite films.

This chapter investigated the following questions:

1. Can microphase-separated polymers be used to direct cathode active materials, such as transition metal oxides?
2. Are the resulting microstructures continuous and on an appropriate size scale?

The microphase-separating polymers POEM-*b*-PBMA and POEM-*g*-PDMS were successfully used to direct the synthesis of the transition metal oxide, vanadium oxide. The final film was flexible and the final oxide structure was continuous within the POEM domain. The composite film retained both the ionic conductivity of the neat polymer and the ability to intercalate Li⁺ within the vanadium oxide. Therefore, *in situ* sol-gel chemistry methods were successfully used to structure-direct growth of an inorganic phase within microphase-separated copolymers.

References

1. Templin, M. et al. "Organically Modified Aluminosilicate Mesostructures from Block Copolymer Phases." *Science*, **1997**, 278, 1795-1798.
2. Trapa, P. E., Huang, B., Won, Y.-Y., Sadoway, D. R. & Mayes, A. M. "Block Copolymer Electrolytes Synthesized by Atom Transfer Radical Polymerization for Solid-State, Thin-Film Batteries." *Electrochemical and Solid-State Letters*, **2002**, 5, A85-A88.
3. Trapa, P. E. et al. "Rubbery Graft Copolymer Electrolytes for Solid-State, Thin-film Lithium Batteries." *Journal of the Electrochemical Society*, **2005**, 152, A1-A5.
4. Albinsson, I., Mellander, B. E. & Stevens, J. R. "Ionic Conductivity in Poly(propylene glycol) complexed with Lithium and Sodium triflate." *Journal of Chemical Physics*, **1992**, 96, 681-690.
5. MacCallum, J. R. & Vincent, C. A. in *Polymer Electrolyte Reviews* (Elsevier Applied Science, London and New York, 1987).
6. Soo, P. P., Huang, B., Y-M., C., Sadoway, D. R. & Mayes, A. M. "Rubbery Block Copolymer Electrolytes for Solid-State Rechargeable Lithium Batteries." *Journal of the Electrochemical Society*, **1999**, 146, 32-37.
7. De Paul, S. M., Zwanziger, J. W., Ulrich, R., Wiesner, U. & Spiess, H. W. "Structure, Mobility, and Interface Characterization of Self-Organized Organic-Inorganic Hybrid Materials by Solid-State NMR." *Journal of the American Chemical Society*, **1999**, 121, 5727-5736.
8. Dunn, B., Farrington, G. C. & Katz, B. "Sol-gel approaches for solid electrolytes and electrode materials." *Solid State Ionics*, **1994**, 70/71.
9. Guerra, E. M., Ciuffi, K. J. & Oliveira, H. P. "V₂O₅ xerogel-poly(ethylene oxide) hybrid material: Synthesis, characterization, and electrochemical properties." *Journal of Solid State Chemistry*, **2006**, 179, 3814-3823.
10. Demeter, M., Neumann, M. & Reichelt, W. "Mixed-valence vanadium oxides studied by XPS." *Surface Science*, **2000**, 454-456, 41-44.

11. Sudant, G., Baudrin, E., Dunn, B. & Tarascon, J. M. "Synthesis and Electrochemical Properties of Vanadium Oxide Aerogels Prepared by a Freeze Drying Process." *Journal of the Electrochemical Society*, **2004**, 151, A666-A671.
12. Miller, R. L. & Boyer, R. F. "X-Ray Scattering from Amorphous Acrylate and Methacrylate Polymers: Evidence of Local Order." *Journal of Polymer Science, Part B: Polymer Physics*, **1984**, 22, 2021-2041.
13. Rolison, D. R. & Dunn, B. "Electrically conductive Oxide Aerogels: new materials in electrochemistry." *Journal of Materials Chemistry*, **2001**, 11, 963-980.
14. Harreld, J. H., Wong, H. P., Dave, B. C., Dunn, B. & Nazar, L. F. "Synthesis and properties of polypyrrole-vanadium oxide hybrid aerogels." *Journal of Non-crystalline Solids*, **1998**, 225, 319-324.
15. Kim, J. H. et al. "Role of Polymer Matrix in Polymer/Silver Complexes for Structure, Interactions, and Facilitated Olefin Transport." *Macromolecules*, **2003**, 36, 6183-6188.

Chapter 5 : Electronic Conductivity

In the previous chapter, growth of a continuous, inorganic phase of vanadium oxide was structure-directed within the ion-conducting domain of the block copolymer, POEM-*b*-PBMA. The Li⁺-intercalating ability of vanadium oxide was preserved in the composite film and the polymer exhibited ionic conductivities comparable to that of the pure electrolyte material. The resulting structure was a continuous nanophase of vanadium oxide with increased surface area-to-volume ratio over that of either thin-film, fully-dense vanadium oxide or composite cathode films made with micron sized particles of vanadium oxide. The next step was to incorporate this composite film into battery test cells to assess its viability as a cathode material. To act as a cathode in a discharging and charging cell, the material must be able to exchange electrons with the external circuit. This chapter will focus on techniques used to increase electronic conductivity between the external circuit and the cathode-active vanadium oxide dispersion in the film while still preserving the POEM-*b*-PBMA structure present in the film. Successful incorporation of such a cathode would enable an all solid-state, mechanically flexible battery.

This chapter will address the following questions:

1. Can these structure-directed materials be used as cathodes? What electronic conductivity additives are necessary to make them usable?
2. Do these nanocomposite cathodes offer an improvement to a particular set of battery metrics, e.g. rate capability?

More specifically, this chapter describes several techniques used to increase the electronic conductivity of the composite film in order to attempt to access the full capacity of the vanadium oxide. The chapter begins with a brief description of attempts to improve conductivity through the addition of silver. Two approaches are then described in detail: (1) incorporation of the conducting polymer, poly(3,4-ethylenedioxythiophene) (PEDOT); (2) the use of a dispersion of carbon black. Carbon black provided the most

robust conductivity additive and the films synthesized with carbon black enabled the examination of electrochemical limitations within the composite film.

Without additive

To verify the need for an electronically conducting additive, a POEM-*b*-PBMA/VO_x film acting as a control was cycled in a cell comprised of a lithium anode and using LP50 liquid electrolyte as described in Chapter 3. This film also contained a lithium salt, LiCF₃SO₃, added to the copolymer prior to the vanadium oxide sol-gel process. The cycling behavior, discharged at C/30, is shown below in Figure 5-1. It is evident that the poor electronic conductivity of vanadium oxide within the composite film results in substantial ohmic losses and thereby reduces the useful cell voltage. The internal resistance caused by the low electronic conductivity reduces the capacity of vanadium oxide because the drop in cell voltage results in termination of the discharge before realizing the full capacity of the electrode material.[1] The capacity in the first discharge was < 10 mAh/g.

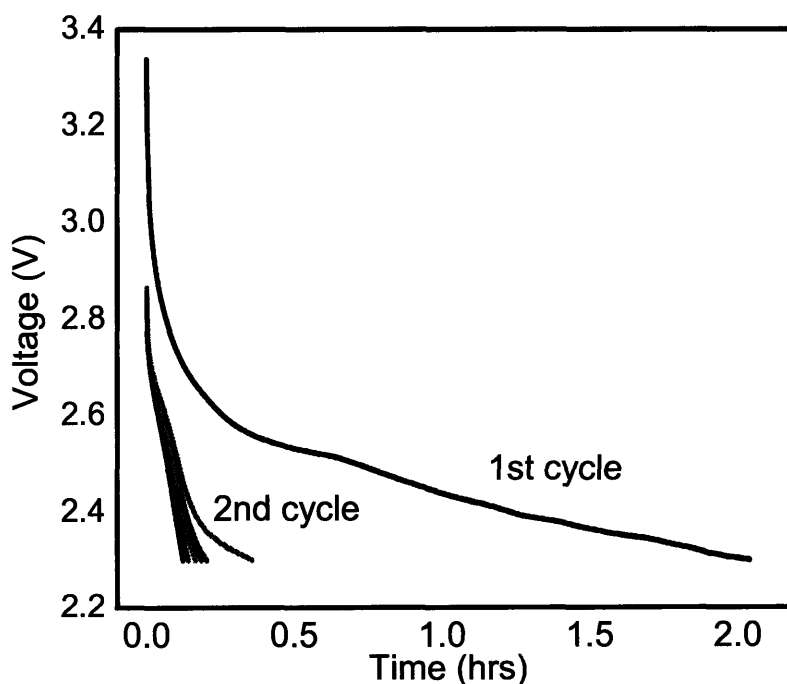


Figure 5-1: Galvanostatic cycling of POEM-*b*-PBMA/VO_x film from 2.3 V – 3.6 V at C/30.

Several techniques were used to improve the conductivity of the cathode films. The intent was to synthesize a film wherein the electronic additive was directed to the same film regions as the vanadium oxide and POEM. However, the vanadium oxide still needed to be accessible to insertion of Li^+ ions in order to realize the benefits of the nanoscale architecture as described in Chapter 4. The advantages and disadvantages of alternative ways of improving conductivity will be presented along with results from electrochemical testing. The chapter will begin with a description of the use of the metallic additive, silver, and then describe the use of the conducting polymer, PEDOT. The last example, a dispersion of carbon black within POEM-*b*-PBMA/ VO_x , gave the most robust composite structure and enabled the cycling of an all solid-state mechanically flexible battery. These CB-containing composite films provided a way to probe the system electrochemically to provide further understanding of the limiting mechanisms.

Silver Salt

Silver salt was added to the composite film in several different varieties and weight percentages. The silver salt was dissolved in water, 30 wt% AgNO_3 and added to the solution of acetone, polymer and $\text{VO}(\text{O}^i\text{Pr})_3$. Silver vanadium oxide (SVO), $\text{Ag}_2\text{V}_4\text{O}_{11}$, cathodes are currently available commercially as primary batteries in implantable medical devices and boast capacities of 260 mAh/g over the voltage range 1.5 V – 3.6 V for a current of 0.08 mA/cm². [2] SVO cathodes enable high currents necessary for these implantable cardiac defibrillators, but the reversibility for silver oxidation/reduction coupled with lithium insertion has been a challenge for rechargeable batteries. [3] The disadvantage with metallic additives over that of carbon or polymers is their high density, leading to an increase of “dead” weight in the cathode system. In addition, the literature indicated that carbon might still be necessary as an additive and that the metal species could not serve as additives on their own. [3-7] As a result, ~ 30 wt% silver was necessary to achieve cycling capabilities for these films. The data shown below are using AgNO_3 , thermally reduced at 150°C. Evidence that elevated temperature was required for the reduction of silver can be found from WAXS data comparisons between heated and unheated POEM-*b*-PBMA/ VO_x /Ag films shown in Figure 5-2. The peaks at 38.1° and 44.5° are characteristic of metallic silver. [8] This figure also shows the

WAXS spectra for AgNO_3 powder indicating complete conversion of this salt to metallic silver in the final film.

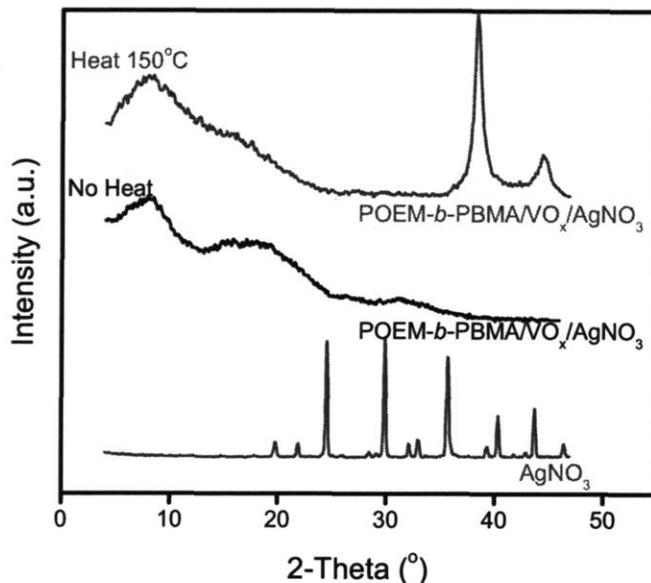


Figure 5-2: WAXS spectra for POEM-*b*-PBMA/VO_x/Ag film heat treated at 150°C (red, upper) without heating (black, middle) and AgNO₃ powder (grey, bottom).

The reduction of Ag^+ ions formed metallic Ag particles throughout the film that are less than 20 nm, as shown in Figure 5-3.

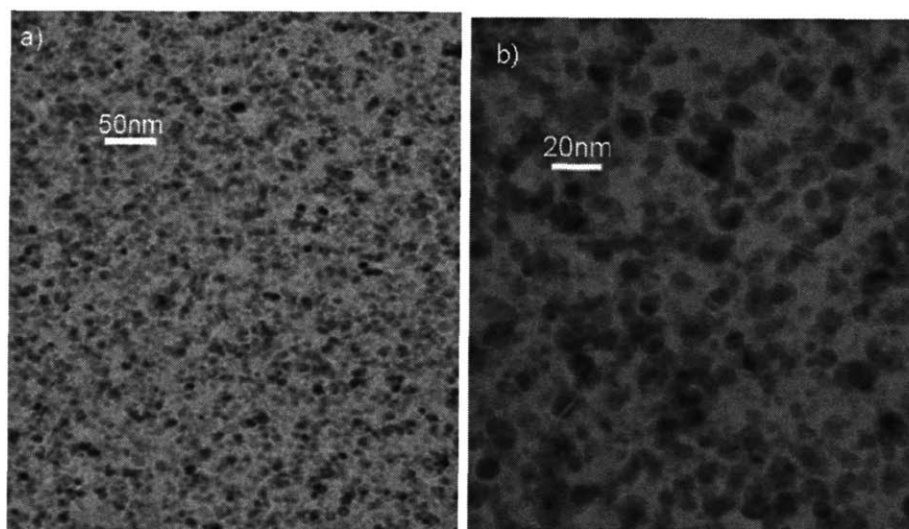


Figure 5-3: TEM micrographs of POEM-*b*-PBMA/VO_x film containing Ag particles a) lower magnification b) higher magnification of the same film.

The particles appear localized in the hydrophilic domains. The visible characteristic length scale corresponds to the ~ 30 nm periodicity of the block copolymer domain. The second micrograph (Figure 5-3b) shows a higher magnification of the same film. Vanadium oxide is not discernable in these micrographs. It was hypothesized that the high electron density of silver dominated the image contrast in the experiment and resulting images. The mechanical properties of the stiffer PBMA domains appear able to hinder the aggregation of large particles of silver. Similar films were synthesized using the POEM-*g*-PDMS graft copolymer matrix and large aggregations of silver were formed that were not confined to the hydrophilic domains. One such aggregation is shown in Figure 5-4. It was hypothesized that the higher glass transition of PBMA versus that of PDMS prevented “breakout” of the Ag particles that would have led to large aggregations of metal.

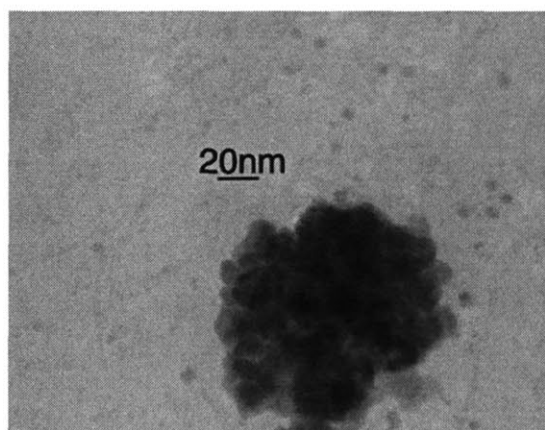


Figure 5-4: TEM micrograph of POEM-*g*-PDMS/VO_x film containing Ag.

In order to cycle these films they had to be cast on aluminum foil. Freestanding films of POEM-*b*-PBMA/VO_x/Ag were not cyclable in galvanostatic tests; however, when cast on Al foil they showed some capacity, which decreased upon cycling. Capacity was also difficult to calculate accurately for these films because of the presence of silver in the film and the low weights that were used. The cycling data, using LP50 liquid electrolyte and lithium foil anode, is shown below in Figure 5-5. This film contained 27 wt% V₂O₅ and 30 wt% AgNO₃ and the thickness of the cathode cast on aluminum foil was between 1 and 5 μ m. The first discharge capacity was measured as 120 mAh/g,

based on the V_2O_5 mass, with substantial capacity fade upon cycling. These films showed no capacity when cycled using a solid electrolyte.

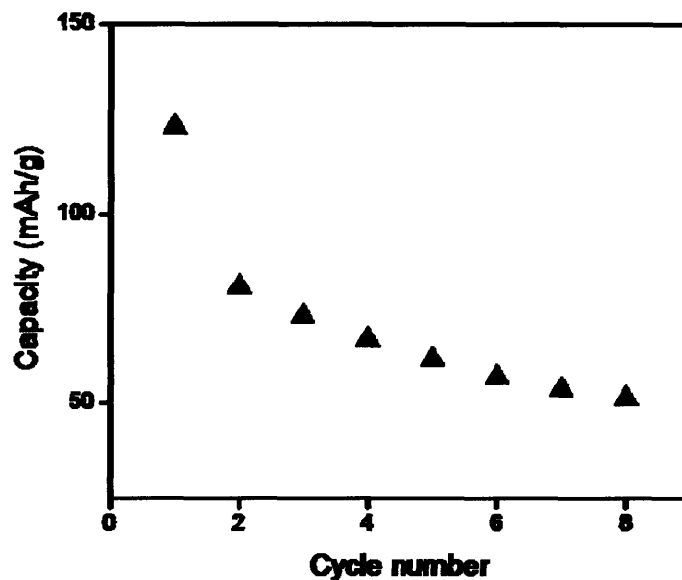


Figure 5-5: POEM-*b*-PBMA/ VO_x /Ag cycling data at C/20.

PEDOT

Poly(3,4-ethylenedioxythiophene) (PEDOT) was investigated as a conductive additive for the POEM-*b*-PBMA/ VO_x composite. As indicated in the literature and described in chapter 2, PEDOT would be conductive in the voltage range of interest and would therefore be able to replace carbon as a conductivity additive.[9] The challenge was to have PEDOT in contact with the vanadium oxide phase so that its capacity might be accessed, and to maintain the fine, networked structure of the vanadium oxide. Several techniques were employed to add PEDOT to POEM-*b*-PBMA/ VO_x , including chemical vapor deposition, electrodeposition and *in situ* oxidative polymerization of the EDOT monomer by vanadium oxide.

Capacity of PEDOT

To determine the theoretical capacity of PEDOT in the voltage range of interest, a film of PEDOT was electrodeposited and cycled in a three-electrode configuration. As explained in Chapter 3, this was performed in a three-electrode cell with EDOT monomer dissolved in the electrolyte solution of 0.05 M TBAClO₄ in propylene carbonate. This

deposition was on a working electrode of Au or ITO in order to run a control on the PEDOT capacity. This was a stepped potential deposition (as opposed to swept potential, seen later on)[10] as shown below in Figure 5-6.

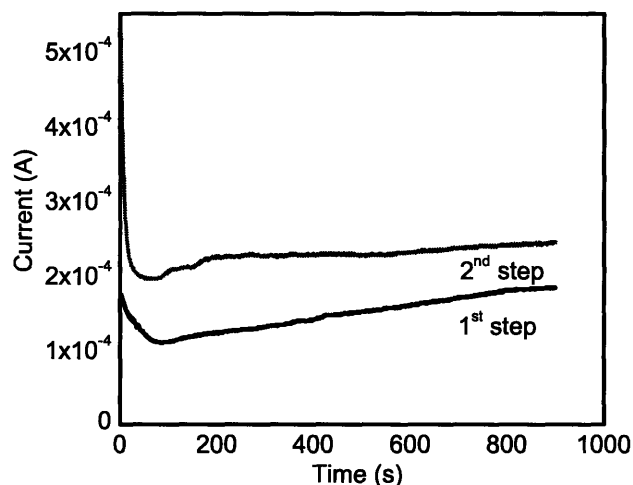


Figure 5-6: PEDOT deposition on Au electrode, potential held at 1.02V vs. Ag/Ag⁺ in 0.05 M TBAClO₄ in PC with 3 mmol of EDOT. RE: Ag/AgNO₃ in acetonitrile, CE: Pt.)

This sample was then cycled over the voltage limits 2.1 – 3.5 V vs. Li to replicate the voltage range seen by the cycling experiments. This voltammogram shown in Figure 5-7a was similar to that found in the literature are reproduced in Figure 5-7b.

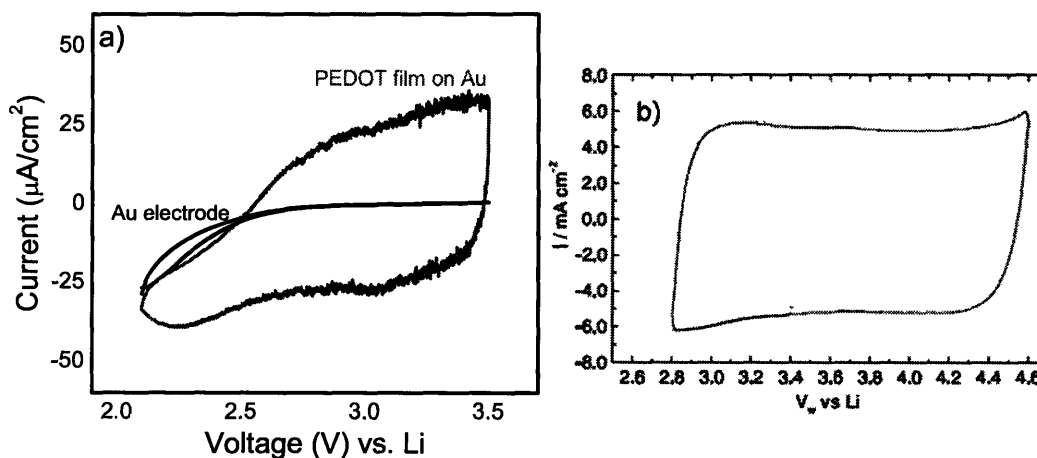


Figure 5-7: Cyclic voltammogram of PEDOT at 20mV/s vs. Li a) film deposited on gold b) film from literature [11] PEDOT on Pt both films at 20 mV/s in 1 M LiPF₆ 2:1 (EC:DMC) with lithium foil as CE and RE.

The voltage ranges shown in these figures are slightly different because the latter experiment was investigating PEDOT's use for LiMnO_x compounds. Both CVs indicate the capacitive behavior of the system within the voltage range depicted. PEDOT is conductive within this range, although for the experimental film studied here in Figure 5-7a, the higher end of the voltage range shows higher capacity. From the data in Figure 5-7, the capacity of the film synthesized on the Au electrode was ~ 20 mAh/g (calculated from the mass of the PEDOT deposited and the current from the graph above). This number corresponded well with values found in the literature of 25 mAh/g and was used as the capacity from PEDOT alone in previous investigations.[11]

Chemical Vapor Deposition

A 200 nm layer PEDOT film was deposited, via chemical vapor deposition (CVD), onto a POEM-*b*-PBMA/ VO_x composite film containing 30 wt% vanadium oxide. As indicated in Chapter 3, FeCl_3 was used as an oxidizing agent and was removed by washing several times with methanol after the deposition.[12] The mechanical properties of the film were preserved after the addition of the PEDOT film and the rinse step, despite the brittle characteristics of conductive polymers.[13] It was hypothesized that there might be some infusion of the PEDOT film into the vanadium oxide composite to allow for electronic conduction, thereby enabling cycling. A battery using liquid electrolyte, POEM-*b*-PBMA/ VO_x /PEDOT as a cathode and lithium foil as an anode was constructed and cycled at a rate of $C/20$. The PEDOT coated side was placed in contact with the stainless steel current collector. The cycling data from this film are shown below in Figure 5-8. As is evident from the discharge curves, there is some capacity obtained from this film.

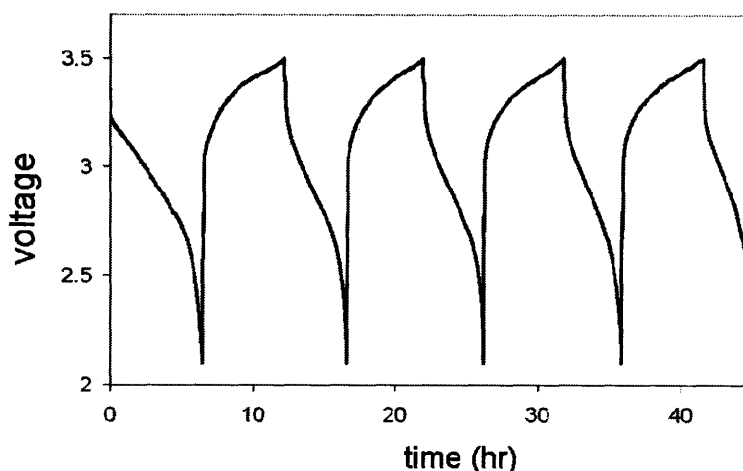


Figure 5-8: Charge /Discharge curves from the POEM-*b*-PBMA/VO_x/PEDOT(CVD) film, cycled from 2.1 V - 3.5 V at 20 μA/cm².

The capacity of the POEM-*b*-PBMA/VO_x/PEDOT(CVD) film as a function of cycle number is shown below in Figure 5-9. The capacity upon discharge for the first cycle is ~ 35 mAh/g, calculated based on the weight of vanadium oxide in the film. The capacity decreases upon cycling to ~ 20 mAh/g after 6 cycles.

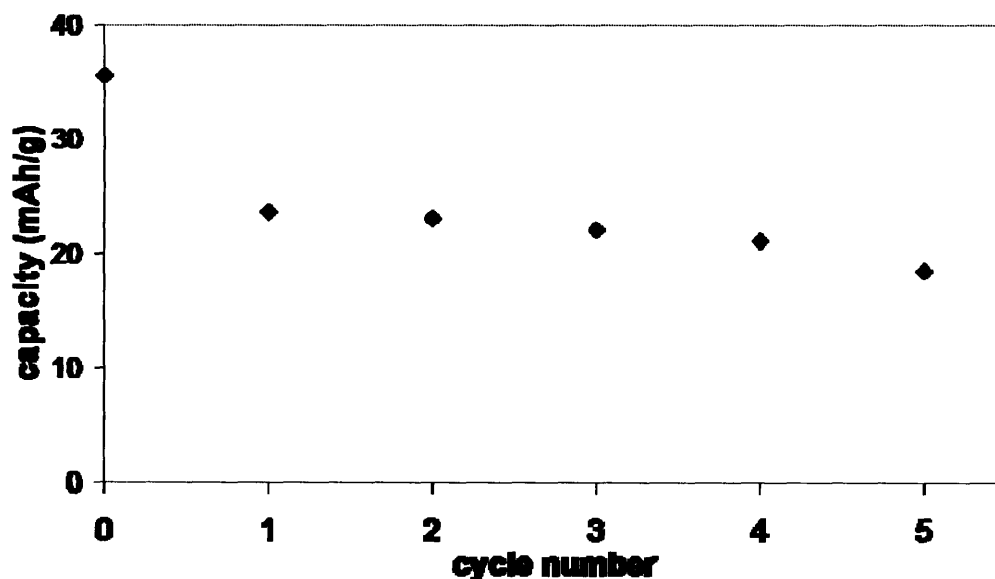


Figure 5-9: Capacity from POEM-*b*-PBMA/VO_x/PEDOT(CVD) as cathode from 2.1 V - 3.5 V at 20 μA/cm².

Evidence suggesting that capacity from vanadium oxide was accessed when cycling the POEM-*b*-PBMA/VO_x/PEDOT(CVD) film can be found from calculations

based on the mass of PEDOT. The mass of PEDOT in the cathode was 0.01 mg. Assuming 100% capacity from PEDOT this would only provide 0.3 μAh of capacity while this film provided 80 μAh . In addition, Assuming a theoretical capacity for VO_x of 147 mAh/g over this voltage range, approximately 16% of this theoretical capacity of VO_x was accessed. This translates to a depth of 30 μm through the film, greater than the ~ 500 nm electronic conductivity limitation in vanadium oxide thin films.[14] These calculations indicates that the presence of PEDOT allowed some access to the vanadium oxide.

However, further characterization revealed an abrupt interface between PEDOT and the POEM-*b*-PBMA/ VO_x film. A cross-section of the sample was microtomed and examined by TEM. The imaging of this film indicates no apparent infusion of the PEDOT into the composite, as shown in Figure 5-10.



Figure 5-10: Cross-sectional STEM of CVD PEDOT film on POEM-*b*-PBMA/ VO_x film.

At higher magnification, EDX was used to map the sulfur content in the sample to further confirm that PEDOT was not present within the sample. The abrupt jump between the sulfur contained in the 200 nm PEDOT film and the nanocomposite film can be seen in Figure 5-11. The epoxy material is also sulfur containing.

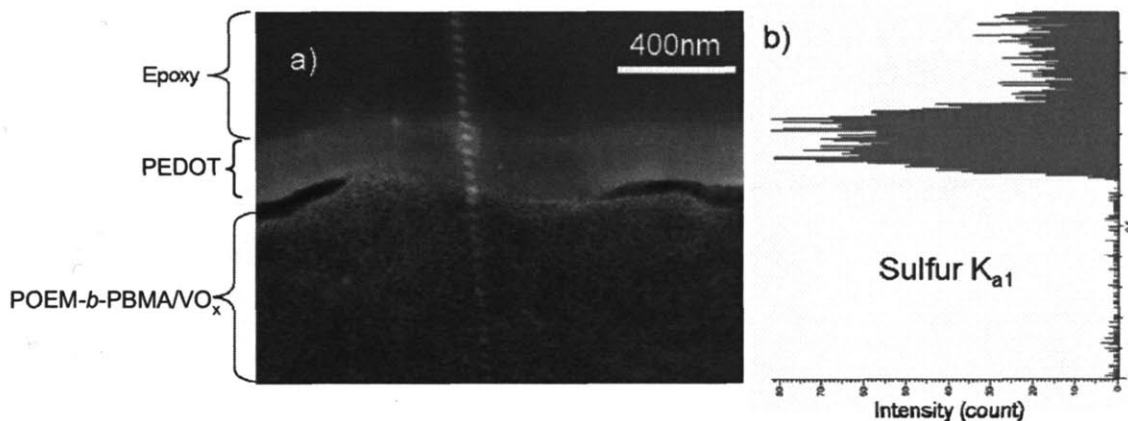


Figure 5-11: Higher magnification a) STEM micrograph with b) chemical map of sulfur.

The lack of gradient in sulfur on the composite side of the PEDOT interface indicates little infusion of the PEDOT into the POEM-*b*-PBMA/VO_x composite. However, based on the calculation of depth of discharge into the film, the PEDOT seems to have some effect on the electronic conductivity of the film. It is hypothesized that the PEDOT is acting as an enhanced current collector, enabling a more intimate contact with the composite film than is possible by the stainless steel current collectors, and the PEDOT film enables vanadium oxide to be less electronically limited than thin film VO_x sputtered on aluminum. The weak sulfur signal in the EDX map on the composite side of the interface may also indicate some small infusion of EDOT vapor during the CVD process that might also account for the enhanced capacity from vanadium oxide determined from the calculations above. Because of the high conductivity of CVD PEDOT films[12, 15], even a slight infusion of EDOT monomer may polymerize on the vanadium oxide and increase the electronic conductivity of the composite film.

The next attempt involved depositing PEDOT onto a vanadium oxide surface to determine whether electrodeposition could be used to ensure better contact between the vanadium oxide and the electronic conductor. The initial experiments were used to determine the variation in polymerization onset potential for PEDOT and to illustrate the ability of PEDOT to electrodeposit on vanadium oxide. The preliminary depositions also served to determine experimental conditions for later work with composites. To begin with, PEDOT was electrodeposited onto a sputtered thin film coating of vanadium oxide

on an ITO substrate. The voltammogram from the swept potential deposition is shown below in Figure 5-12.

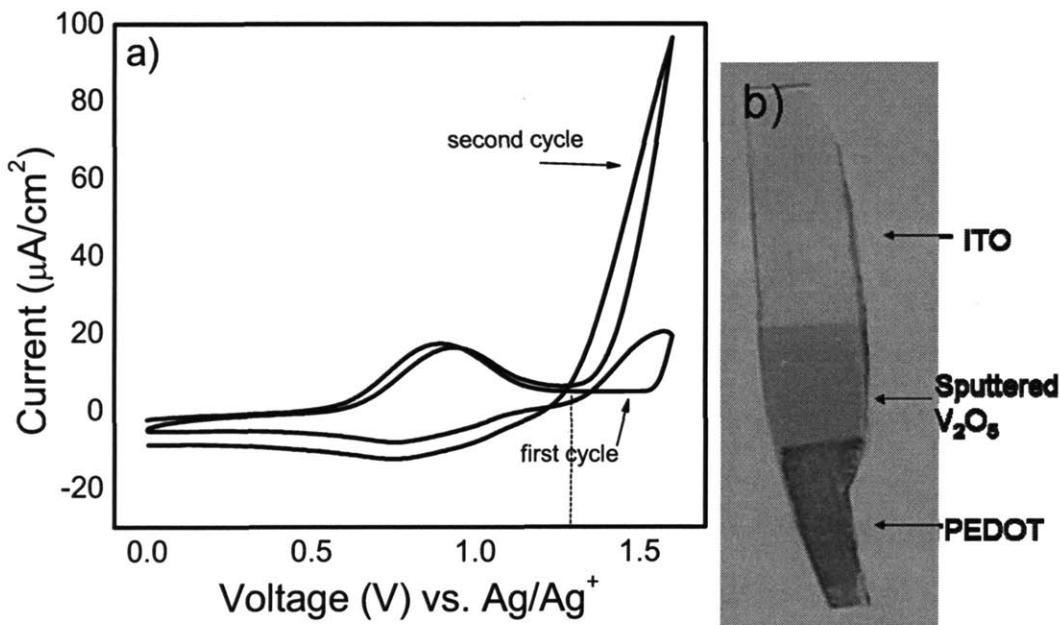


Figure 5-12: PEDOT deposition through cyclic voltammetry on vanadium oxide sputtered ITO a) CV of deposition at 20 mV/s in 0.1 M TBAClO₄ in PC containing 3 mmol EDOT. RE: Ag wire, CE: Pt. b) image of final film.

This voltammogram indicates that on the first cycle above the deposition potential (ca. 1.25 V vs Ag/Ag^+), a small amount of film is deposited, but because of the low electronic conductivity of the vanadium oxide substrate, the deposition is limited. However, as soon as some PEDOT is present on the electrode, the deposition proceeds much more rapidly and completely, as shown in the second cycle, due to the enhanced electronic conductivity of PEDOT over that of V_2O_5 . [16] An image of the final PEDOT film deposited on a sputtered film of vanadium oxide is shown in Figure 5-12b. The yellow region is a sputtered vanadium oxide film of ~ 200 nm while the blue region is the electrodeposited PEDOT film. The film thickness of vanadium oxide used is below the limit of electronic conductivity as shown by members of this group. [14] Therefore, PEDOT films were also deposited on thicker substrates including 0.1 mm thick POEM-*b*-PBMA/ VO_x films cast onto ITO slides or aluminum wire mesh. The CVs from a few such depositions are shown in Figure 5-13 and Figure 5-14.

These depositions show the same trend of increasing current with increasing number of cycles due to deposition of the conducting PEDOT film. In other words, the PEDOT deposition is autocatalytic.[17] The first two cycles are shown in Figure 5-13a indicating the increase in current, and twelve cycles are shown in Figure 5-13b to illustrate how the process proceeds. The same pattern is true for Figure 5-14. For the deposition shown in Figure 5-13, the reference electrode was a silver wire, while for the deposition in Figure 5-14 the reference electrode was Ag/AgNO₃ in saturated acetonitrile. This difference in reference explains the deviation for the onset of polymerization (ca. 1.02 V vs Ag/Ag⁺ and 1.2 V for Ag wire). The Ag/AgNO₃ reference was used in subsequent experiments and to fix the onset potential.

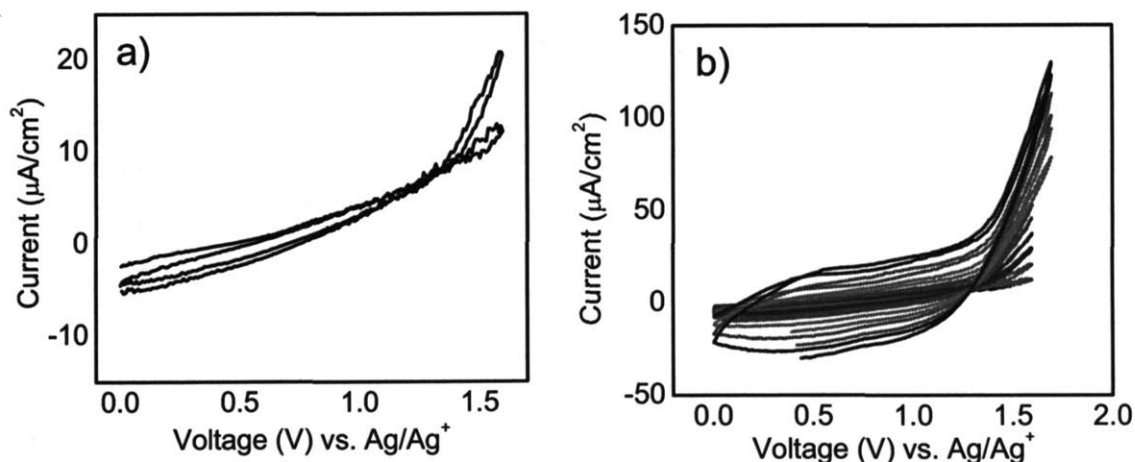


Figure 5-13: PEDOT deposition onto POEM-*b*-PBMA/VO_x coated Al wire mesh at 20 mV/s in 0.05 M TBAClO₄ in PC containing 3 mmol EDOT. RE: Ag wire, CE: Pt, a) the first two cycles of the deposition b) subsequent twelve cycles, the first 6 to sweep out to 1.5 V and the next 6 out to 1.7 V.

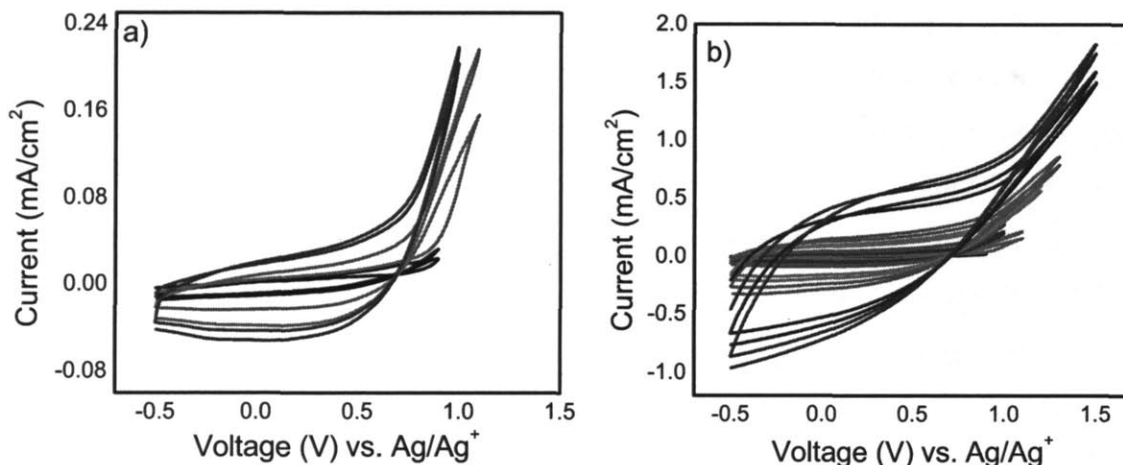


Figure 5-14: PEDOT deposition onto POEM-*b*-PBMA/VO_x coated ITO glass slide. scan rate = 20 mV/s; electrolyte = 0.05 M TBAClO₄ in PC containing 3 mmol EDOT. RE: Ag/AgNO₃ in saturated acetonitrile, CE: Pt a) the first six cycles of the deposition b) subsequent fourteen cycles.

Finally, in order to ensure PEDOT was in intimate contact with the transition metal oxide, a series of films were made with EDOT monomer added concurrently during sol-gel synthesis of vanadium oxide within POEM-*b*-PBMA. After dissolution of the polymer and addition of the (VO(OⁱPr)₃), 20 wt% EDOT was added dropwise to the stirring solution. After synthesis and evaporation, these films contained LiCF₃SO₃ (also added *in situ*), PEDOT, and sol-gel vanadium oxide structure-directed within POEM-*b*-PBMA. These films retained their mechanical flexibility as indicated by the photograph shown below in Figure 5-15.

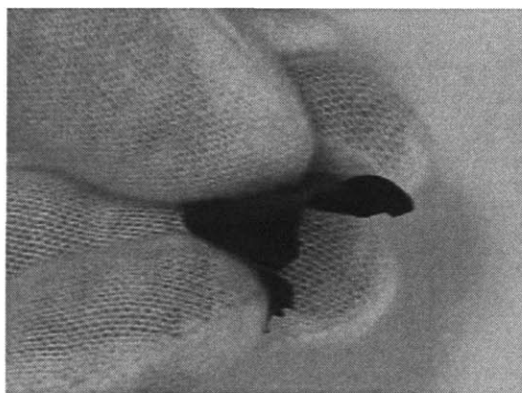


Figure 5-15: POEM-*b*-PBMA/VO_x film containing PEDOT added as monomer, chemically polymerized by vanadium oxide.

In this case the majority of EDOT monomer was chemically oxidized to PEDOT by vanadium oxide within the film. There was a visual change in the color of the solution during the stirring of the solution containing $\text{VO}(\text{O}^i\text{Pr})_3$ and EDOT monomer, from orange to black, indicating some initial oxidation of the monomer. The final polymerization occurs after casting the solution into the PTFE dish. To ensure that the final product did not contain unreacted EDOT monomer, the system was rinsed with propylene carbonate repeatedly and a final electro-oxidation step through sweep potential methods up to the onset of polymerization was performed, as shown in Figure 5-16. A potential step up to 1.02 V was performed between the first and second sweeps. The oxidation of remaining polymer was determined to be complete once the trace of the cycles overlapped, as can be seen in Figure 5-16 for the 3rd (blue) cycle.

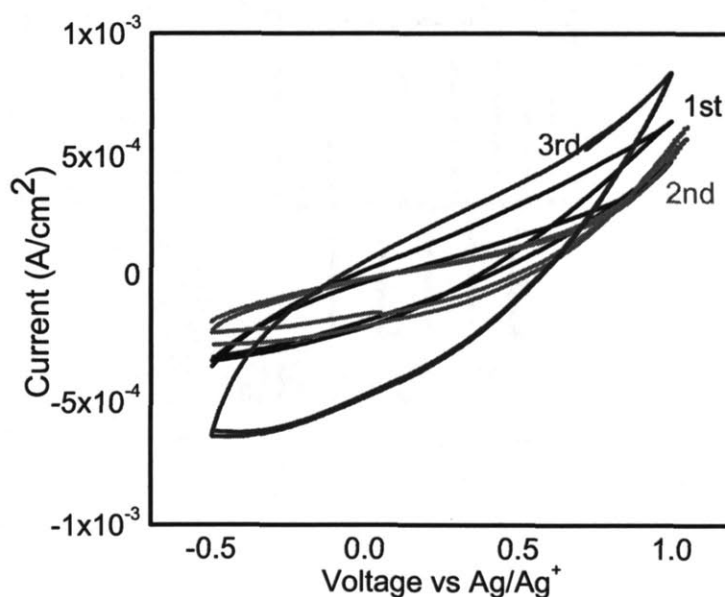
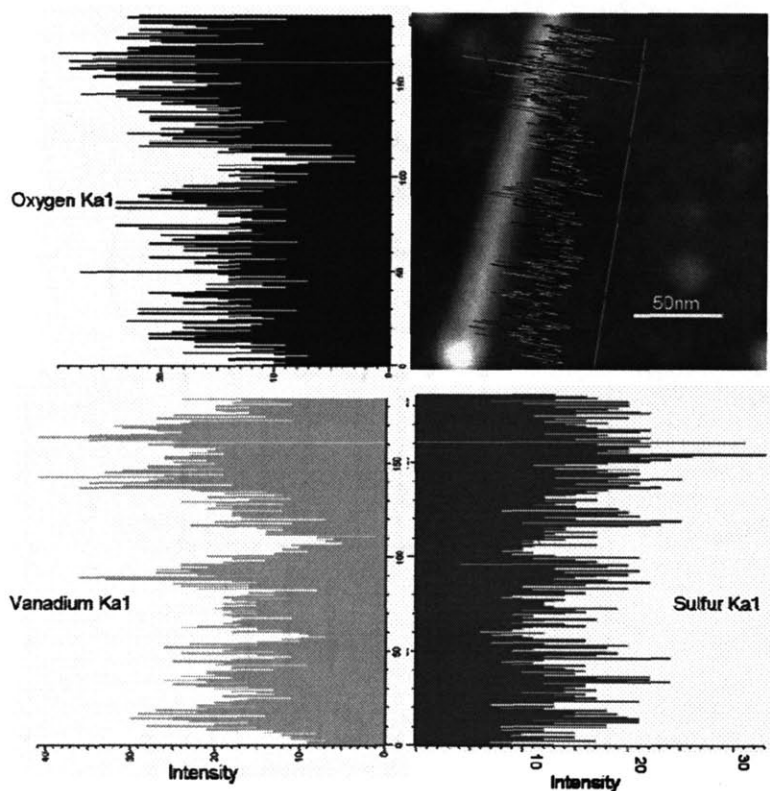


Figure 5-16: CV of electropolymerization of EDOT containing composite of POEM-*b*-PBMA/ VO_x at 20 mV/s, performed in 0.05 M TBAClO_4 in PC without monomer. RE: Ag/AgNO_3 in saturated acetonitrile, CE: Pt

These films were also characterized by TEM to determine whether there was PEDOT in contact with the vanadium oxide. As the epoxy used to microtome the samples contains sulfur (see Figure 5-11), these samples were microtomed in an alternative sample holder that does not require epoxy. Therefore, the presence of sulfur in these

samples is due only to the presence of PEDOT. EDX maps of sulfur confirmed the proximity of sulfur and vanadium with a correlation between the two, indicating vanadium oxide is involved in the PEDOT chemical polymerization (in addition there was no other oxidizing species present). Two line scans of the film are shown below in Figure 5-17. There was some degree of drift and beam contamination with this sample, but the uniformity of the vanadium oxide as seen in Chapter 4 is also observed.



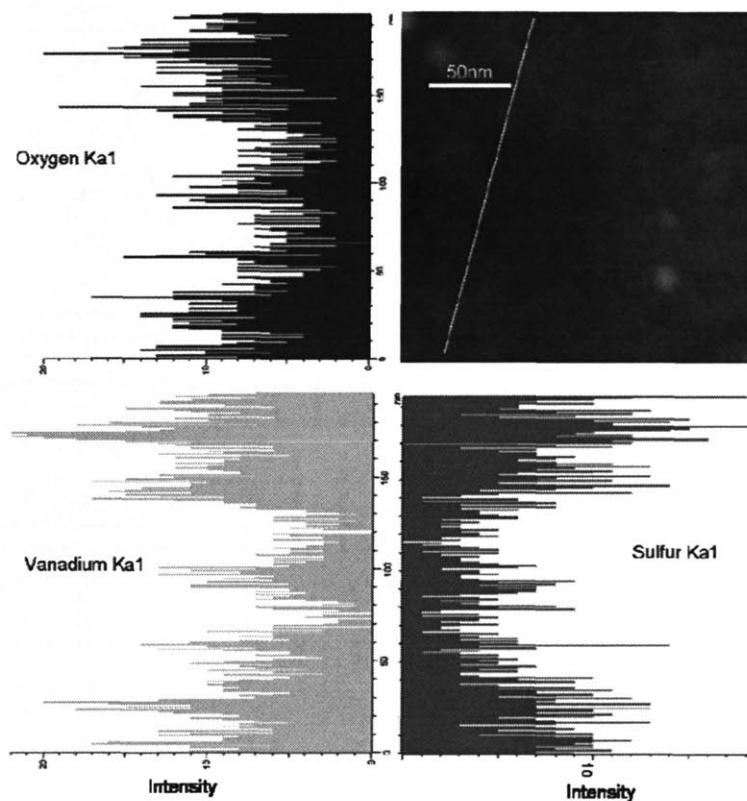


Figure 5-17: STEM cross sections mapping oxygen, sulfur and vanadium within POEM-*b*-PBMA/VO_x/PEDOT film.

Figure 5-17 indicates a prevalence of sulfur and vanadium throughout the film. The vanadium, sulfur and oxygen correlate with each other and the fibrous, ribbon-like structure is visible as seen for the POEM-*b*-PBMA/VO_x films (see Chapter 4). Finally, these ~ 100 μm films were cycled in a coin cell configuration using solid electrolyte, POEM-*b*-PBMA doped with LiCF₃SO₃, to determine the access to vanadium oxide capacity. The cells were cycled at 2.5 μA/mg. The cycling data is shown in Figure 5-18. The capacity of this film calculated based on the weight of each component of the system is shown in Table 5-1 below.

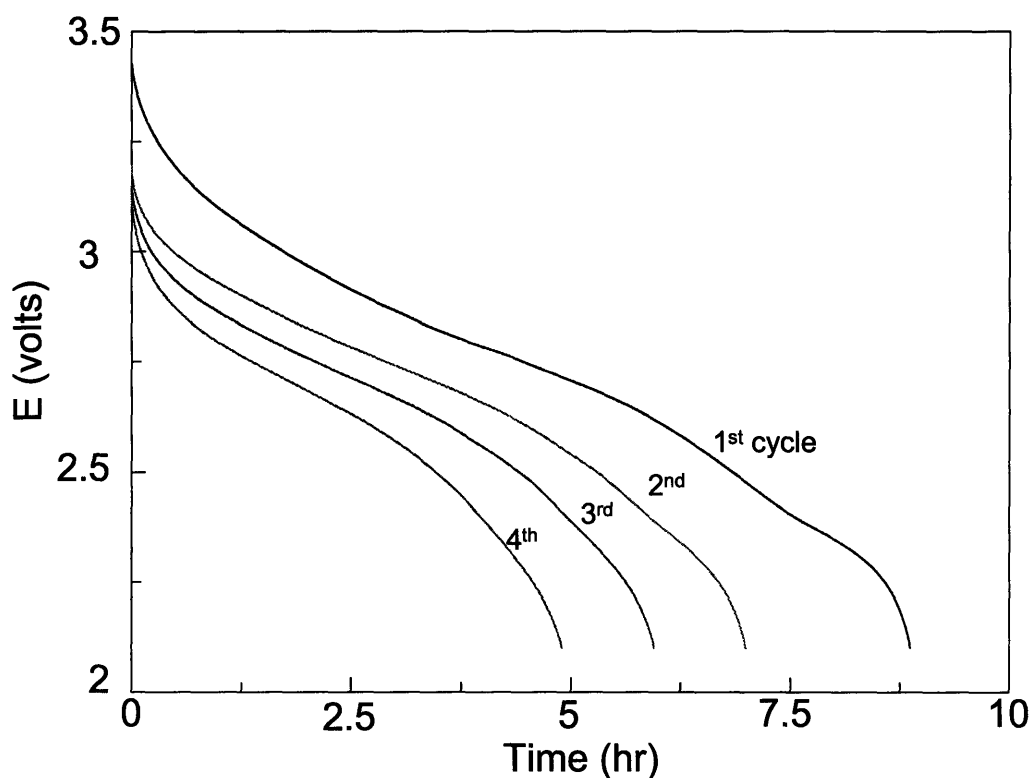


Figure 5-18: Cycling for 120 μm POEM-*b*-PBMA/ VO_x /PEDOT film at 2.5 $\mu\text{A}/\text{mg}$.

To differentiate values for capacity based on the different components of the film, the capacity was calculated assuming the weight of VO_x only, PEDOT only and then both, as shown in the first three columns of Table 5-1. The fourth column is the first column divided by the ~ 147 mAh/g theoretical capacity for vanadium oxide for the experimental voltage limits. The final column shows the depth through the film that would need to be accessed to provide the capacity in column 1. In other words, the final column shows the percentage of the entire film thickness that would need to be accessed in order to provide the calculated percentage of vanadium oxide capacity.

Table 5-1: Table of capacity and depth through film calculation for POEM-*b*-PBMA/ VO_x /PEDOT.

cycle	VO_x mAh/g	PEDOT mAh/g	Both mAh/g	% Theoretical of VO_x	Depth (μm)
1	22	30	13	15	20
2	18	23	10	11	14.3
3	15	20	8.5	10.1	13
4	12	16	7	8.3	10.4

The conductivity of these films was also measured to confirm that PEDOT percolated through the system and provided an improvement over the conductivity of the POEM-*b*-PBMA/VO_x film alone. The Nyquist plot for this film is shown in Figure 5-19 and the conductivity values for each semicircle (corresponding to multiple elements in the film) were 2.7×10^{-6} S/cm and 9×10^{-7} S/cm.

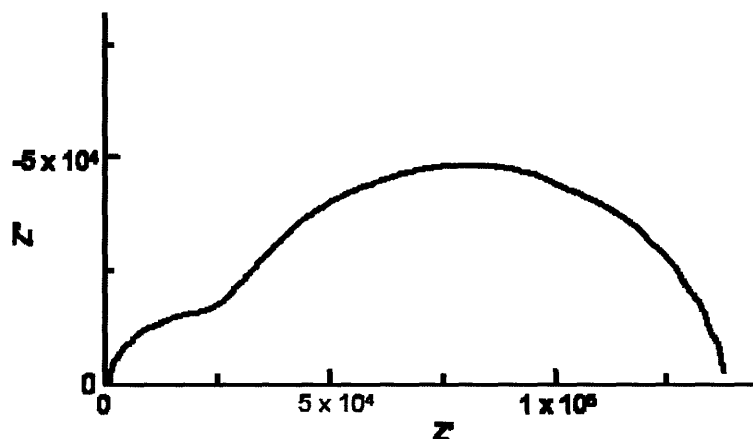


Figure 5-19: Impedance plot of POEM-*b*-PBMA/VO_x/PEDOT.

These films did not exhibit good cyclability, but the capacity of the first cycle is more than can be accounted for by PEDOT alone, since the calculated capacity of 30 mAh/g (Table 5-1) is above that determined for PEDOT (20-25 mAh/g). Hence it appears that vanadium oxide is at least partially accessed by Li⁺ ions. One reason for the lack of capacity could be that PEDOT blocks access to the vanadium oxide, making it difficult for Li⁺ ions to intercalate. Excess EDOT monomer was removed in a rinsing step and via electropolymerization so that capacity fade was determined to be film related rather than coming from polymerization of excess monomer. The advantage of this method is that the vanadium oxide and PEDOT are in intimate contact and capacity was obtained from an all solid-state cell; however, 20 wt% of PEDOT was necessary to obtain the 22 mAh/g first discharge capacity.

Carbon Black

Films containing POEM-*b*-PBMA and VO_x were combined with 5 wt% of the conductivity additive, carbon black (CB), to wire the system electronically. As described in Chapter 3, CB was added *in situ* during the sol-gel process. The main challenges of

using CB are that the carbon is hydrophobic and it aggregates into regions larger than the size scale of the polymer domains. In addition, the individual particles of the CB that was used (Super P) are around the size of the polymer domains, ~ 40 nm. However, this additive allowed the system to be probed electrochemically. The CB was treated with fuming sulfuric acid and exposed to a series of sonicating and cryogrinding steps, thereby improving contact with the vanadium oxide/POEM domain by increasing hydrophilicity and reducing aggregation of the particles. After acidification the CB powder remained suspended overnight in water. This indicated that re-aggregation was inhibited by the acidification steps. Approximately 0.1 mm solution-cast films containing POEM-*b*-PBMA/ VO_x and CB were mechanically flexible, as demonstrated in Figure 5-20. A TEM negative micrograph showing the final structure with the acid-treated CB is shown in Figure 5-21. Films were made with both the non-acid-treated and acid-treated carbon black powders (both subjected to the same sonication and cryo-grinding procedure). The data presented are for the acid-treated carbon black unless otherwise specified.

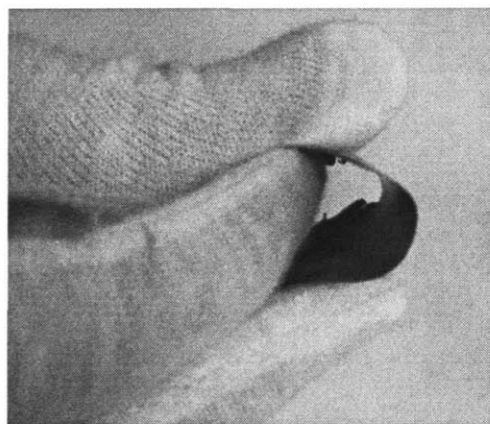


Figure 5-20: POEM-*b*-PBMA with 34 wt% VO_x and 5 wt% CB.

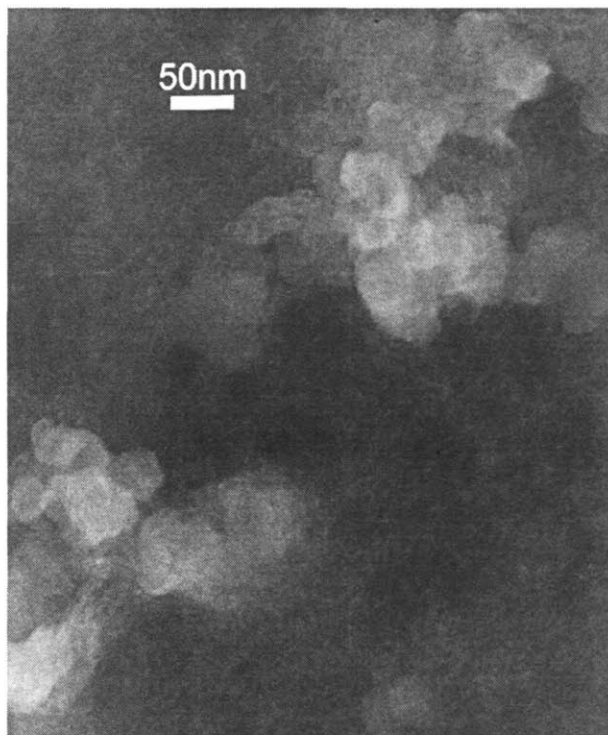


Figure 5-21: TEM negative micrograph of POEM-*b*-PBMA with 34 wt% VO_x and 5 wt% acid-treated CB.

The uniformity of the fine ribbon-like structure of VO_x described and depicted in Chapter 4 was preserved in the films containing CB. In Figure 5-20 the CB particles are visible (light spherical regions) along with the network structure of the VO_x; dark regions correspond to domains of PBMA. CB particles were percolated throughout the film, thereby providing a wiring harness, although some aggregation of the particles is observed.

The conductivity of the films, determined using ac impedance spectroscopy with blocking electrodes, demonstrates that the CB had percolated through the thickness of the film. The conductivity of the films with vanadium oxide alone was $\sim 10^{-10}$ S/cm, while with the addition of carbon black the value increases to close to 10^{-5} S/cm. A visual observation of the Nyquist plots for the conductivity measurement reveals a large difference between the cross-sectional conductivity of the vanadium oxide only films and the films containing carbon black. The Nyquist plots for films of the same area and thickness are shown below in Figure 5-22. Because the conductivity measurements are

taken through the cross section of the film, these plots offer further indication that the CB has percolated throughout the film.

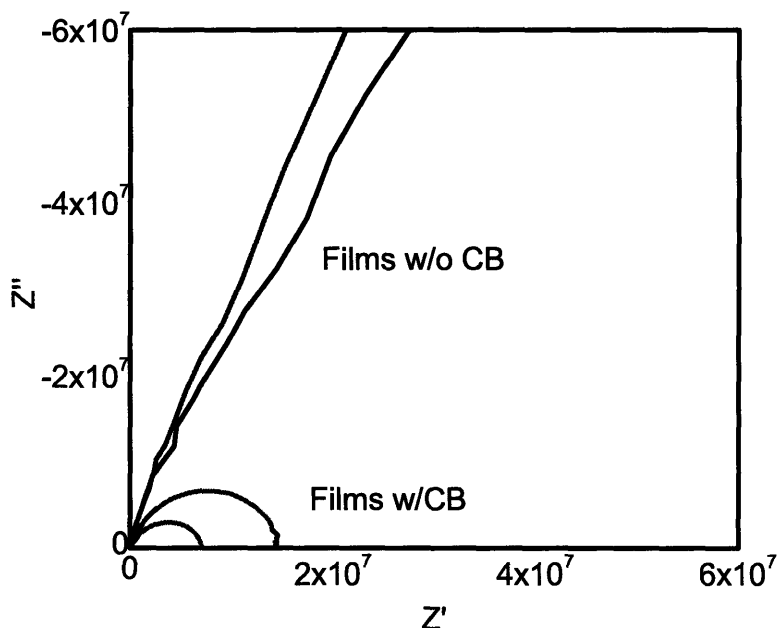


Figure 5-22: Nyquist plot of POEM-*b*-PBMA/VO_x with and without carbon black between blocking electrodes.

The film shown in Figure 5-21 was cycled in an all solid-state battery configuration with lithium foil as an anode. As described in Chapter 3, POEM-*b*-PBMA was used as an electrolyte doped with LiCF₃SO₃ at a Li:EO ratio of 1:20 and cast from anhydrous-THF onto the lithium foil anodes. A washer was used to protect the edges from shorting. The cathodes for these cells were either POEM-*b*-PBMA/VO_x containing acid-treated or non-acid-treated CB added *in situ* as described in Chapter 3.

The cycling data for the ~ 100 μm POEM-*b*-PBMA/VO_x films containing non-acid-treated CB are shown in Figure 5-23 at C/20 rate ($4.5 \mu\text{A}/\text{mg}$). The POEM-*b*-PBMA electrolyte thickness was ~ 50 μm . The capacity of the film, reversibly cycled for over 20 cycles was ~ 40 mAh/g. There is a decrease in the capacity after the first cycle, which is typical for vanadium oxides, but some recovery is observed upon further cycling. This increase in capacity has been seen previously in cycling data for batteries containing microphase-separated polymer electrolytes and could come from some orientation of the polymer domains.[18] There was a slight increase seen in initial cycles of CB and binder-

only films (there was negligible capacity from these films above 2.5 V). The capacity from the CB/binder-only films was still less than 2% of the total capacity obtained from these films and so could not alone account for the increase in capacity with cycling seen in Figure 5-23. The open circuit voltage for the cells made with carbon black versus lithium foil was 3.8 V.

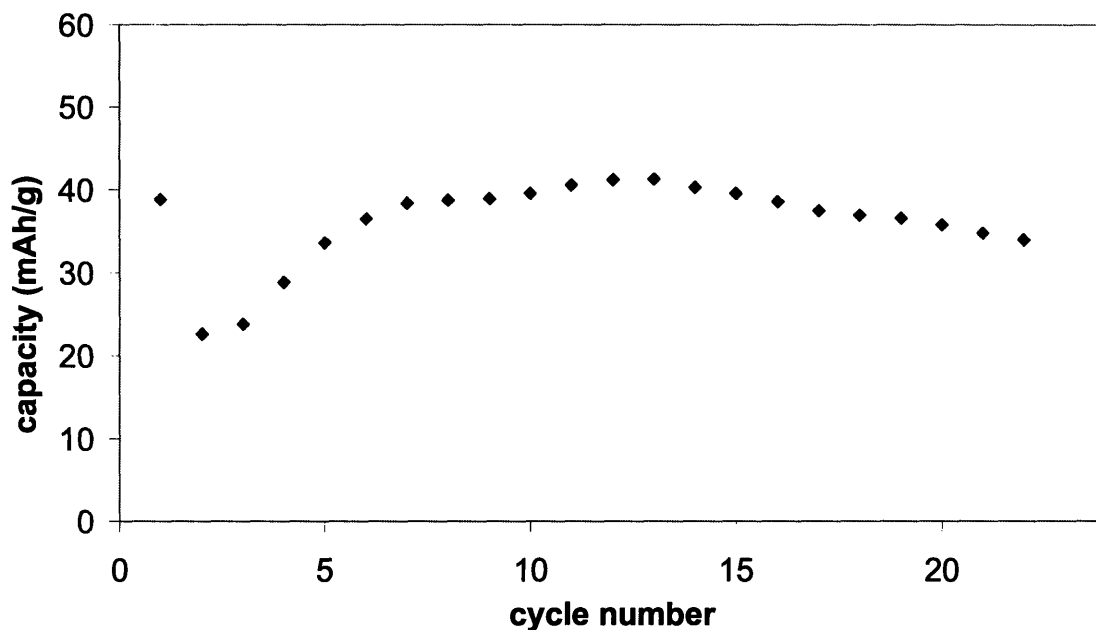


Figure 5-23: Cycling data for POEM-*b*-PBMA/VO_x/CB (non-acid-treated) film with solid electrolyte cycled at C/20.

Data for the POEM-*b*-PBMA/VO_x films with acid-treated CB and non-acid-treated (shown again for comparison) are shown Figure 5-24. The acid-treated CB shows an improved capacity compared to the non-acid-treated on the first and second cycle, but this capacity rapidly decays by the 7th cycle to around the same value as the non-acid-treated sample, ~ 40 mAh/g. The same increase in capacity is not seen for the films with acid-treated carbon black. It is hypothesized that the mechanism causing the decrease between the 1st and 7th cycles for the acid-treated film overshadows the increase upon cycling seen in the non-acid-treated films.

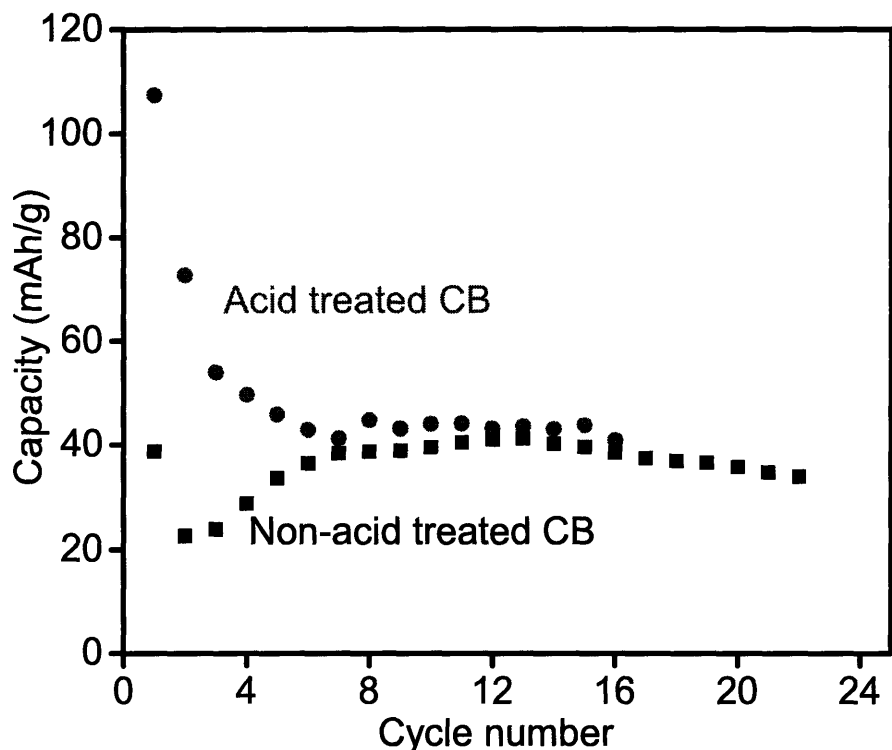


Figure 5-24: Cycling data for POEM-*b*-PBMA/VO_x/CB (acid-treated and non-acid-treated) film with solid electrolyte at C/20.

To verify that capacity was obtained from intercalation of Li⁺ into vanadium oxide, control films were tested by cyclic voltammetry in a three electrode configuration. Voltammograms of POEM-*b*-PBMA films incorporating VO_x, CB or both are shown in Figure 5-25. A blow up of the CV curve for the POEM-*b*-PBMA film with only vanadium oxide is shown as well, in order to show redox detail (this CV was shown in Chapter 4). The POEM-*b*-PBMA/VO_x film alone is characterized by a set of corresponding redox peaks (-0.55 V and 0.9 V) reflecting intercalation/de-intercalation of Li⁺ into/out of the VO_x structure. The film containing both CB and VO_x exhibits those same peaks, which are similar to those in the literature,[19] but the current obtained from the POEM-*b*-PBMA/VO_x/CB is higher by a factor of 20.[20]

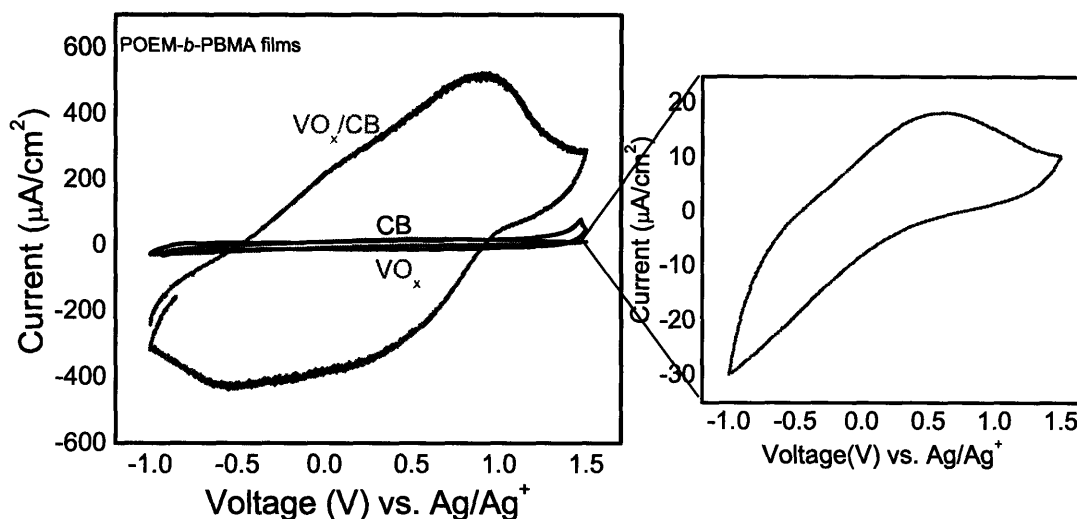


Figure 5-25: CV for POEM-*b*-PBMA films from -1.0 to 1.5 V vs. Ag/Ag⁺ at 50 mV/s in 1 M LiClO₄ in PC a) containing VO_x and/or CB (acid-treated) components b) VO_x.

Carbon black: Performance Limitations of the Battery

Even though this film cycled reversibly as a solid-state battery, the capacity was a great deal lower than the theoretical capacity for vanadium oxide, 147 mAh/g. To investigate one potential cause of this limited performance, cathodes were cycled with solid electrolyte of three different thicknesses. The curves for the second discharge cycle for these films, shown in Figure 5-26, indicate a featureless profile, as would be expected from an amorphous material. These data are for ~ 100 μm POEM-*b*-PBMA/VO_x/CB (acid-treated) films. Because of the decrease in capacity upon cycling, the data are plotted from the 2nd cycle. The test was repeated three times for each thickness to verify reproducibility. The total capacity for these films varied by ~ 5-10 mAh/g for each electrolyte thickness; however, the trend of decreasing capacity was always seen with increasing solid electrolyte thickness. Increasing the thickness of the solid electrolyte from 30 μm to 90 μm decreases the capacity obtained from the film. The 2nd discharge capacities at ~30, 60 and 90 μm were, respectively, 97, 63 and 22 mAh/g. It is important to note that there is also “electrolyte” within the 100 μm cathode film in the form of the POEM-*b*-PBMA matrix. These data indicate that one possible limitation in the battery’s performance could be the ionic conductivity of the electrolyte within the cathode.

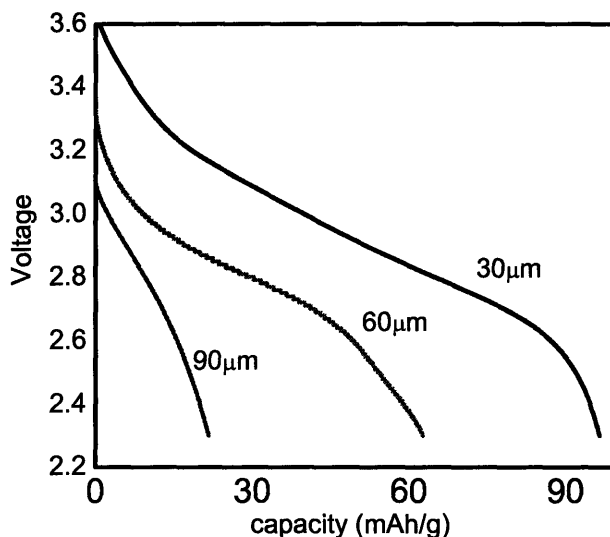


Figure 5-26: Discharge profiles from 2nd cycle of POEM-*b*-PBMA/VO_x/CB (acid-treated) films with varying thickness of solid electrolyte.

Carbon black: Advantages of system

The data above indicate that the POEM-*b*-PBMA/VO_x/CB films are limited in part by the ionic conductivity of the solid polymer electrolyte. Some improvement in capacity was seen with the acidification of the carbon black before incorporation into these films, but there was also a loss in capacity with cycling. To investigate the rate capability of the nanostructured architecture offered by microphase separating polymers, the POEM-*b*-PBMA/VO_x/CB films were cycled with LP50 liquid electrolyte and compared to conventional composite cathode (CCC) films. The data from these cycling experiments are shown in Figure 5-27. The open shapes correspond to the polymer cathode film while the closed shapes are for CCC films synthesized as described in Chapter 3. The area and ratio of active material to carbon black for each cathode were held constant for each of the cathodes cycled; however, the ~ 5 - 10 μm thickness of the CCC films is lower than that of the ~50 - 100 μm POEM-*b*-PBMA/VO_x/CB films. The capacity of the liquid electrolyte batteries was improved over that of the solid electrolyte, as seen in Figure 5-24. Although the CCC begins with a higher capacity at the lower current rate of C/10, the polymer film demonstrates superior behavior over the CCC at the higher rate of C/1.3. At current rates of C/1.3 the nanostructured cathode maintains

85% of the capacity obtained at $C/10$, while the CCC maintains approximately 55% of the capacity realized at $C/10$. When examined in comparison this provides an indication of the improved rate capability of the polymer-directed nanostructure.

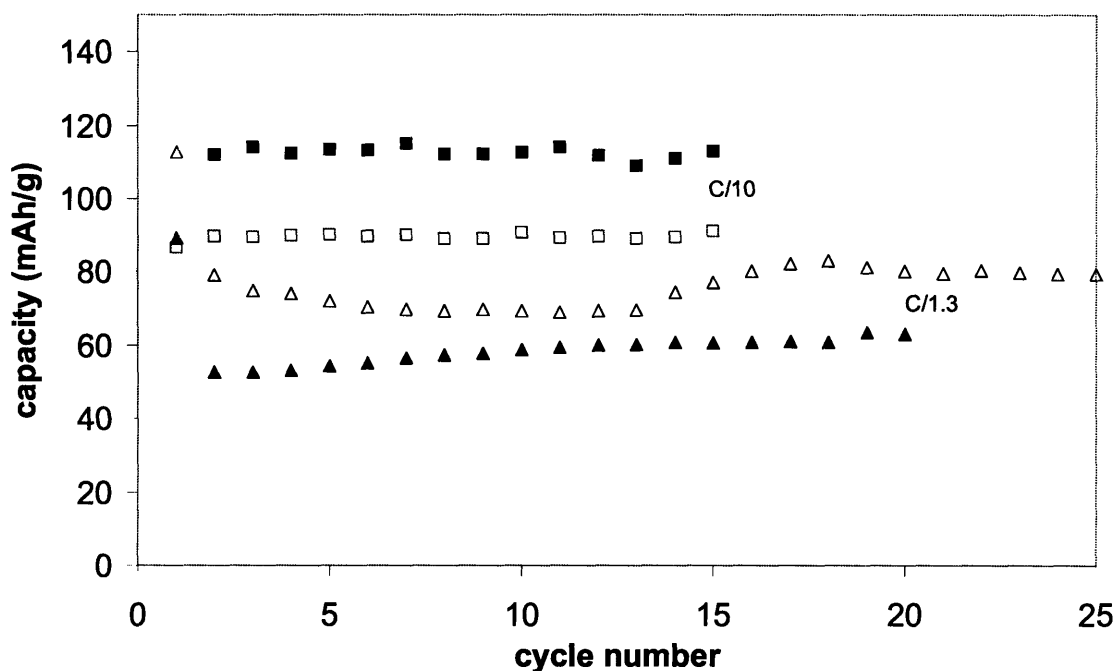


Figure 5-27: Cycling data as a function of current using liquid electrolyte. Open shapes are for the freestanding POEM-*b*-PBMA/ VO_x /CB (acid-treated) cathode and filled shapes are for a CCC control.

Carbon black was an effective conductivity additive that allowed the system to be probed electrochemically. An all solid-state battery containing nanocomposite vanadium oxide structure directed within POEM-*b*-PBMA was cycled reversibly using CB and lithium salt added in situ during the sol-gel processing steps. The performance of the solid-state battery was limited by the solid polymer electrolyte, not the electronic conductivity, as using liquid electrolyte improved the capacity of the cell and the capacity decreased with increased solid electrolyte thickness. Increased weight percentages of CB did not improve the capacity (not shown). In addition, attempts were made to use CB with a smaller average particle size (~ 10 nm, Black Pearls 2000); however these particles did not improve the capacity.

Summary

This chapter examined the following questions:

1. Can the POEM-*b*-PBMA/VO_x materials be used as cathodes? What electronic conductivity additives are necessary to make them usable?
2. Do these nanocomposite structures offer an improvement to a particular set of battery metrics, e.g. rate capability?

These materials can be used as cathodes, but not without an electronic conductivity additive. This chapter described several additives to improve electronic conductivity. The challenge comes in directing the electronic conductor to the same film regions as the POEM and VO_x, while retaining access to the transition metal oxide. The electronic wiring harness must provide a continuous pathway for electrons to the TMO phase to access its full capacity.

The use of silver salt also improved electronic conductivity and enabled cycling of thin 1-3 μm films cast on aluminum foil giving a first discharge capacity of 130 mAh/g. The limitation of the silver-containing films was that because of the high mass density of silver, a high weight fraction (~30 wt%) was required for cycling and freestanding films exhibited negligible capacity.

PEDOT also demonstrated the ability to act as an electron-conducting additive for these films. The advantage of PEDOT was that it could be deposited in direct contact with the vanadium oxide on the size scale of the polymer domain; however, it exhibited poor cyclability and 20 wt % was necessary for cycling. The electrodeposition of PEDOT onto films of vanadium oxide, including sputtered vanadium oxide and composite films cast on ITO and wire mesh, was also demonstrated.

The use of carbon black as a conductivity additive resulted in ~ 0.1 mm freestanding, flexible POEM-*b*-PBMA/VO_x/CB films that were cycled in an all solid-state battery configuration (using lithium foil as an anode) showing reversible capacities of ~40 mAh/g for several cycles. Acidification of the carbon black showed good improvement in capacity with the first several discharges; however, this capacity

decreased upon cycling. Although the carbon was not templated along the POEM domain, it percolated throughout the film as shown from the TEM micrograph and the impedance analysis of those films. Because of the successful solid-state battery cycling, the use of carbon black allowed for electrochemical probing of the system limitations. The performance of this system was limited by ionic conductivity through the electrolyte, as shown by the increased capacity using liquid electrolyte and the dependence on thickness of the solid electrolyte. In addition, the use of carbon black resulted in some improved rate capability over that of a composite cathode containing the same weight percentage VO_x and carbon black. This demonstrates the benefits of the nanostructured cathode, despite the scale of the carbon black particles. The use of carbon black enabled the access of capacity from vanadium oxide within the POEM-*b*-PBMA/VO_x composite films.

Table 5-2 shows the conductivities determined by impedance spectroscopy for the POEM-*b*-PBMA/VO_x composite films containing different electronic conductivity additives.

Table 5-2: Conductivity values for various electronic conductivity additives.

	σ (S/cm)
Ag	5×10^{-6}
PEDOT	$2.7 \times 10^{-6} - 9 \times 10^{-7}$
CB	10^{-5}

This chapter has shown improved rate capability in the POEM-*b*-PBMA/VO_x films containing carbon black and the ability to cycle all solid-state batteries with improved interface between the cathode and electrolyte. Beyond these improvements, the answer to the second question will be examined further in the next chapter.

References

1. Long, J. W., Dunn, B., Rolison, D. R. & White, H. S. "Three-Dimensional Battery Architectures." *Chemical Reviews*, **2004**, 104, 4463-4492.
2. Ramasay, R. P., Feger, C., Strange, T. & Popov, B. N. "Discharge Characteristics of Silver Vanadium Oxide Cathodes." *Journal of Applied Electrochemistry*, **2006**, 36, 487-497.
3. Takeuchi, K. J., Marschilok, A. C., Davis, S. M., Leising, R. A. & Takeuchi, E. S. "Silver vanadium oxides and related battery applications." *Coordination Chemistry Reviews*, **2001**, 219-221, 283-310.
4. Huang, F., Fu, Z.-w. & Qin, Q.-Z. "A novel Li₂Ag_{0.5}V₂O₅ composite film cathode for all-solid-state lithium batteries." *Electrochemistry Communications*, **2003**, 5, 262-266.
5. Hwang, H. S. et al. "Characterization of Ag-doped vanadium oxide (Ag_xV₂O₅) thin film for cathode of thin film battery." *Electrochimica Acta*, **2004**, 50, 485-489.
6. Xie, J., Li, J., Dai, Z., Zhan, H. & Zhou, Y. "Ultrasonic sol-gel synthesis of Ag₂V₄O₁₁ from V₂O₅ gel." *Journal of Materials Science*, **2004**, 39, 2565-2567.
7. West, K. & Crespi, A. M. "Lithium insertion into silver vanadium oxide Ag₂V₄O₁₁." *Journal of Power Sources*, **1995**, 54, 334-337.
8. Kawakita, J., Sasaki, H., Eguchi, M., Miura, T. & Kishi, T. "Characteristics of delta-Ag_yV₂O₅ as a lithium insertion host." *Journal of Power Sources*, **1998**, 70, 28-33.
9. Kwon, C.-W. et al. "Poly(3,4-ethylenedioxythiophene)V₂O₅ hybrids for lithium batteries." *Electrochemistry Communications*, **2002**, 4, 384-387.
10. Sonmez, G., Schottland, P. & Reynolds, J. R. "PEDOT/PAMPS: An electrically conductive polymer composite with electrochromic and cation exchange properties." *Synthetic Metals*, **2005**, 155, 130-137.
11. Arbizzani, C., Mastragostino, M. & Rossi, M. "Preparation and Electrochemical Characterization of a polymer Li_{1.01}Mn_{1.97}O₄/pEDOT Composite Electrode." *Electrochemistry Communications*, **2002**, 4, 545-549.

12. Lock, J. P., Im, S. G. & Gleason, K. K. "Oxidative Chemical Vapor Deposition of Electrically Conducting Poly(3,4-ethylenedioxythiophene) Films." *Macromolecules*, **2006**, 39, 5326-5329.
13. Skotheim, T. A., Elsenbaumer, R. L. & Reynolds, J. R. *Handbook of Conducting Polymers* M Dekker: New York, 1998.
14. Mui, S. C. PhD thesis in *Materials Science and Engineering*. "Electrochemical Kinetics of Thin Film Vanadium Pentoxide Cathodes for Lithium Batteries." 2005.
15. Im, S. G., Olivetti, E. A. & Gleason, K. K. "Doping Level and Work Function Control in Oxidative Chemical Vapor Deposited PEDOT." *Applied Physics Letters*, **2007**, accepted.
16. Lim, J. Y., Ko, H. C. & Lee, H. "Systematic Prediction of Maximum Electrochromic Contrast of an Electrochromic Material." *Synthetic Metals*, **2005**, 155, 595-598.
17. Lapkowski, M. & Pron, A. "Electrochemical oxidation of poly(3,4-ethylenedioxythiophene)- "in situ" conductivity and spectroscopic investigations." *Synthetic Metals*, **2000**, 110, 79-83.
18. Trapa, P. E. et al. "Rubbery Graft Copolymer Electrolytes for Solid-State, Thin-film Lithium Batteries." *Journal of the Electrochemical Society*, **2005**, 152, A1-A5.
19. Livage, J. "Sol-gel chemistry and electrochemical properties of vanadium oxide gels." *Solid State Ionics*, **1996**, 86-88, 935-942.
20. Guerra, E. M., Ciuffi, K. J. & Oliveira, H. P. "V₂O₅ xerogel-poly(ethylene oxide) hybrid material: Synthesis, characterization, and electrochemical properties." *Journal of Solid State Chemistry*, **2006**, 179, 3814-3823.

Chapter 6 : Benefits of Templated Architecture

In the previous chapter, a composite material made by structure-directing vanadium oxide growth within the ion-conducting domain of the block copolymer POEM-*b*-PBMA, was further modified through the addition of electronically conducting components. The resulting films demonstrated improved performance at a $C/1.3$ discharge rate of analogous traditional, mixed-powder composite cathodes when cycled with liquid electrolyte. Addition of nanoscale carbon black further enabled cycling of the composite film using a solid polymer electrolyte and lithium foil anode in an all-solid-state, mechanically flexible battery. Based on the cycling data obtained by changing the thickness of the electrolyte, the battery performance was determined to be limited by the electrolyte's conductivity.

This chapter discusses removal of the copolymer after the *in situ* growth of vanadium oxide to examine in detail the resulting structure of the inorganic phase. The chapter documents the resulting material (after polymer removal under various atmospheres) and investigates the potential benefits of this architecture. It also provides some analysis of the diffusion lengths allowed by the smaller length scales and discusses the validity of the assumption of mass-transport limitations.

This chapter examines the fundamental question:

Does the nanostructure created by templating with microphase-separating copolymers offer an improvement to a particular set of battery metrics, e.g. rate capability?

More specifically, this chapter describes removal of the polymer under a variety of atmospheres, and characterizes the resulting vanadium oxide microstructure. Once the polymer is removed we can examine the relevant diffusion length scales provided by the architecture and provide justification for the mass-transport-limitation assumptions inherent in attempts to improve surface-area-to-volume ratios.

A Word about Taxonomy

In a typical templated structure, as in the work described by Patrisi and Martin,[1] the track-etched polycarbonate or porous alumina template is removed after it has been filled by the material synthesized therein. For example, after synthesizing vanadium oxide nanofibers from $\text{VO}(\text{O}^i\text{Pr})_3$, Sides *et al.* removed the polycarbonate template (that enabled the nanofiber morphology) by an oxygen plasma treatment.[2] Template removal is also accomplished through post-pyrolysis or dissolution of the membrane by aqueous acids or bases.[3] In the present study, the cathode-active material has been synthesized within the POEM domains of a copolymer, which remains part of the composite film. Li^+ ion conduction occurs within the POEM domains, while the copolymer matrix confers mechanical flexibility on the composite film. Therefore, this thesis has avoided the use of the word “template” in Chapters 4 and 5, as this term usually denotes a structure-directing component that is removed after the synthesis of the active material. In this chapter, however, the polymer will be removed; leaving behind the nanostructured vanadium oxide, herein termed ***templated*** vanadium oxide or VO_x .

Removing the Template

Composite films of POEM-*b*-PBMA and vanadium oxide were synthesized as described in Chapter 3. A control film of sol-gel derived vanadium oxide without the polymer was also synthesized. After both films had dried under vacuum overnight at 80°C , they were heated at 400°C under an atmosphere of argon gas removing the polymer, as confirmed by SEM. This temperature was above the onset of crystallization for vanadium oxide at 200°C (stable orthorhombic structure heating $> 350^\circ\text{C}$).[4, 5] Figure 6-1a and b are SEM micrographs depicting the microstructure of the templated VO_x . The resulting architecture has porosity on the order of the polymer domain spacing, ~ 30 nm. Figure 6-1a shows the cross section of the film while Figure 6-1b shows the surface of the film.

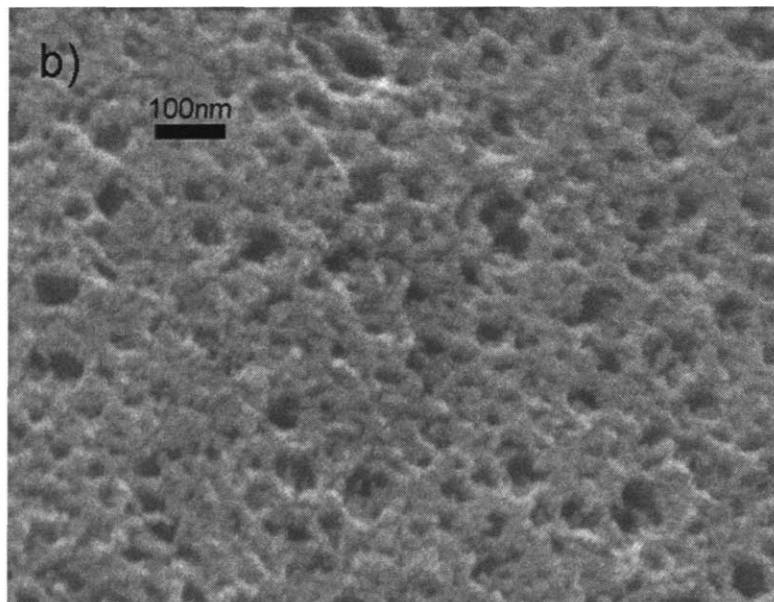
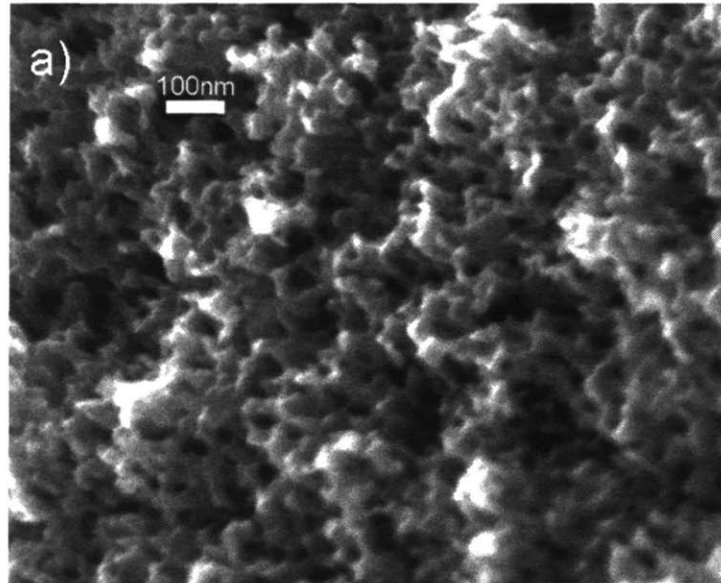


Figure 6-1: SEM micrograph of templated sol-gel vanadium oxide synthesized within POEM-*b*-PBMA after polymer removal under Ar at 400°C. a) cross section b) surface of the film.

The SEM micrograph in Figure 6-2 depicts the microstructure of vanadium oxide made through sol-gel chemistry without the polymer template (non-templated) and shows large, featureless micron-sized discs.

The surface area of the templated material was $\sim 200 \text{ m}^2/\text{g}$ using BET techniques, while the non-templated material had a surface area $\sim 20 \text{ m}^2/\text{g}$.

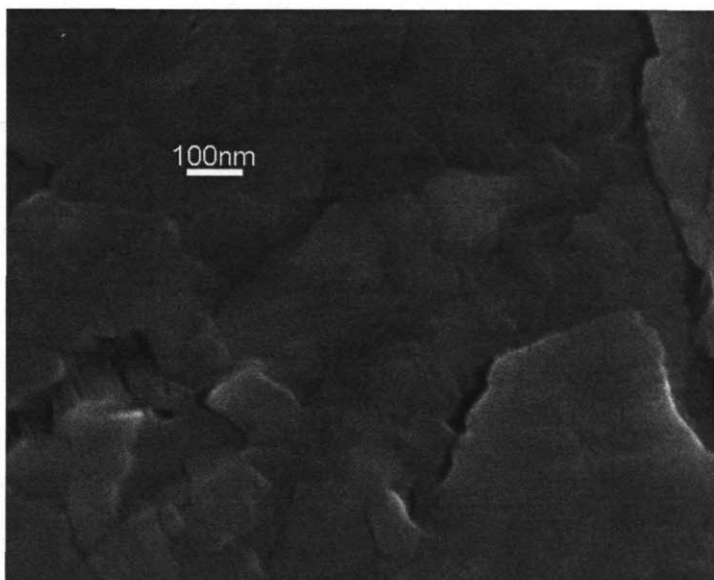


Figure 6-2: Non-templated sol-gel derived vanadium oxide synthesized and cast without polymer.

Under TEM, the templated VO_x particle size can be further examined (Figure 6-3 and Figure 6-4). The film shown was heated to 600°C under nitrogen for 1 hour and subsequently crushed with a mortar and pestle before dispersing on carbon-coated TEM grids. The continuous templated structure observed in Figure 6-1 is not seen as clearly in Figure 6-3, but particles of ~ 10 nm are apparent and the lattice fringes of crystalline vanadium oxide are visible in the higher magnification micrograph found in Figure 6-4.

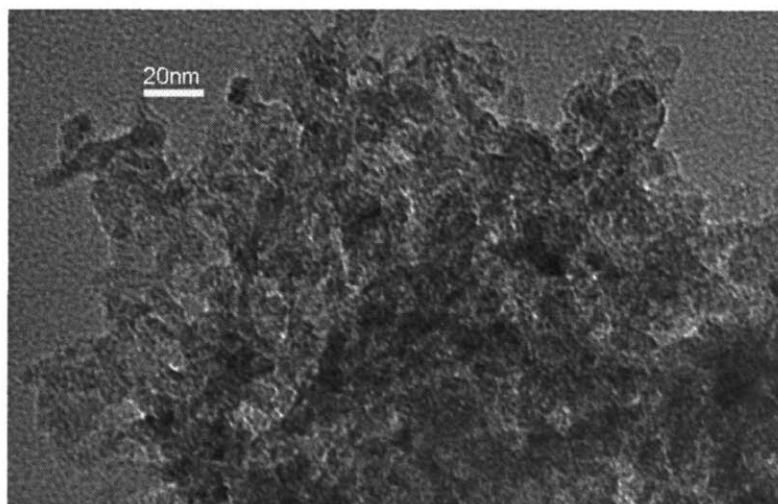


Figure 6-3: TEM micrograph of templated vanadium oxide heated to 600°C under argon and crushed.

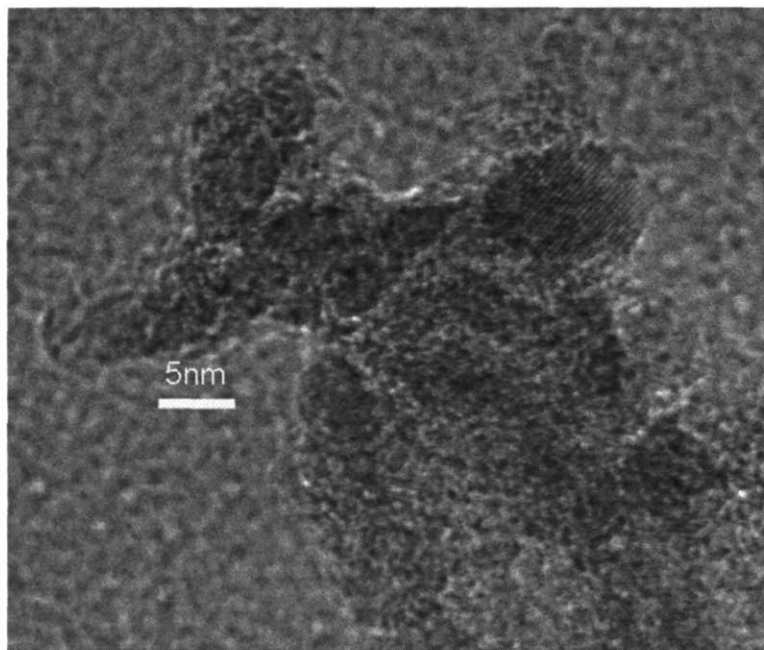


Figure 6-4: Higher magnification TEM micrograph of templated VO_x particles.

These images verify that, upon removal of the polymer under inert atmosphere, the increased surface-area-to-volume ratio nanostructure is preserved, even when the sample is mechanically ground. WAXS shown in Figure 6-5 verifies that the orthorhombic structure of crystalline vanadium oxide is formed upon heating to 400°C. The peaks shown match that of V₂O₅ (PDF #41-1426) as seen from the lines plotted below the experimental data³.

³ Powder Diffraction Standards File No. 41-1426

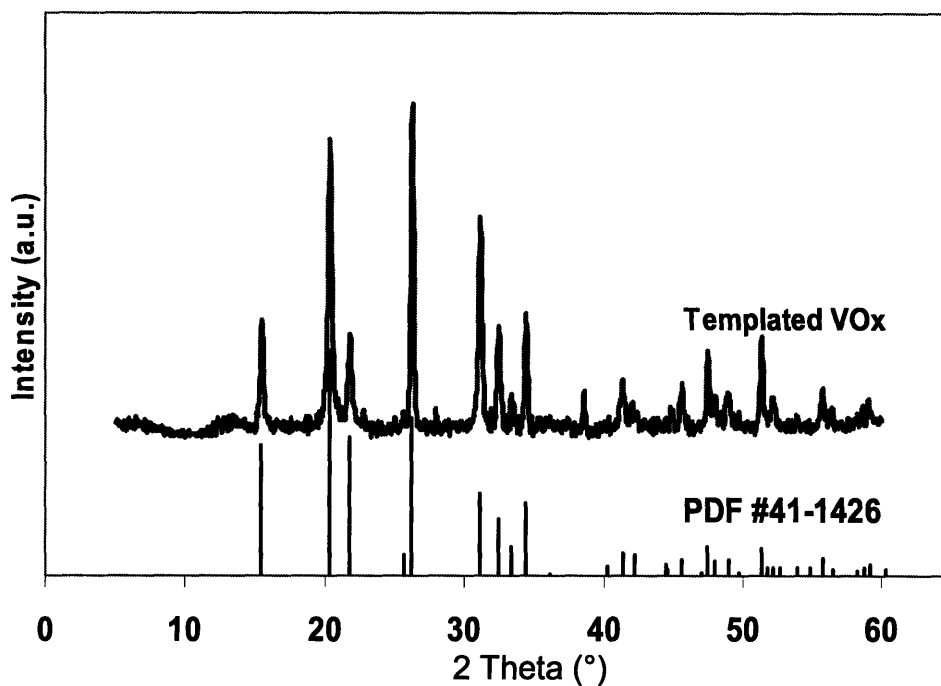


Figure 6-5: WAXS for sol-gel derived vanadium oxide heated at 400°C.

Template Removal: Changing the Atmosphere

A potential benefit of template removal would be the partial conversion of the polymer template to graphitic carbon in the removal process. This would improve electronic conductivity and may eliminate the need for a conductivity additive. As was mentioned in Chapter 2, this has been illustrated in vanadium oxide by the work of Odani *et al.* and recently in the olivine-structured LiFePO_4 systems by Scrosati *et al.*[6, 7] In cathodes of the vanadium oxide system, unlike those of lithium iron phosphate, there is a dilemma between preserving graphitized carbon and avoiding reduction of the V_2O_5 to less desirable oxides such as VO_2 and V_2O_3 , thereby affecting the crystal structure and electronic conductivity, leading to reduced capacity.[4] In addition, as suggested by Swider-Lyons *et al.*, heat treatments under various atmospheres may introduce different vacancies changing the electrochemical performance.[8]

Therefore, to prepare V_2O_5 an additional oxidation step is needed. Heating in oxidizing conditions also means the carbon will be combusted, so, as Odani indicated,

heating steps need to be optimized for conversion of V^{4+} to V^{5+} while still leaving some carbon on the particles.[6] However, according to the Ellingham diagram shown below in Figure 6-6, the conversion of carbon to carbon dioxide will occur before the oxidation of V^{4+} to V^{5+} .

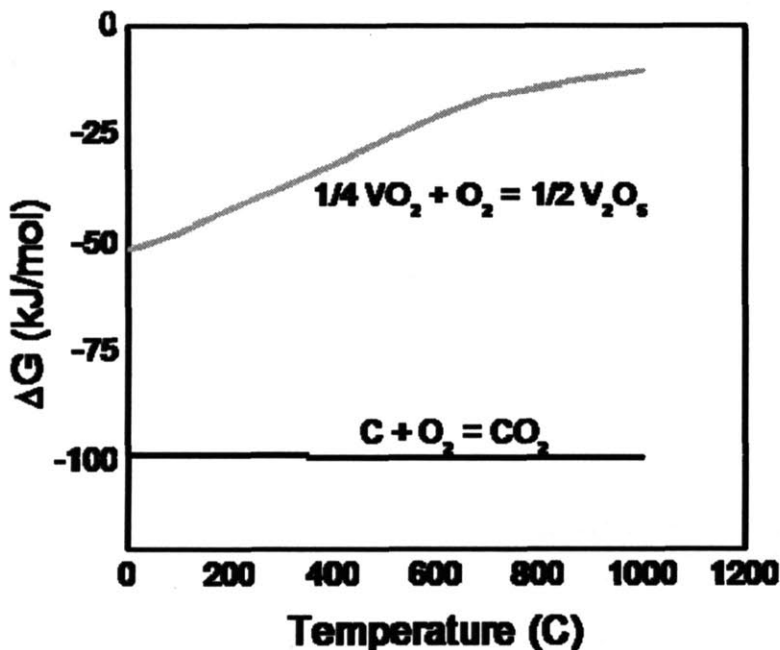


Figure 6-6: Ellingham diagram for vanadium oxide and carbon dioxide (graph produced using HSC Chemistry software).

To attempt to convert the polymer template to a conducting carbon phase, several POEM-*b*-PBMA/ VO_x films from the same synthesis batch were subjected to various heat treatments, XPS was used to determine the valence of the vanadium after each treatment.

Non-templated, for reference

The high resolution XPS V2p spectrum for non-templated vanadium oxide from sol-gel is shown in Figure 6-7 for comparison. The valence for vanadium in the oxide is primarily V^{5+} , shown at binding energies of 518 eV ($2p_{3/2}$) and 525.5 eV ($2p_{1/2}$). The XPS data are consistent with the published spectrum for V_2O_5 . [9].

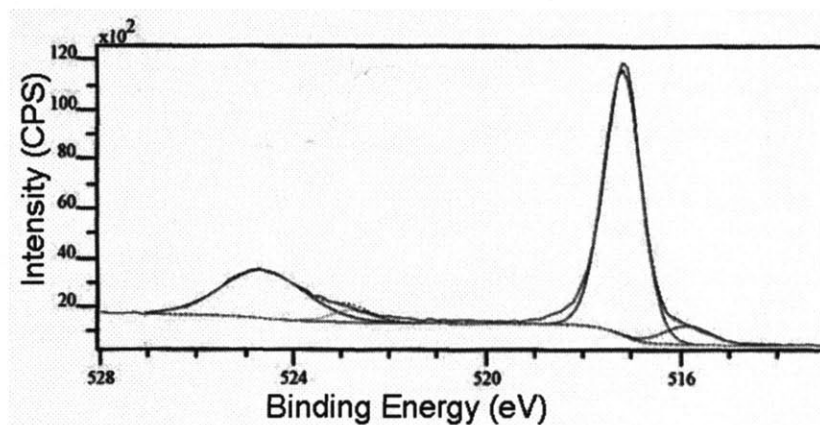


Figure 6-7: XPS V2p spectrum of sol-gel derived, non-templated vanadium oxide.

Also for reference, a TEM micrograph, shown in Figure 6-8, depicts micron-sized particles of sol-gel derived, non-templated vanadium oxide that have been mechanically ground for use in the composite cathodes.

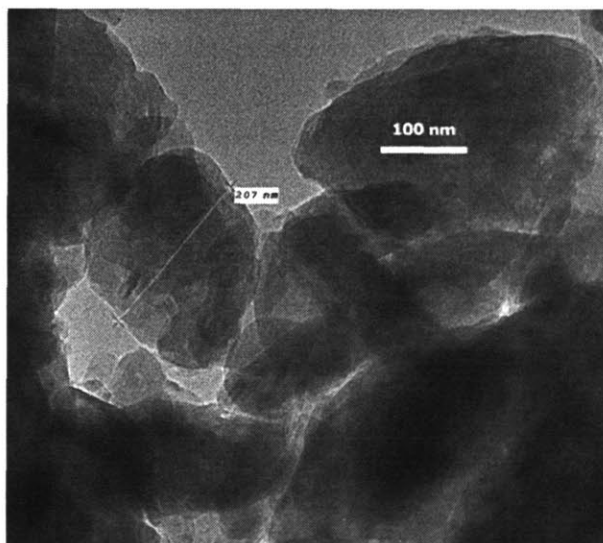


Figure 6-8: TEM micrograph of sol-gel derived, non-templated vanadium oxide mechanically ground for use in cathode.

Templated

The high resolution XPS V2p spectrum for a templated film heated under argon at 400°C (herein denoted VO_x(Ar)), is shown in Figure 6-9. The heating protocol for this sample involved ramping up to 400°C at 3° per minute followed by a dwell step for 1.5 h.

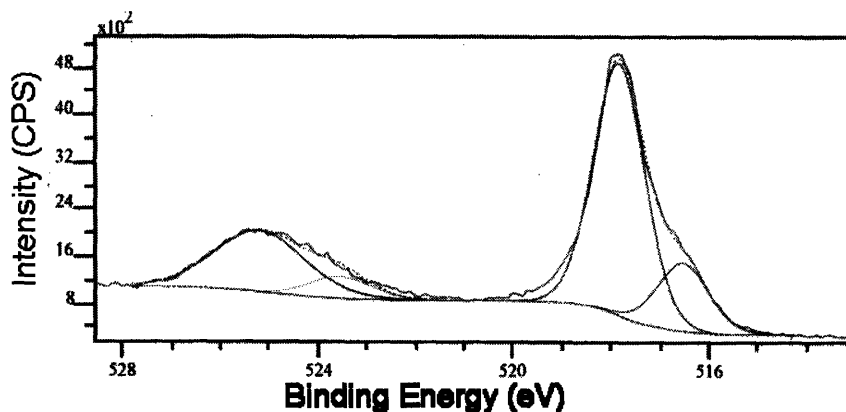


Figure 6-9: XPS V2p spectrum of sol-gel derived, templated vanadium oxide, heated to 400°C under flowing argon (VO_x(Ar)).

This can be compared to the spectrum from a sample of film from the same batch that was heated under air (herein denoted VO_x(Air)) following the same heating protocol to remove the polymer template. The XPS V2p spectrum for this sample is shown in Figure 6-10 and indicates that the VO_x(Air) film is dominated by V⁵⁺ states. The VO_x(Ar) film has a higher percentage of vanadium in the 4+ state, as evidenced by the larger shoulders at lower binding energy. From the relative intensities of the V⁴⁺ and V⁵⁺ contributions, ~73% of the vanadium is in a 5+ state when film is heated under argon versus ~92% when heated in air.

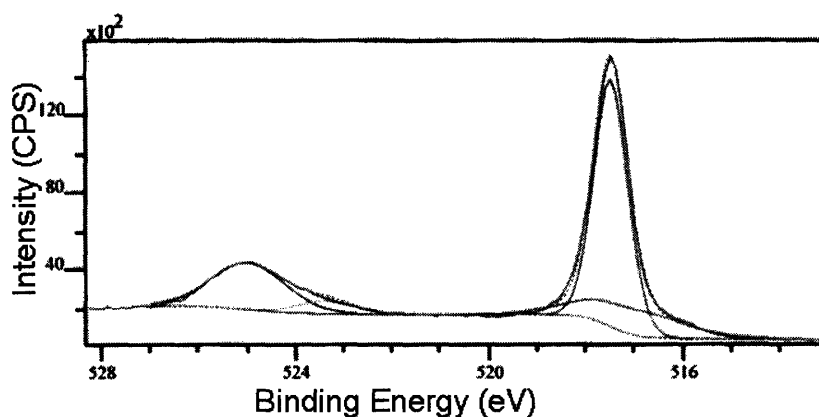


Figure 6-10: XPS V2p spectrum of sol-gel derived, templated vanadium oxide, heated to 400°C under air (VO_x(Air)).

Heating the composite in air for long times (>1 h) to remove the polymer template also resulted in particle coarsening from ca. 10 nm to 60 nm as shown in the TEM micrograph in Figure 6-11. This process did not occur in the systems heated under inert conditions. These particles are still smaller than micron-sized particles seen in the non-templated micrograph in Figure 6-8.

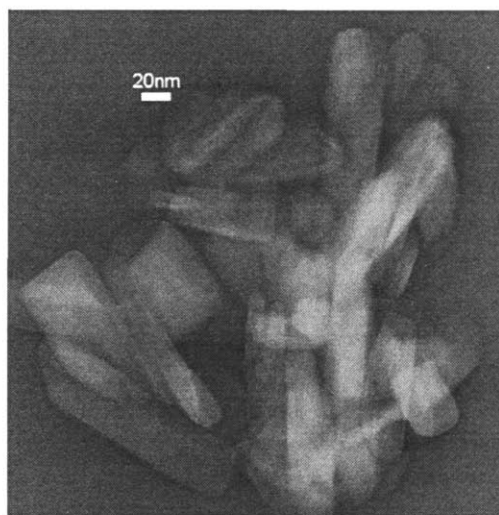


Figure 6-11: TEM micrograph of sol-gel derived, templated VO_x heated to 400°C in air (VO_x(Air)).

To attempt to partially retain the graphitized carbon formed in the Ar environment while decreasing the percentage of 4+ vanadium, the VO_x(Ar) sample was subsequently heated in air up to 400°C at 2° per min to oxidize the vanadium (sample herein denoted VO_x(Ar/Air)). Upon reaching the target temperature, the film was immediately removed from the heat to limit oxidation of the carbon and extensive sintering of the vanadium oxide particles. This technique was followed by Odani *et al.*[6] and confirmed by email communication with Dr. Vilas Pol of the Odani research group.[10] The XPS spectrum for this sample is shown in Figure 6-12 and a TEM micrograph of the resulting morphology is shown in Figure 6-13.

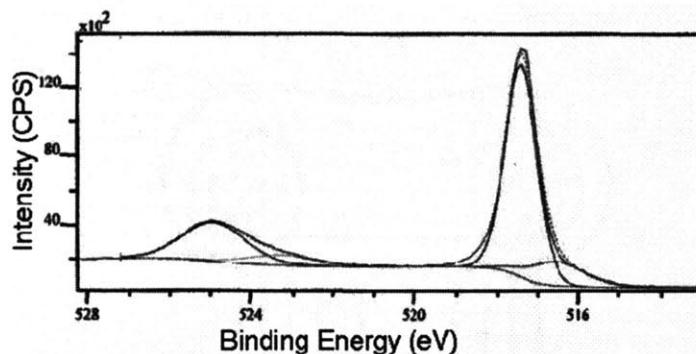


Figure 6-12: XPS spectrum of VO_x heated first in argon at 400°C, then second heating step in air to 400°C (VO_x(Ar/Air)) (rapid cool).

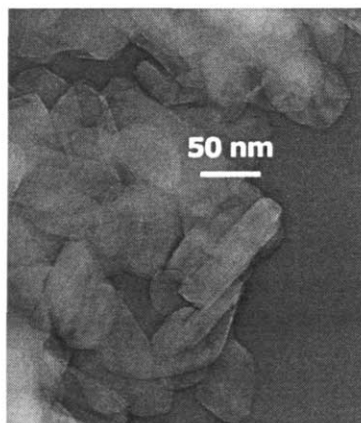


Figure 6-13: TEM micrograph of sol-gel derived, templated VO_x (VO_x(Ar/Air)) heated at 400°C in argon, then second heating step in air to 400°C (rapid cool).

The XPS spectrum indicates that the vanadium was oxidized to primarily V⁵⁺. Results of elemental analysis to determine the amount of carbon present in the film shown in Figure 6-12 are presented in Table 6-1, along with other information about the particles under different atmospheres.

Table 6-1: Elemental analysis on VO_x films with polymer removed under different atmospheres.

Sample	%C	%H	% V ⁵⁺ (XPS)	Particle size (ca.)
VO _x (Ar) : Figure 6-9	12.38	1.11	73	10 nm
VO _x (Air) : Figure 6-10 and 6-9	0.1	<0.1	92	40 - 60 nm
VO _x (Ar/Air): Figure 6-12	0.13	<0.1	85	40 - 60 nm

The majority of carbon was eliminated in the oxidation step and so the results of this work differ from those reported by the Odani group. Based on the above analysis, carbon was not preserved in the heating treatments and therefore, electronic additives were necessary to measure the electrochemical properties of the templated vanadium oxide. Removing the polymer also results in a brittle vanadium oxide material requiring repotting with a polymeric binder and casting as a composite cathode film.

Before presenting data on cycling the nanostructured vanadium oxide, the next section provides a brief analysis of the diffusion lengths and a discussion on the mass transport limitation assumption.

Calculating Potential Benefits of Architecture

The distance of Li^+ ion diffusion is set by the dimension of the vanadium oxide fiber, or particle. The architecture provided through the template process with vanadium oxide dimensions between 10 and 30 nm will result in a large active area over which Li^+ can intercalate. Considering the specific particle sizes that have been observed in the TEM micrographs in this chapter, the surface-area-to-volume ratio for spherical particles of sizes 10, 50, 200 nm are, respectively, 0.6, 0.12, 0.03 nm^{-1} .

However, using spherical particle geometry does not account for the bicontinuous structure seen in the SEM micrographs seen in Figure 6-1 and Figure 6-2 or the cylindrical morphology of the pristine POEM-*b*-PBMA copolymer. The surface-area-to-volume ratio for cylinders of 35 nm and 500 nm are, respectively, 0.13 and 0.028 nm^{-1} . Previous work by Anderson and Thomas has modeled polymer morphologies and determined a range of dimensionless surface areas as a function of polymer volume fraction for bicontinuous morphologies.[11, 12] For the volume fraction of POEM used in this work, the normalized surface area (SA) for dividing surfaces of the single-diamond family was between 3.5 and 4.5.[11] Using the SAXS domain spacing as a unit cell lattice parameter, the expected range in surface-area-to-volume ratio was calculated as 0.09-0.12 nm^{-1} . An estimate for the surface-area-to-volume ratio based on the measured BET values of 200 m^2/g and 20 m^2/g , respectively, for the templated and non-templated vanadium oxide can be made assuming the value 3.36 g/cm^3 for the density of vanadium oxide. For the non-templated and templated sol-gel derived vanadium oxide

the surface-area-to-volume ratios from BET measurements are 0.067 and 0.67 nm⁻¹, respectively. Table 6-2 summarizes the results of these surface-area-to-volume ratio calculations and estimates.

Table 6-2: Surface area: volume comparing templated and non-templated vanadium oxide microstructures determined by several techniques (units = nm⁻¹)

	Geometric estimates (cylinders)	From BET measurement	Modeled normalized SA[11]
Non-templated	0.028	0.067	-
Templated	0.13	0.67	0.12

The BET measured surface-area-to-volume ratio was substantially higher than values calculated based on the template geometry. One explanation for this might be the fine structure of the vanadium oxide, which exists at a smaller lengthscale than the template periodicity, increasing the true surface area. Moreover, the vanadium oxide does not fill the volume of the POEM domain in the block copolymer. A higher ratio would be expected from the vanadium oxide measured using BET than is estimated from the polymer morphology, as it has increased surface area within the POEM domain.

Further analysis can determine the current at which increased rate will result in a reduction in capacity at a given size scale. Altering the dimension over which Li⁺ will diffuse in the electrode will alter the diffusion penetration time as L²/D (where D is the diffusion coefficient and L is the electrode thickness). Looking at the two length scales mentioned for vanadium oxide in this chapter, 10 - 50 nm for the nanoarchitecture and 500 nm - 1 μm for commercially available vanadium oxide powders, the characteristic diffusion time will range from 5 - 45 seconds and 3 - 14 hours, respectively; assuming a diffusion coefficient of Li⁺ in V₂O₅ of 2 × 10⁻¹³ cm²/s.[13] This calculation implies that the diffusion time of Li⁺ through micron-sized particles of V₂O₅ should manifest at current rates of ~C/8.5 (average between 3 and 14). The next section will provide a discussion on mass transport limitations in the system and give experimental evidence of this rate limitation.

Mass Transport

The increased surface-area-to-volume ratio offered by these architectures will be most beneficial in situations of mass-transfer limitation. A system gated electronically, by some interfacial step, or by transport in the electrolyte may not be improved by the nanoarchitecture described in this work. Previous work has shown that at high discharge rates the effect of increased surface-area-to-volume ratio is seen, while at lower discharge rates performance is invariant with change in particle size.[14] However, previous work done in this group has shown that at higher current rates, factors other than mass transport of ions within the intercalation host may also become limiting. These factors may include electronic conductivity or, for the case of crystalline systems, the phase transformation (as lithiation occurs) may become the rate limiting step.[15] Mui found that thin films of sputtered vanadium oxide were Li^+ diffusion controlled (mass transfer) at low current rates (as a dependence on film thickness was observed), while at high current rates kinetic processes such as charge transfer became limiting (performance no longer scaled with thickness).[15] Phase transformation may also induce rate limitations correlated with lattice strain within the particles undergoing transformation.[16]

Mass transport limitations can be manifest in this system as a result of decreased performance upon rate increase. This decrease in performance with increased current rate is shown in Figure 6-14, depicting discharge profiles of a model vanadium oxide cathode at various C-rates cycled from 2.5 V – 3.5 V. The model cathodes used for this cycling data were prepared from commercially available vanadium oxide powder combined with carbon black and PVDF binder. These materials were mixed together along with NMP and the slurry was cast onto aluminum foil as a conventional composite cathode (CCC). The cells were run with liquid electrolyte with a lithium anode.

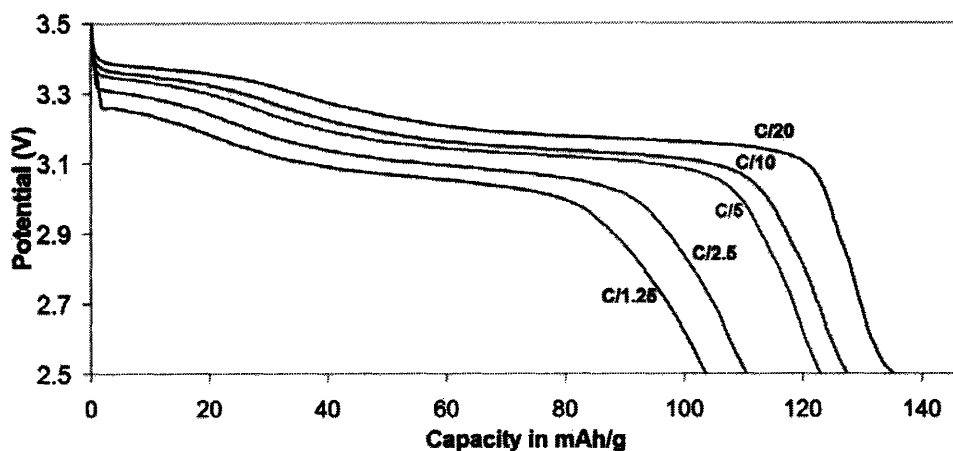


Figure 6-14: V_2O_5 composite cathode cycled at different rates with liquid electrolyte. Cycling data provided by graduate researcher, Kenneth Avery.

The effect of increased rate leading to decreased capacity is seen as the capacity of the cell at C/5 is reduced by 10% from the capacity at C/20 (from 135 mAh/g to 122 mAh/g).

Cycling Data for Templated VO_x

In order to investigate the electrochemical performance of the templated vanadium oxide, two different CCC films were prepared. One with *templated* ($VO_x(\text{Ar}/\text{Air})$) and one with *non-templated* VO_x , with the same ratio of PVDF:CB: VO_x for both films. The results of several cycles discharged at C/5 (a rate at which decreased capacity was seen in the “model” cathode above) from 2.5 - 3.5 V with each cathode are shown in Figure 6-15. The cycling data (which was reproduced in four different cells and is averaged in Table 6-3) indicates a factor of improvement of 1.5 for the nanostructured film. Both cathode films were heated to 400°C before cycling to compare the cycling data more accurately. The crystallinity of the vanadium oxide is notable from the plateaus in the discharge profiles. For the templated structure the first discharge is 92% of theoretical while the non-templated cathode shows only 56% of theoretical capacity. Therefore, the templated, nanostructured cathodes appear to offer some rate improvement over their non-templated counterparts.

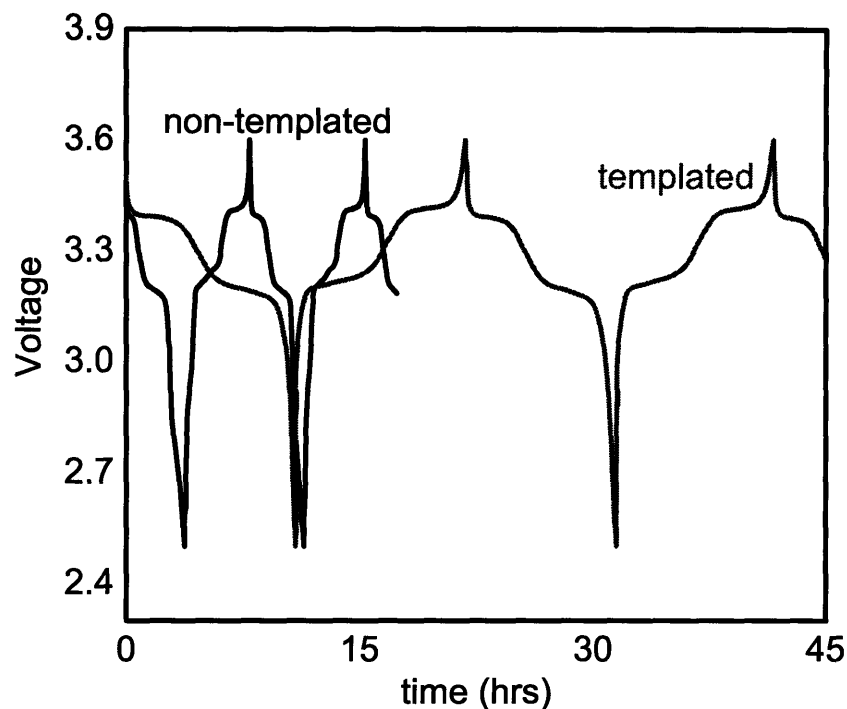


Figure 6-15: Discharge curves for templated ($\text{VO}_x(\text{ArAir})$) and non-templated VO_x at C/5.

Table 6-3: Capacity from templated and non-templated VO_x (average of 4 cells) at C/5.

Cycle	Capacity non-templated (mAh/g)	Capacity templated (mAh/g)
1	83 ± 5	135 ± 6
2	75 ± 4	120 ± 8
3	72 ± 7	110 ± 4

The decrease in capacity observed with further cycling is characteristic of crystalline vanadium oxide systems.

To further illustrate the improved rate performance of the templated films at high rates, the first discharge profiles for templated and non-templated cathodes were compared at 3C. The profiles comparing non-templated and templated samples are shown in Figure 6-16. The first discharge capacity at 3C for the templated cathodes is 96% of the capacity at C/10, while the non-templated cathode decreases by 58% from 147mAh/g at C/10 to only 86 mAh/g when cycled at 3C.

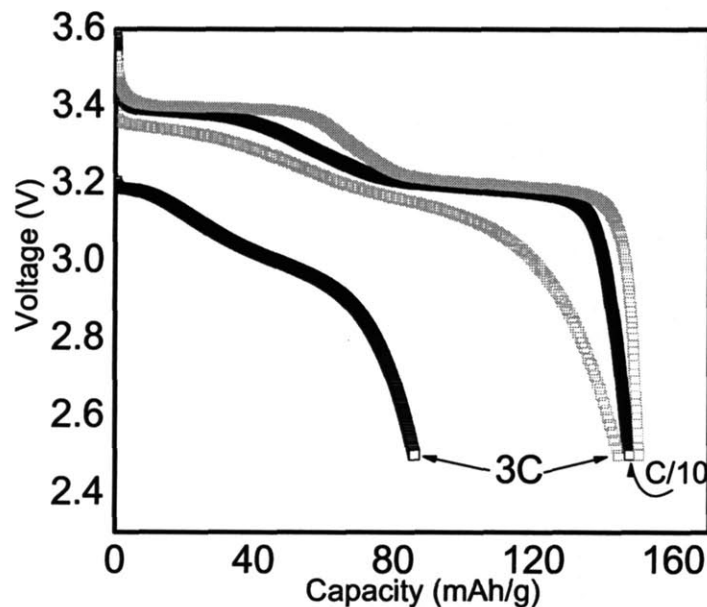


Figure 6-16: 1st discharge curves for templated ($\text{VO}_x(\text{ArAir})$) (green) vs. non-templated (black) conventional composite cathodes at C/10 and 3C.

Amorphous composite cathode films made with sol-gel vanadium oxide exhibited better cycle life, but for the purposes of comparison, data from the crystalline forms are shown here. In addition, composite cathodes made from the films heated only under argon ($\text{VO}_x(\text{Ar})$) with no additional oxidizing step were made into composite cathodes and exhibited decreased performance as compared to the $\text{VO}_x(\text{Ar}/\text{Air})$ films. This result may also have implications for the cycling ability of the films in Chapter 5, because as was shown in Chapter 4, some reduction of V^{5+} occurs during the *in situ* sol-gelation of vanadium oxide (Figure 4-14).

Discussion of Performance

Although an improvement in rate capability is observed in the templated vanadium oxide, the increase was not as dramatic as seen in the aerogel vanadium oxide produced by Dunn and coworkers or the templated version seen by Martin and coworkers.[1, 5] This section will discuss a potential way electronic conductivity may account for this difference.

A limitation arises in the preparation of the composite cathodes that may not effectively wire the vanadium oxide electronically. To illustrate this, SEM micrographs

comparing non-templated and templated cathodes are shown below. Graduate researcher Kenneth Avery performed this SEM. The first two micrographs, Figure 6-17 and Figure 6-18 are, respectively, low- and high-magnification images of the non-templated vanadium oxide composite cathodes. The smaller particles present are carbon black (example outlined with white circles in figure) and the large faceted species are the vanadium oxide particles (example outlined with green squares in figure). The smooth surface of the particles is similar to that of the vanadium oxide sol-gel film shown in Figure 6-2. From the higher magnification micrograph the particles can be sized at between ~ 500 nm and $1 \mu\text{m}$. It is also apparent from the composite cathode micrographs that these films are not uniform and that their performance will be affected by the contact between the carbon black and vanadium particles. This contact may alter upon cycling as well.

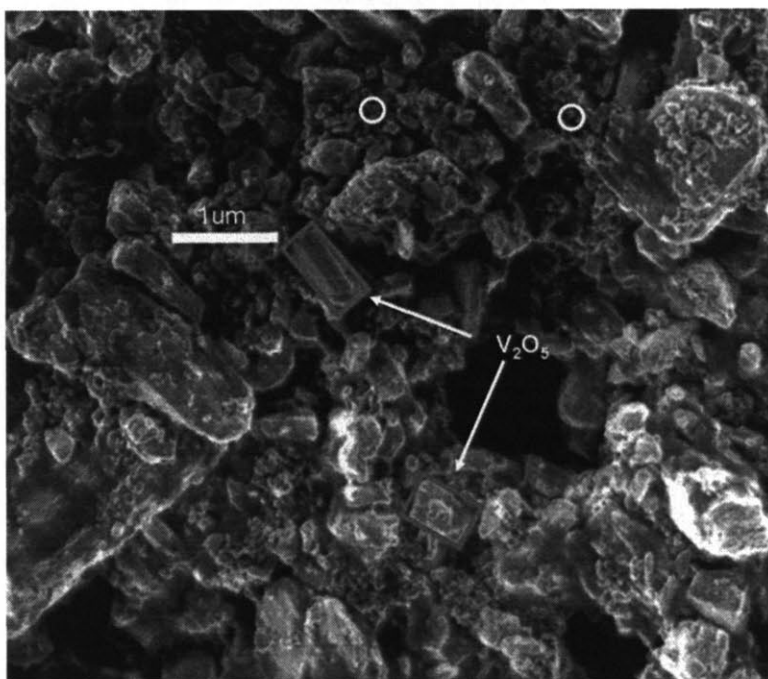


Figure 6-17: SEM micrograph of composite cathode made with non-templated vanadium oxide (green square). Carbon black also indicated by a white circle.

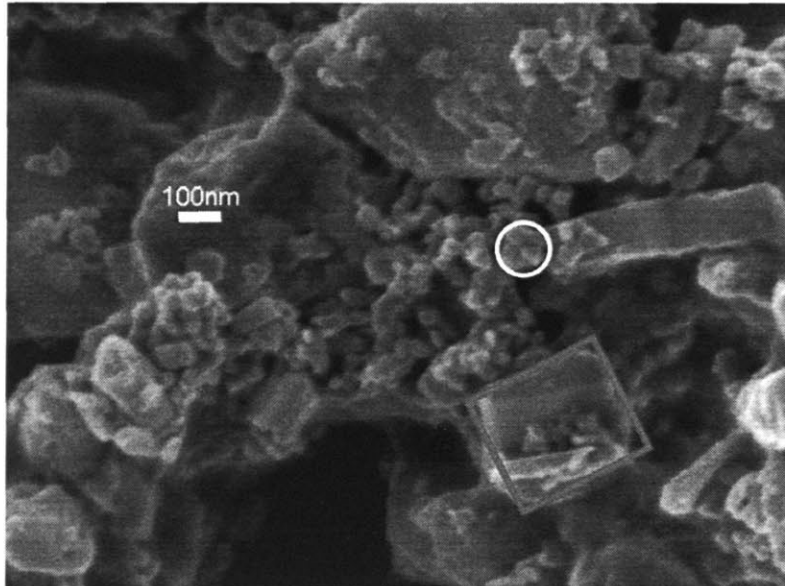


Figure 6-18: SEM micrograph of composite cathode made from non-templated vanadium oxide at higher magnification.

The next two SEM micrographs in Figure 6-19 and Figure 6-20 are from composite cathode films made with templated vanadium oxide. They are shown at similar magnifications to the images above. The first micrograph shows the same large particles of vanadium oxide (green outline) and smaller carbon black particles (white circle) serving as the electronically conducting additive. The micrograph at higher magnification, Figure 6-20, shows the detail of the particles whose morphology is similar to that seen in the templated VO_x alone (Figure 6-1).

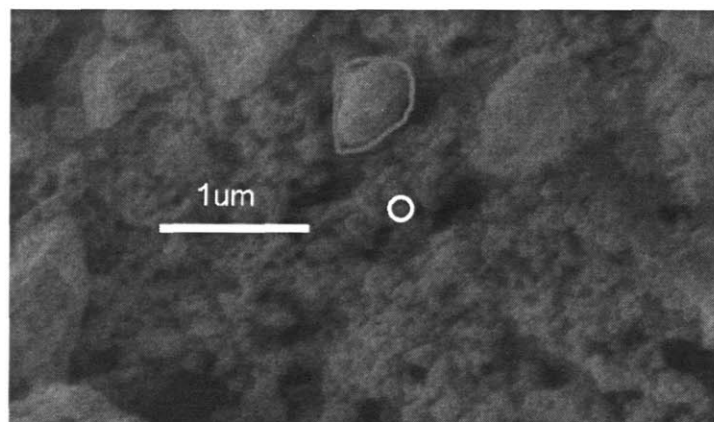


Figure 6-19: SEM micrograph of composite cathode made with templated ($\text{VO}_x(\text{Ar}/\text{Air})$) vanadium oxide (example has green outline). Example of carbon black also indicated with circle.

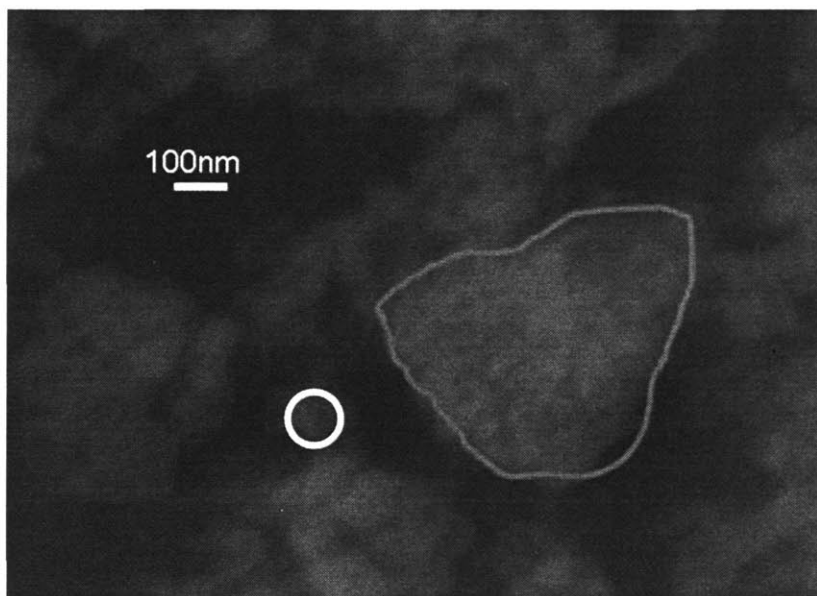


Figure 6-20: SEM micrograph of composite cathode made from templated ($\text{VO}_x(\text{Ar}/\text{Air})$) vanadium oxide at higher magnification.

It is apparent from these composite cathode images that the fabrication techniques used might not access the increased surface area structure because the larger particles (with the fine substructure) might not be in contact with the carbon black and therefore not wired to the external circuit. Hence, the templated cathode may be limited by the electronic conductivity of the system.

Summary

This chapter examined the question:

Does the nanostructure created by templating with microphase-separating copolymers offer an improvement to a particular set of battery metrics, e.g. rate capability?

This chapter has shown that the continuous nanometer scale structure created by the structure-direction of vanadium oxide within microphase-separating copolymers was preserved after thermal removal of the copolymer. Attempts were made to partially convert of the copolymer template to graphitic carbon through heating under inert

atmospheres. This resulted in a partial reduction of V^{5+} to V^{4+} . Subsequent heating steps in air oxidized the vanadium but also combusted the carbon.

The diffusion lengths of the nanoscale architecture were an order of magnitude lower than those of commercially available particles, resulting in dramatically reduced characteristic diffusion times of Li^+ within vanadium oxide. The resulting inorganic was reprinted with carbon black and PVDF into a traditional composite cathode that showed improved rate capability over the non-templated sol-gel. The results of the various samples described in this chapter are summarized in Table 6-4.

Table 6-4: Summary of sol-gel derived vanadium oxide films, templated and non-templated, with varying heat treatments.

Sample	%C	% V^{5+} (XPS)	Particle size (ca.)	Surface area	1 st discharge capacity at 3C
Non-templated	-	~88	.3 – 1 μm	20 m^2/g	86 mAh/g
VO _x (Ar)	12.38	~73	10 nm	200 m^2/g	
VO _x (Air)	0.1	~92	40 - 60 nm		
VO _x (Ar/Air)	0.13	~85	40 - 60 nm		144 mAh/g

An improvement in capacity at 3C was seen for the templated cathode; however, battery performance may have been limited because the nanometer-sized cathode particles offered through the templating technique were not wired electronically on that same nanoscale.

The next chapter will provide a summary of the work described in this thesis, combining the conclusions from these last three chapters. The chapter will also provide some areas for future research.

References

1. Patrisi, C. J. & Martin, C. R. "Improving the Volumetric Energy Densities of Nanostructured V_2O_5 Electrodes Prepared Using the Template Method." *Journal of the Electrochemical Society*, **2001**, 148, A1247-A1253.
2. Sides, C. R. & Martin, C. R. "Nanostructured Electrodes and the Low-Temperature Performance of Li-ion Batteries." *Advanced Materials*, **2005**, 17, 125-128.
3. Sides, C. R., Li, N., Patrisi, C. J., Scrosati, B. & Martin, C. R. "Nanoscale Materials for Lithium-Ion Batteries." *MRS Bulletin*, **2002**, 604-606.
4. Wang & Cao, G. "Synthesis and Enhanced Intercalation Properties of Nanostructured Vanadium Oxides." *Chemistry of Materials*, **2006**, 18, 2787-2804.
5. Sudant, G., Baudrin, E., Dunn, B. & Tarascon, J. M. "Synthesis and Electrochemical Properties of Vanadium Oxide Aerogels Prepared by a Freeze Drying Process." *Journal of the Electrochemical Society*, **2004**, 151, A666-A671.
6. Odani, A. et al. "Testing Carbon-Coated VO_x Prepared via Reaction under Autogenic Pressure at Elevated Temperature as Li-Insertion Materials." *Advanced Materials*, **2006**, 18, 1431-1436.
7. Sides, C. R., Croce, F., Young, V. Y., Martin, C. R. & Scrosati, B. "A High-Rate, Nanocomposite $LiFePO_4$ /Carbon Cathode." *Electrochemical and Solid-State Letters*, **2005**, 8, A484-A487.
8. Swider-Lyons, K. E., Love, C. T. & Rolison, D. R. "Improved Lithium Capacity of Defective V_2O_5 Materials." *Solid State Ionics*, **2002**, 152-153, 99-104.
9. Demeter, M., Neumann, M. & Reichelt, W. "Mixed-valence vanadium oxides studied by XPS." *Surface Science*, **2000**, 454-456, 41-44.
10. Pol, S. V. (ed. Olivetti, E. A.) (Cambridge, MA, 2006).
11. Anderson, D. M. & Thomas, E. L. "Microdomain Morphology of Star Copolymers in the Strong-Segregation Limit." *Macromolecules*, **1988**, 21, 3221-3230.

12. Winey, K. I., Thomas, E. L. & Fetters, L. J. "Ordered morphologies in binary blends of diblock copolymer and homopolymer and characterization of their intermaterial dividing surfaces." **1991**.
13. Li, N., Martin, C. R. & Scrosati, B. "Nanomaterial-based Li-ion battery electrodes." *Journal of Power Sources*, **2001**, 97-98, 240-243.
14. Li, N. & Martin, C. R. "A High-Rate, High-Capacity, Nanostructured Sn-Based Anode prepared by sol gel template synthesis." *Journal of the Electrochemical Society*, **2001**, 148, A164-A170.
15. Mui, S. C. PhD thesis in *Materials Science and Engineering*. "Electrochemical Kinetics of Thin Film Vanadium Pentoxide Cathodes for Lithium Batteries." 2005.
16. Meethong, N., Huang, H.-Y., Speakman, S. A., Craig, W. C. & Chiang, Y.-M. "Strain accommodation during phase transformations in olivine-based cathodes as a materials selection criterion for high-power rechargeable batteries." *Advanced Functional Materials*, **2007**, in press.

Chapter 7 : Contributions of Dissertation

This chapter provides a summary of the findings of this study, synthesizing the conclusions from the previous three chapters and providing potential future directions for subsequent work.

General Conclusions

This thesis investigated using microphase-separating block and graft copolymer electrolytes as a matrix for the *in situ* growth of nanoscale vanadium oxide to generate cathode architectures. This structure-direction of the inorganic phase growth within the ion-conducting (POEM) domain of copolymers was proposed as a means to increase the surface-area-to-volume ratio within the cathode, potentially improving battery performance by decreasing mass transfer limitations. Rate capability was the battery metric that was expected to improve as a result of this change in architecture. Enhanced performance was expected due to reduced Li^+ ion diffusion distances and increased surface area over which faradaic reactions can occur. If used in conjunction with a solid electrolyte of the same polymer used in the matrix, this strategy also may improve the kinetics at the electrode/electrolyte interface. The solid electrolyte would also address safety issues present with a flammable organic liquid electrolyte and facilitate the formation of a solid-state device that can be made mechanically flexible.

This dissertation set out to answer the following questions:

Can microphase-separated polymers be used to direct the growth of cathode active materials, such as transition metal oxides?

Are the resulting microstructures continuous and on an appropriate size scale?

Can these structure-directed materials be used as cathodes? What electronic conductivity additives are necessary to make them usable?

Do these nanocomposites offer an improvement to a particular set of battery metrics, e.g. rate capability?

In situ sol-gel chemistry methods were successfully used to grow an inorganic phase within preferred domains of microphase-separated copolymers. Nanostructured vanadium oxide was grown within the POEM domains of both POEM-*b*-PBMA and POEM-*g*-PDMS resulting in flexible films (thickness average $\sim 100 \mu\text{m}$, depending on polymer and inorganic amount) where the final oxide structure was continuous. The microphase-separation of the block and graft copolymer films was preserved up to a limit in inorganic compound loading as confirmed by SAXS, TEM and STEM. Co-assembled nanocomposite films incorporating up to 34 wt% vanadium oxide in POEM-*b*-PBMA and 31 wt% in POEM-*g*-PDMS were flexible and semi-transparent. The polymer morphology dictated the final structure of the vanadium oxide, which, upon removal of the polymer, contained pore sizes of $\sim 20 - 30 \text{ nm}$ and surface areas of $200 \text{ m}^2/\text{g}$ compared to $20 \text{ m}^2/\text{g}$ for control films of V_2O_5 made without the polymer matrix. Cyclic voltammetry and impedance spectroscopy confirmed the preservation of the redox properties of the vanadium oxide and the ion-conductive properties of the polymer in composite films.

These materials can be used as cathodes but not without an electronic conductivity additive. The challenge in enhancing the electronic conductivity comes in directing a continuous wiring harness to the same POEM domains while retaining access to the transition metal oxide phase. Carbon black was added to the system *in situ* and $\sim 40 \text{ mAh/g}$ was obtained reversibly from an all solid-state battery using lithium foil as the anode. In addition, the use of carbon black resulted in some improved rate capability over that of a composite cathode containing the same weight percentage VO_x and carbon black, when using liquid electrolyte. The solid electrolyte limited this system, as shown from the increased capacity using liquid electrolyte and the performance dependence on the thickness of the solid electrolyte.

The electronically conducting polymer PEDOT also demonstrated the ability to act as a conducting additive for these films. Electrodeposition of PEDOT directly onto the vanadium oxide was achieved; however, the resulting cathodes exhibited poor cyclability. The addition of silver to the POEM-*b*-PBMA/ VO_x composite also enabled its use as a cathode material. This system, when cast on aluminum foil, exhibited some

capacity in a cell with liquid electrolyte. This cell experienced capacity fade and a high silver loading of 30 wt% was required, further limiting the specific battery capacity.

Finally, after removing the polymer by heating under inert atmosphere, the nanostructured vanadium oxide was re-potted with carbon black and PVDF to make a composite cathode film that cycled with better performance at higher rates compared to a control film. Upon removal of the template and grinding, the nanoporous network structure was preserved, providing micron-sized aggregations of ~10 nm vanadium oxide struts. This cathode was limited electronically, however, as the vanadium oxide lacked contact with the conductivity additive on the scale of the nanostructure. Cycling these systems also showed improvement in rate capability over a control made with commercial vanadium oxide, resulting in 96% of theoretical capacity (144 mAh/g) when cycled at 3C as opposed to 58% for control films (83 mAh/g) cycled at the same rate.

The architecture created by structure-directing the growth of an inorganic phase within microphase-separated copolymers offered a continuous nanoscale morphology that showed improvement in rate capability when used as a cathode film after the addition of a conductivity additive. An all solid-state battery was cycled using the composite film with a polymer electrolyte, but the performance of this system was gated by the electrolyte. When a liquid electrolyte was used, the nanocomposite film showed improved rate capability over a conventional composite cathode and a similar improvement in rate capability was seen with nano-templated vanadium oxide potted with PVDF and carbon black. The improvement in rate capability was smaller than expected in comparison with similar studies found in the literature.[1, 2] This was in part due to the limits in ionic conductivity of the polymer and the electronic conductivity within the cathode. The suggested directions for this work, described in the next section, provide some potential ways this architecture could be further exploited.

Suggested Directions

Using vanadium oxide as the inorganic to incorporate into microphase-separating copolymers offered several advantages for this work. This oxide could be used as a cathode without pre-lithation. The ability to synthesize the oxide at room temperature and obtain redox properties in lithium metal batteries without a high-temperature calcination step enabled preservation of the polymer in the final film. If we are not confined by the

desire to preserve the polymer, several chemistries are available that would offer higher electronic conductivity or flexibility in choice of cathode material. The ability to synthesize ~10 nm-sized particles would be useful for several other oxide systems. A few of these systems are described below.

Phospho-olivines, developed by Goodenough [3], have offered a great deal of promise as cathode materials. Sol-gel methods for the synthesis of lithium iron phosphates might involve, dissolving $\text{Li}(\text{OH})\cdot\text{H}_2\text{O}$, $\text{FeC}_2\text{O}_4\cdot 2\text{H}_2\text{O}$, and $\text{NH}_4\cdot\text{H}_2\text{PO}_4$, in water, in which polyacrylic acid and citric acid are added as complexing agents for the formation of the gel.[4] This could be incorporated into the microphase-separating copolymer. Heating is required to decompose the organics and further sinter the precursors under a slightly reducing atmosphere to create the final LiFePO_4 chemistry.

Recent work by Kang *et al.* produced $\text{Li}(\text{Ni}_{0.5}\text{Mn}_{0.5})\text{O}_2$ which exhibited improved rate capabilities over solid solution preparation of the same material.[5] Sol-gel methods would involve stoichiometric amounts of lithium acetate ($\text{Li}(\text{CH}_3\text{COO})\cdot 2\text{H}_2\text{O}$), manganese acetate ($\text{Mn}(\text{CH}_3\text{COO})_2\cdot 4\text{H}_2\text{O}$), and nickel acetate ($\text{Ni}(\text{CH}_3\text{COO})_2\cdot 4\text{H}_2\text{O}$) dissolved in water with citric acid as a chelating agent.[6] Further decreasing particle size for this material, using the templating method described in this research, might further improve rate capability. Alumina templates have been used to produce nanowire arrays of nickel manganese oxides.[7]

Towards other battery materials, similar strategies could be employed to form anode structures of tin oxides or other materials as was done by Mui *et al.*[8] Similar to the work of Bullock and Kofinas, both anode and cathode materials could be structure-directed into block copolymers, resulting in an entire battery made of the same base copolymer “doped” differently for positive and negative electrodes.[9]

As advances in solid polymer electrolyte materials are made, this approach could also be applied to microphase-separating polymers with higher ionic conductivities. Alternatively, use of existing electrolytes with higher ionic conductivities, such as further experimenting with the POEM-g-PDMS copolymer described in this thesis might enable improved battery performance. In addition, low molecular weight additives such as PEGDME have proven useful for ionic conductivity enhancement in polymer electrolytes.[10]

Other applications

Vanadium oxides have shown promise as optical switching materials based on their electrochromic properties.[11-13] The high surface-area-to-volume ratios that are advantageous from a battery electrode perspective, would also be beneficial to an electrochromic system leading to faster switching times. We briefly explored the use of this technique towards electrochromic devices and believe that with further optimization of the template removal or use of a polymer with higher ionic conductivity, this application would be promising.

This work used polymer morphologies that enabled a continuous phase of vanadium oxide, but without this limitation, the composition of the polymer could also be altered to result in different final inorganic morphologies. Beginning with polymer structures where the hydrophilic phase is the minority phase, inorganic spheres or cylinders could be synthesized similar to the work of Ulrich *et al.*[14] Composite nanostructures with tunable morphologies and size scales are used in many applications including biological systems for labeling for particle tracking, separation and drug delivery, or catalysis.[15] Other energy storage devices such as supercapacitors have made use of nano-objects that might be further enabled by this technique.[16] Recent work produced high surface area, hydrophilic graphitic carbon nanocages by templating approaches for use as Pt catalyst supports for low temperature fuel cells.[17] In addition, work in dye-sensitized solar cells uses a light-absorbing dye material in concert with semiconductor materials with nanocrystalline particle morphology.[18] This nanoparticle network serves as a host for electrons migrating to the current collector after excitation in the dye. These particles need to be high surface area to allow for increased light absorption. Anatase (TiO₂) with surface areas from 80 - 200 m²/g typically serves as this wide-bandgap oxide and synthesis of this material results from titanium alkoxides using sol-gel chemistry methods.[19] This approach is analogous to the vanadium oxide synthesis approach outlined in this work and could prove a viable alternative for the semiconductor material in dye-sensitized solar cells.

The structure-direction of inorganic phases within one domain of microphase-separating copolymers provides interesting nanoscale structures relevant to many applications including cathode materials with improved rate capability.

References

1. Sides, C. R. & Martin, C. R. "Nanostructured Electrodes and the Low-Temperature Performance of Li-ion Batteries." *Advanced Materials*, **2005**, 17, 125-128.
2. Dong, W., Rolison, D. R. & Dunn, B. "Electrochemical Properties of High Surface Area Vanadium Oxide Aerogels." *Electrochemical and Solid-State Letters*, **2000**, 3, 457-459.
3. Padhi, A. K., Nanjundaswamy, K. S. & Goodenough, J. B. "Phospho-olivines as Positive-Electrode Materials for Rechargeable Lithium Batteries." *Journal of the Electrochemical Society*, **1997**, 144, 1188-1194.
4. Wang, G. X. et al. "A study on LiFePO₄ and its doped derivatives as cathode materials for lithium-ion batteries." *Journal of Power Sources*, **2006**, 159, 282-286.
5. Kang, K., Meng, Y. S., Breger, J., Grey, C. & Ceder, G. "Electrodes with High Power and High Capacity for Rechargeable Lithium Batteries." *Science*, **2006**, 311, 977-980.
6. Hwang, B. J., Wang, C.J., Chen, C.H., Tsai, Y.W., Venkateswarlu, M. "Electrochemical properties of Li[Ni_xLi_{(1-2x)/3}Mn_{(2-x)/3}]O₂ (0=x=0.5) cathode materials prepared by a sol-gel process." *Journal of Power Sources*, **2005**, 146, 658-663.
7. Zhou, Y. & Li, H. "Sol-gel template synthesis and structural properties of a highly ordered LiNi_{0.5}Mn_{0.5}O₂ nanowire array." *Journal of Materials Chemistry*, **2002**, 12.
8. Mui, S. C. et al. "Block Copolymer-Templated Nanocomposite Electrodes for Rechargeable Lithium Batteries." *Journal of the Electrochemical Society*, **2002**, 149, A1610-A1615.
9. Bullock, S. & Kofinas, P. "Synthesis of an A/B/C triblock copolymer for battery materials applications." *Macromolecules*, **2004**, 37, 1783-1786.
10. Trapa, P. E., Huang, B., Won, Y.-Y., Sadoway, D. R. & Mayes, A. M. "Block Copolymer Electrolytes Synthesized by Atom Transfer Radical Polymerization

- for Solid-State, Thin-Film Batteries." *Electrochemical and Solid-State Letters*, **2002**, 5, A85-A88.
11. Wang, Z., Chen, J. & Hu, X. "Electrochromic properties of aqueous sol-gel derived vanadium oxide films with different thickness." *Thin Solid Films*, **2000**, 375, 238-241.
 12. Ozer, N. "Electrochemical properties of sol-gel deposited vanadium pentoxide films." *Thin Solid Films*, **1997**, 305, 80-87.
 13. Takahashi, K., Wang, Y. & Cao, G. "Growth and electrochromic properties of single-crystal V₂O₅ nanorod arrays." *Applied Physics Letters*, **2005**, 86, 053102.
 14. Ulrich, R., Du Chesne, A., Templin, M. & Wiesner, U. "Nano-objects with Controlled Shape, Size, and Composition from Block Copolymer Mesophases." *Advanced Materials*, **1999**, 11, 141-146.
 15. Park, C., Yoon, J. & Thomas, E. L. "Enabling Nanotechnology with Self Assembled Block Copolymer Patterns." *Polymer*, **2003**, 44, 6725-6760.
 16. Kudo, T. et al. "Amorphous V₂O₅/carbon composites as electrochemical supercapacitor electrodes." *Solid State Ionics*, **2002**, 152-153, 833-841.
 17. Wang, J. N. et al. "Synthesis of High Surface Area, Water-Dispersible Graphitic Carbon Nanocages by an in situ Template Approach." *Chemistry of Materials*, **2007**, 19, 453-459.
 18. Graetzel, M. "Dye-sensitized Solid-State Heterojunction Solar Cells." *MRS Bulletin*, **2005**, 30, 23-28.
 19. Burnside, S. D. et al. "Self-Organization of TiO₂ Nanoparticles in Thin Films." *Chemistry of Materials*, **1998**, 10, 2419-2425.